Dissertation
submitted to the
Combined Faculties of the Natural Sciences and Mathematics
of the Ruperto-Carola-University of Heidelberg, Germany
for the degree of
Doctor of Natural Sciences

Put forward by
Alessandra Grassi
born in: Arezzo, Italy
oral examination: July 25th, 2013

BARYON ACOUSTIC OSCILLATIONS AND PRIMORDIAL NON-GAUSSIANITIES WITH WEAK LENSING

Referees:	Prof. Dr. Björn Malte Schäfer
	Prof. Dr. Luca Amendola

A Fede
e alle nostre pagine bianche

ABSTRACT-ZUSAMMENFASSUNG

This work introduces two investigations on possible new weak lensing applications. In the first part, I present a study on the possibility of detecting baryon acoustic oscillations by means of 3d weak lensing (3dWL). Basing our analysis on a Fisher matrix approach, we quantify the uncertainty on inferring the amplitude of the power spectrum wiggles with 3dWL. Ultimately, we find that surveys like Euclid and DES should be able to detect, respectively, the first four and three oscillations, with errors reaching the 1% or 10% of the amplitude for the first two wiggles in the case of Euclid. The second part of this work focuses on the study of primordial non-Gaussianities with a classical weak lensing approach. We study inflationary bi- and trispectra, the strentgh of their signals, and the consequences of fitting data with a wrong type of bispectrum on the inferred on f_{NL}. We conclude that contraints on f_{NL} are not competitive with the ones from CMB, but nonetheless valuable in case of a scale-dependent f_{NL}. Lastly, we quantify lensing ability to test the Suyama-Yamaguchi inequality, and ascertain that Euclid could give evidence in favour or against the inequality for large non-Gaussianity values ($\tau_{NL} \geqslant 10^5$ or $f_{NL} \geqslant 10^2$).

In dieser Arbeit untersuche ich zwei neue Anwendungsmöglichkeiten des schwachen kosmischen Linseneffekts. In dem ersten Teil meiner Dissertation zeige ich die Ergebnisse einer statistische Studie, die den Fisher-Formalismus verwendet, ob baryonische Oszillationen in dreidimensionalen Abbildungen der kosmischen Struktur über den Linseneffekt detektiert werden können. Mein Ergebnisse zeigen, dass Durchmusterungen wie Euclid und DES die ersten vier oder drei Oszillationen erkennen, wobei die Amplitude der ersten beiden Oszillationen statistische Fehler im Prozentbereich haben. Im zweiten Teil untersuche ich primordiale nicht-Gaußianitäten durch den klassischen Linseneffekt, insbesondere inflationäre Bi- und Trispektren, deren Signalstärke und die Auswirkungen einer falschen Modellwahl auf die Messung von Parametern wie f_{NL}. Ich zeige, dass Einschränkungen auf f_{NL} nicht mit dem CMB konkurrenzfähig sind, es sei denn die nicht-Gaußianitäten wären skalenabhängig. Schließlich untersuche ich die Möglichkeit, mit dem Linseneffekt die Suyama-Yamaguchi-Ungleichung zu testen, wobei Euclid in der Lage sein sollte, statistische Tests im Parameterbereich $\tau_{NL} \geqslant 10^5$ und $f_{NL} \geqslant 10^2$ durchzuführen.

CONTENTS

LIST OF FIGURES

LIST OF TABLES

ACRONYMS

3dWL	3d weak lensing
BAO	Baryon Acoustic Oscillations
BOSS	Baryon Oscillation Spectroscopic Survey
CMB	Cosmological Microwave Background
DES	Dark Energy Survey
LSS	Large Scale Structure
n-G	non-Gaussianities
SDSS	Sloan Digital Sky Survey
SY	Suyama-Yamaguchi

PREFACE

Many steps have been made since 1915, when Albert Einstein first published his work on a relativistic theory of gravity, marking the birth of modern cosmology. Back then, it was thought that our Universe coincided with the Milky Way, and there was no reason to doubt its staticity. In a decade, both conceptions would have been proven wrong: Observations by Edwin Hubble and, before him, Vesto Slipher, suggested in 1924 that our galaxy was just one among many, and that such distant objects were receding from us, as if the Universe was expanding. Friedmann's equations, derived a couple of years earlier from Einstein's general relativity under the assumptions of homogeneity and isotropy of the Universe, had been themselves implicitly - and, back then, surprisingly - supporting an expanding Cosmos. This was just the beginning of the series of processes that led many common conceptions about our Universe to be revolutionized.

In less than one century, we came to learn that the initial assumptions of homogeneity and isotropy were well-grounded, as the discovery of an extremely uniform background blackbody radiation (CMB) proved in 1965. We are now familiar with the idea of an expanding Universe, and we are able to make predictions about the rate of this motion, both in the past and in the future, and infer some of the consequences it may have on the properties, and the evolution, of the Cosmos' content. Overall, we developed a comprehensive standard model able to describe such properties, and parametrize them by means of some quantities that are being measured with ever-growing precision: the cosmological parameters.

Regardless of all its successes, though, the study of our Universe is far from being a closed issue. Many questions still remain unanswered. We still do not know anything about the true nature of dark matter, postulated to account for several problems: flat rotational curves in spiral galaxies, dynamical properties of galaxy clusters, or the small amplitude of primordial density fluctuations, as observed from the CMB. Such perturbations would not have led to structure formation as we observe it today, had baryonic matter been the only gravitationally interacting species. Our understanding of the nonlinear regime of structure formation is also incomplete. In addition, the origin of the seeds of structure formation, i. e. the primordial distribution of density fluctuations, is not known, and such a distribution must be given as an initial condition in the framework of the standard model. A possible solution to this last issue is given by inflation, also gracefully solving the problem of the excessive flatness of our

Universe as well as the CMB problem, in which isotropy is also observed on scales that should not have been causally connected. Inflation postulates the existence of an early period in which the Universe has undergone an accelerated expansion. Many inflationary models exist, and all of them naturally predict the genesis of density fluctuations. Furthermore, observations dating back to 1998 detected for the first time an - unexpected - acceleration of the Universe, opening a new series of unresolved questions regarding the mechanism that is driving this peculiar type of expansion. Possible solutions could be a modified theory of gravity that on larger scales acts differently to general relativity, or some kind of energy whose properties mimic, in some sense, the effect of a repulsive gravity. Such a component is usually referred to as dark energy, and its contribution could either vary or be uniform with time; in the last case, dark energy would have the same effect of a cosmological constant Λ, originally introduced by Einstein in his field equations. These are only a fraction of the still open questions, and the amount of the understanding we lack makes cosmology one of the most fecund sciences of our time.

This work, in particular, focuses on two of these unsolved issues. We know that constraints on the nature and properties of dark energy, for instance, can be obtained by an accurate description of the Universe's expansion history. Such a description can be provided by standard rulers: objects or properties of known size, and for whom we can easily retrieve the distance-redshift relation. Baryon acoustic oscillations, frozen relics of the time when matter and radiation were coupled together, are promising candidates to the role of standard rulers, and could indeed help us understanding more about the nature of dark energy. The other problem here addressed involves the inflationary paradigm. It turns out that many different models of inflation predict diverse degrees of deviation from Gaussianity in the distribution of primordial density fluctuations. A detection of such deviation, and of its entity, could tell us something about the leading mechanism responsible for inflation.

Both baryon acoustic oscillations and primordial non-Gaussianities are observable properties of the matter distribution. The purpose of this work is then to understand what kind of contribution could a weak lensing analysis give to the quest for the detection, and measurement, of these two quantities. The weak lensing method, in effect, can infer informations about the cosmological density field. It does so by exploiting the relativistic deflection of light due to variations of the gravitational potential, and hence of the mass distribution.

This thesis is articulated in three parts. Part i has a twofold, introductory purpose. A collection of the main results of modern cosmology will be given in Chapter 1, in order to frame the original research of this work in a wider picture. Here I will review a description of the Universe's metric and dynamical properties, when homogeneity and isotropy are assumed to be valid on large scales. Growth of primordial perturbations and their statistical description will also be concisely addressed, as well as a schematic chronology of the Universe from its very first instants up to now. The second aim of this introductory part is to introduce gravitational lensing both generically, as a relativistic effect, and as a cosmological tool, especially in its weak limit. A special mention to 3d weak lensing, able to produce a 3-dimensional shear map by using photometric redshift of galaxies as an estimate of their distance, will also be given in this chapter.

The following parts will present our two investigations. Part ii will focus on the possibility of detecting baryon acoustic oscillations by means of 3d weak lensing. It constitutes of Chapter 3, where I first examine the physics governing the baryon oscillations genesis. I will continue by introducing the concept of standard rulers, proving that baryon acoustic oscillations can be considered such, hence providing motivation for the scientific community interest in these cosmological tool. In Chapter 4, I will propose a novel method for their detection. Our method is inspired by some of weak lensing interesting properties such as, most importantly, its sensitivity to both dark and baryonic matter, its well understood physics, and its independency from other methods, especially regarding probed redshift or scales, but also systematic errors and degeneracies. Unfortunately, the wide line-of-sight weighting functions arising from the source projection on the sky plane, renders narrowband features of the matter power spectrum unobservable with classical weak lensing. A 3d lensing approach, though, provides a direct estimate of the 3-dimensional matter distribution. Our study, here reproduced as in Grassi and Schäfer [2013], quantifies the statistical power of this approach on inferring the presence of one or more baryon acoustic wiggles, and the precision that it allows for constraining the spectrum at the oscillations wavelengths. Such analyses are carried out for future surveys like Euclid, DES, or the hypothetical DEEP. Lastly, our study investigates how much the uncertainties on the determination of the power spectrum are sensitive to some typical survey parameters.

Part ii will be centered on the investigation of primordial non-Gaussianities with classical weak lensing, starting with an introduction of such features of the primordial density distribution in Chapter 5. Here I will briefly explain the common traits of inflationary theories, and why the assumption of a period with an accelerated expansion made its way over the years in explaining some of the standard cosmological model contradictions. Moreover, I will enumerate the possible parametrizations of the deviations from Gaussianity predicted by some inflationary models, and explain why those deviations can be devised as a means to study the mechanism behind inflation. Thereafter, I will review in Chapter 6 the results we obtained in Schäfer et al. [2012], where the statistical sensitivity of the weak lensing bispectrum to the signal from the three main shapes of primordial non-Gaussianity is tested. Finally, in Chapter 7, I will propose weak lensing as a method for testing the Suyama-Yamaguchi inequality: It is a fundamental relation that links two of the non-linear parameters that describe and parametrize the degree of primordial non-Gaussianities. Although such inequality is a general result, violations are predicted among certain inflationary models. Being in the condition to detect this kind of anomalies could indeed help to discriminate between different, competing models of inflation. Our investigation starts from the study of the weak lensing bi- and trispectrum and the computation of the relative signal-to-noise ratio. We give an analytical expression for the probability of the inequality to be exactly fulfilled, and we finally estimate the degree of primordial non-Gaussianity allowing to make a reliable statement about the relation.

Chapter iv will ultimately summarize the main results of this thesis, and Appendix A will briefly outline the numerical method used in the computation of the 3d weak lensing covariance matrices.

Part of the content presented in this thesis has appeared already, or will soon appear, in the following publications:

- *Detecting baryon acoustic oscillations by 3d weak lensing*
  A. Grassi and B. M. Schäfer,
  submitted to MNRAS, under revision,
  arXiv:1303.1024;

- *A weak lensing view on primordial non-Gaussianities*
  B. M. Schäfer, A. Grassi, M. Gerstenlauer and C. Byrnes,
  MNRAS, 421:797-807;

- *A test for the Suyama-Yamaguchi inequality from weak lensing*
  A. Grassi, L. Heisenberg, C. Byrnes and B. M. Schäfer,
  in preparation

Part I

INTRODUCTION TO COSMOLOGY

1

FOUNDATIONS OF COSMOLOGY

This chapter intends to be a collection of the main results obtained in Cosmology. For a more detailed dissertation on the main aspects of modern cosmology I refer to Coles and Lucchin [2002], Padmanabhan [1993], Bartelmann [2010b], and to Bartelmann [2012] for an analysis of the evolution of this discipline over time[1].

dark and baryonic matter

Before starting, it could be worthwhile pointing out that all along this chapter and this Thesis I will refer to ordinary[2] matter as *baryonic*. By *matter*, on the other hand, I will mean both baryons and *dark matter*. The existence of a type of matter that could only interact by gravity and possibly by weak force, has been speculated to account for rotation curves of spiral galaxies, inconsistencies betwbeen cluster of galaxies mass estimates and other probes. Unfortunately, there is still no direct evidence for a particle with such characteristics, although many efforts are being done to detect it. For some recent reviews on the subject, please see Del Popolo [2013], Frenk and White [2012], Peter [2012], or Einasto [2011].

The present chapter is organized as follows. Section 1.1 will start from the Cosmological principle and derive the main properties possessed by a homogeneous and isotropic Universe. In particular, it will deduce a metric for such a system, define distances, and parametrize the density of the Cosmos content. Section 1.2, instead, will focus more on the inhomogeneous part of our Universe, namely on how

---

[1] among the others, I would like to mention Prof. Bartelmann's lecture notes on Cosmology, kindly provided on:
ita.uni-heidelberg.de/research/bartelmann/Lectures/cosmology/.

[2] meaning, by ordinary: Able to interact gravitationally and electromagnetically.

density perturbations are supposed to evolve, and how they can be statistically described. Lastly, Section 1.3 will present a schematic timeline of the Universe, from the first instants after the big bang, until the beginning of structure formation.

1.1 DESCRIBING A HOMOGENEOUS UNIVERSE

A great part of modern cosmology is based on two very simple assumptions:

1. the properties of the Universe are independent of the direction when averaged over large scales, therefore the Universe is isotropic;
2. we are not special or favored observers in any way, and our position in the Universe is supposed to be comparable with any other (*Copernican principle*).

Cosmological principle

The two statements above imply that the Universe is both homogeneous and isotropic, and are usually referred to as the *Cosmological principle*.

general relativity

In addition, we assume that gravity is described by Einstein's general relativity. Since the other three fundamental forces (weak, strong, and electromagnetic) are either intrinsically acting on very small scales (weak and strong forces), or have their scales limited by charge shielding (electromagnetic force), gravity, whose action is not negligible even at very large scales, is indeed the most relevant type of interaction in the cosmological framework.

1.1.1 *Robertson-Walker metric*

In general relativity, the line element can be written as $ds^2 = g_{ij}dx^i dx^j$. As soon as the Cosmological-principle ansatz is adopted, it can be shown that $g_{0i} = 0$ (isotropy would be violated, otherwise), and $g_{00} = c^2$ (the Copernican principle imposes that all fundamental observers[3] witness the same properties and evolution of the Universe), so that $ds^2 = c^2dt^2 + g_{ij}dx_i dx_j$. Spacetime can therefore be decomposed in spatial hypersurfaces at constant time. To preserve isotropy, these surfaces should only be multiplied by a scale function $a(t)$:

$$ds^2 = c^2dt^2 - a^2(t)dl^2. \tag{1.1}$$

By convention, the scale factor $a(t)$ is normalized in such a way that $a(t_0) = a_0 = 1$, where t_0 corresponds to today.

Robertson-Walker metric

In spherical coordinates $\mathbf{l} = (r, \theta, \phi)$, Equation 1.1 reads

---

[3] by fundamental one means free-fall observers, or, equivalently, observers placed in an inertial frame of reference.

$$ds^2 = c^2 dt^2 - a^2(t)\left[dr^2 + f_K^2(r) d\omega^2\right], \tag{1.2}$$

where $d\omega$ is the solid angle element. The previous equation describes the metric of a homogeneous and isotropic universe, and is called the *Robertson-Walker metric*. The quantity f_K is a function that is restricted by homogeneity to the values

$$f_K(r) = \begin{cases} K^{-1/2}\sin(K^{-1/2}r) & K > 0, \text{ spherical,} \\ r & K = 0, \text{ flat,} \\ |K^{-1/2}|\sinh(|K^{-1/2}|r) & K > 0, \text{ hyperbolic,} \end{cases} \tag{1.3}$$

with K being a constant value describing spatial curvature.

1.1.2 *Metric's dynamics and density parameters*

Homogeneity turns out to be useful also in determining the dynamical properties of the metric, i. e. the dynamical properties of $a(t)$. In fact, by assuming that pressure p and density ρ of the Universe content - assumed as an ideal fluid - only depend on time, one can make use of the Robertson-Walker metric to solve Einstein's field equations:

ideal fluid: dissipationless, subject to pressure but not to shear stress

$$G_{\mu\nu} = \frac{8\pi G}{c^2} T_{\mu\nu} + \Lambda g_{\mu\nu}, \tag{1.4}$$

where $T_{\mu\nu}$ is the energy momentum tensor, depending on the density and pressure of the fluid, G is the gravitational constant, $G_{\mu\nu}$ the Einstein-tensor, linked to the second derivatives of the metric, and Λ is the cosmological constant. The result is then

Friedmann's equations

$$\left(\frac{\dot{a}}{a}\right)^2 = \frac{8\pi G}{3}\rho - \frac{Kc^2}{a^2} + \frac{\Lambda}{3}, \tag{1.5}$$

$$\frac{\ddot{a}}{a} = -\frac{4\pi G}{3}\left(\rho + 3\frac{p}{c^2}\right) + \frac{\Lambda}{3}. \tag{1.6}$$

These two relations are called *Friedmann's equations*, and they are not necessarily independent. In effect, the first equation can be recovered from the integration of the second if the expansion is considered to be adiabatic, i. e.

$$\frac{d}{dt}(a^3 \rho c^2) + p\frac{d}{dt}(a^3) = 0. \tag{1.7}$$

We can define the logarithmic derivative of the scale factor $a(t)$ as the Hubble parameter

Hubble parameter

$$H(t) \equiv \frac{\dot{a}}{a}, \tag{1.8}$$

whose dimension is of course the inverse of a time (the dotted quantity will be intended as derivatives with respect to t).

critical density

Starting from the first Friedmann's equation (Equation 1.5) one can see that there exists a critical quantity, called ρ_{cr}, that, for a Universe with no cosmological constant, defines the density the Universe should have to be exactly flat:

$$\rho_{cr}(t) \equiv \frac{3H^2(t)}{8\pi G}. \tag{1.9}$$

In some sense, a sphere containing matter at the critical density is forced to have a perfect balance between gravitational potential and kinetic energy, causing the expansion to be constant, and the curvature is equal to 1.

density parameters

It is convenient to express the energy density at a given t of the species contained in the Universe as a ratio between their density and $\rho_{cr}(t)$, namely the *density parameter*:

$$\Omega_i(t) \equiv \frac{\rho_i(t)}{\rho_{cr}(t)}. \tag{1.10}$$

In particular, we can define such a parameter also for the cosmological constant Λ,

$$\Omega_\Lambda(t) = \frac{\Lambda}{3H^2(t)}, \tag{1.11}$$

and the curvature K,

$$\Omega_K \equiv 1 - \Omega_{m0} - \Omega_{r0} - \Omega_{\Lambda 0} = -\frac{Kc^2}{H_0^2}, \tag{1.12}$$

where the subscripts 0 indicate that the quantity must be evaluated today, i. e. $t = t_0$.

expansion function

Once that the density parameters are defined, one can express the first Friedmann's equation in terms of the Ω_i, yielding

$$\begin{aligned} H^2(a) &= H_0^2\left[\Omega_{r0}a^{-4} + \Omega_{m0}a^{-3} + \Omega_K a^{-2} + \Omega_{\Lambda 0}\right] \\ &\equiv H_0^2 E^2(a). \end{aligned} \tag{1.13}$$

The quantity $E(a)$ is called the *expansion function*, and carries information about the expansion history.

1.1.3 *Redshift*

One key quantity in cosmology is the *redshift*, that is the relative change in wavelength of the light emitted by a source and later detected by an observer. If λ_s is the wavelength emitted by the source, and λ_o the one observed, then the redshift is

$$z \equiv \frac{\lambda_o - \lambda_s}{\lambda_s}. \tag{1.14}$$

Since this stretching of waves on the fly is given by the recession of the source due to cosmic expansion, it comes naturally that z is linked to the ratio of the scale factors at emission and observation, respectively a_s and a_o. In particular, we have

relation between redshift and scale factor

$$1 + z = \frac{a_o}{a_s}. \tag{1.15}$$

1.1.4 *Cosmological distances*

While a Euclidean description of space-time would allow for a univocal definition of the distance between two given objects, this is not anymore true in cosmology. In addition, differently from a static, Euclidean framework, distances will depend on the scale factor, as well. As it will be shown in this section, there are several ways to define distance, and although they tend to each other in the limit of a Euclidean space, they can substantially differ in a more general context.

PROPER DISTANCE (d_{prop}) is the distance measured by the time it takes for a light ray to travel from a source placed at a redshift z_2 to an observer put at z_1:

$$d\,d_{prop} = -c\,dt = -c\frac{da}{\dot{a}}, \tag{1.16}$$

yielding

$$d_{prop}(z_1, z_2) = c\int_{a(z_1)}^{a(z_2)} \frac{da}{\dot{a}}. \tag{1.17}$$

COMOVING DISTANCE (d_{com}) is the distance that is *comoving* with the cosmic flow, therefore evaluated at $t = \mathrm{const}$. It is the difference of coordinates l (see Equation 1.1) between the source and the observer along the geodesic $ds = 0$, giving $-c\,dt = a\,d\,d_{com}$ and

$$d_{com}(z_1, z_2) = c\int_{a(z_1)}^{a(z_2)} \frac{da}{\dot{a}a}. \tag{1.18}$$

ANGULAR DIAMETER DISTANCE (d_A) is defined as the ratio between the true size of a given source and its angular size as perceived by the observer. The angular size also depends on the spatial curvature, and it can be proved that

$$d_A(z_1, z_2) = \frac{a(z_2)}{a(z_1)} f_K[d_{com}(z_1, z_2)]. \tag{1.19}$$

Since the quantity $a(z_2)$ gets smaller as the source is placed farther away, the angular diameter distance has the interesting property of not being monotonically increasing with d_{com}: As a result, after a certain z depending on the cosmology objects tend to look bigger as they are farther.

angular diameter distance is not monotonic

LUMINOSITY DISTANCE (d_L), on the other hand, comes from the relation existing between the intrinsic luminosity of a source and the flux received by an observer. It is linked to the angular diameter distance via the *Etherington relation*

$$d_l(z_1, z_2) = \left(\frac{L}{4\pi F}\right)^2 = \left(\frac{a(z_2)}{a(z_1)}\right)^2 d_A(z_1, z_2), \tag{1.20}$$

valid in very kind of space time.

1.2 INTRODUCING INHOMOGENEITIES

The Universe can indeed be considered homogeneous on large scales. On the other hand, structures like clusters, galaxies, stars, or life itself, show that on smaller scale, we have some inhomogeneities to account for. The origin of the primordial distribution of perturbations is still subject of debate, although inflation, i. e. a period of accelerated expansion, may be the source mechanism for such fluctuations (for more details on this topic, please see Section 5.2). This section will give a brief overview on how density perturbations evolve with time and how they can be described statistically.

1.2.1 *Linear description of perturbations*

continuity, Euler, and Poisson equations

For small inhomogeneities, a Newtonian treatment of the problem is still considered a good approximation. A non-relativistic fluid can be described by the continuity and Euler equations,

$$\frac{\partial \rho}{\partial t} + \nabla \cdot \rho \mathbf{v} = 0, \tag{1.21}$$

$$\frac{\partial \mathbf{v}}{\partial t} + (\mathbf{v} \cdot \nabla)\mathbf{v} + \frac{1}{\rho}\nabla p + \nabla \Phi = 0, \tag{1.22}$$

formulating, respectively, mass and momentum conservation. In addition, the gravitational potential Φ should also satisfy the Poisson equation

$$\nabla^2 \Phi = 4\pi G \rho, \tag{1.23}$$

that links it to the density field.

density contrast

Density perturbations can be described via of the density contrast

$$\delta(\mathbf{x}, t) \equiv \frac{\rho(\mathbf{x}, t) - \bar{\rho}(t)}{\bar{\rho}(t)}, \tag{1.24}$$

. By means of linear perturbation theory, from Equation 1.21, Equation 1.22 and Equation 1.23 it is possible to derive the time evolution of the density contrast δ:

$$\ddot{\delta}(\mathbf{x}, t) + 2H\dot{\delta}(\mathbf{x}, t) - \frac{c_s^2}{a^2}\nabla^2 \delta(\mathbf{x}, t) - 4\pi G \rho_0 \delta(\mathbf{x}, t) = 0, \tag{1.25}$$

or its equivalent form in Fourier space

$$\ddot{\delta}(\mathbf{k},t) + 2H\dot{\delta}(\mathbf{k},t) + \delta(\mathbf{k},t)\left(\frac{c_s^2}{a^2}k^2 - 4\pi G\rho_0\right) = 0, \tag{1.26}$$

where a transformation to comoving coordinates $\mathbf{r} = a\mathbf{x}$ was performed. The term c_s, present in both equations, is the sound speed, such that $\delta p = c_s^2 \delta\rho$.

Jeans length

Equation 1.26 naturally defines a scale, called *Jeans length*

$$\lambda_J \equiv \frac{2\pi}{k_J} = \sqrt{\frac{c_s^2 \pi}{G\rho_0}}, \tag{1.27}$$

telling us something about the threshold under which pressure balances gravitational attraction. It turns out that every perturbation whose scale is smaller than λ_J oscillates, whereas those whose scale is larger, grow or decay.

perturbations growth rate

It is interesting to notice that perturbations grow at a different rate depending on which species is dominating the overall Universe energy density. In particular, it can be found that $\delta \propto a^2$ in the radiation-dominated era, and $\delta \propto a$ in the matter-dominated epoch.

growth function

The *linear growth function* $D_+(a)$ traces the evolution of the density contrast with respect to the scale factor a,

$$D_+(a) \equiv \frac{\delta(a)}{\delta(a_0)} \equiv \frac{\delta(a)}{\delta(1)} \tag{1.28}$$

There is a good fitting formula for the growth factor in case of a ΛCDM model, that reads [Carroll et al., 1992]

$$D_+(a) = \frac{5a}{2}\Omega_m \left[\Omega_m^{4/7} - \Omega_\Lambda + \left(1 + \frac{\Omega_m}{2}\right)\left(1 + \frac{\Omega_\Lambda}{70}\right)\right]^{-1}. \tag{1.29}$$

1.2.2 *Statistical description of inhomogeneities: The power spectrum*

density contrast as a stochastic field

The density contrast $\delta(\mathbf{x})$, introduced in the previous section, can be seen as a homogeneous and isotropic stochastic field, thanks to the Cosmological Principle. Our Universe, on the other hand, can be devised as a product of a statistical realization of such a field. What we are interested in, is a study of the properties of the field $\delta(\mathbf{x})$.

ergodic hypothesis

One conceptual problem arises as we notice that we are allowed to observe *only one* realization of the stochastic field. A way out to this limitation is making use of the *ergodic hypothesis*, stating:

- averaging a given stochastic field at a fixed point over the entire ensemble of realizations is equivalent to carrying out a spatial average on its own realizations.

It can be proved that a stochastic field is ergodic if the field can be described by a Gaussian statistics and if its power spectrum is continuous [Adler, 1981].

The density fluctuations can indeed be assumed to be Gaussian (some amount of deviations from Gaussianity is predicted by some inflationary theories, topic that will be treated in much more detail over all Part iii; nevertheless, Gaussianity remains a good first approximation for the field $\delta(\mathbf{x})$). Moreover, it is known that a Gaussian field is completely defined by its mean and variance. Since the mean of the density contrast field is null by construction (see Equation 1.24), the variance is all we need to exhaustively describe the field $\delta(\mathbf{x})$.

correction function

correlation function

The variance of a field σ^2, is related to that field's correlation function

$$\xi(\mathbf{r}) \equiv \langle \delta(\mathbf{x}) \delta(\mathbf{x}+\mathbf{r}) \rangle, \tag{1.30}$$

describing how much a given field's realization moves away from a purely Poissonian realization; in other words, how much a field tends to be correlated on certain scales. In fact, the variance σ^2 coincides with the correlation function when $\mathbf{r} = 0$. If we define the power spectrum to be the correlation function's equivalent in Fourier space, as follows

power spectrum

$$\langle \delta(\mathbf{k}) \delta^*(\mathbf{k}') \rangle = (2\pi)^3 P_\delta(k) \delta_D(\mathbf{k}-\mathbf{k}'), \tag{1.31}$$

(valid if the random field is homogeneous) it is straightforward to see that there is a particular link between variance and power spectrum:

$$\sigma^2 = 4\pi \int \frac{k^2 dk}{(2\pi)^3} P(k). \tag{1.32}$$

As a consequence, the two-point statistics $\xi(\mathbf{r})$ and $P(k)$ are sufficient to describe the properties of the field.

why using the power spectrum?

There are several reasons why the power spectrum is often preferred over the correlation function. Among the advantages of using $P(k)$, for instance, we can acknowledge the fact that, for homogeneous Gaussian perturbations, estimates of the power spectrum at different k are uncorrelated, while this does not hold for the correlation function. Also, from definitions in Equation 1.31 and Equation 1.30, it is easy to see that the covariance matrix of $\delta(\mathbf{k})$ is a diagonal matrix, whereas in configuration space it is not. Most importantly, if the background of a field has some kind of symmetry, the most natural choice for expanding perturbations of the field is in eigenmodes of that symmetry. Due to our hypotheses of isotropy and homogeneity, we can state the background field to be symmetric under translations, and Fourier modes are exactly the eigenmodes of the translation operator [Hamilton, 2009].

Inflationary theories generally predict a primordial power spectrum of the type

$$P(k) \propto k^{n_s}, \tag{1.33}$$

where n_s is called *spectral index* and is very close to 1 (see also Table 1.1 for the latest constraints on n_s).

The power spectrum that we observe today has a dependence on k that goes like

$$P(k) \propto \begin{cases} k & (k < k_0), \\ k^{-3} & (k \gg k_0), \end{cases} \tag{1.34}$$

where k_0 depends on the time of equality between matter and radiation, and on when a perturbation of a given scale enters the horizon. Such behavior of the power spectrum on the smaller scales is due to the growth suppression for modes entering the horizon when radiation is still dominating.

1.3 A TIMELINE OF THE COSMOS EVOLUTION

In this last section, some key events in the Universe history will be presented as we follow the timeline of the cosmic evolution. Please note that the time intervals indicated on the margins are purely indicative.

THE EARLY UNIVERSE The events of the very early Universe are known until a certain extent. This epoch is thought to be described by grand unification theories, stating a unification between electroweak and strong forces. As the temperature drops, due to the cosmic expansion, these forces gradually separate, until, lastly, electromagnetic and weak interactions detach.

first fractions of second

The very first fractions of second of the Cosmos history could have witnessed an accelerated expansion of the Universe, called inflation. Such a mechanism was postulated in order to explain some problems arising in the standard cosmological model, and it is thought to be responsible for the existence of primordial perturbation of the density field. Section 5.1 will address this topic in more detail.

inflation

RADIATION DOMINATION Looking at Equation 1.13 it is straightforward to see that the dominant quantity at early times (small $a(t)$) is the radiation term. During that time the approximation

from 1 s *to* ~ 50 kyrs

$$\frac{da}{dt} = H_0 a^{-1} \Omega_{r0}^{1/2} \tag{1.35}$$

holds, and by solving the equation one finds that, while radiation dominates, the expansion of the Universe scales like

$$a \propto \sqrt{t}. \tag{1.36}$$

Nucleosynthesis takes place in this epoch: In fact, the reached temperature range allows for the formation of the lightest nuclei via a two-body collision process. The production stops at Lithium, due to the fact that as coulomb barriers become stronger, synthesis of heavier nuclei gets more inefficient. The standard model is able to predict the light elements abundances due to nucleosynthesis with a good precision.

During radiation-dominated epoch, and part of the matter-dominated era, (baryonic) matter and radiation are coupled via Thomson scattering.

from ~ 50 kyrs *to* ~ 9.5 Gyrs

MATTER DOMINATION The equality time t_{eq} is defined as the moment when a transition from a radiation-dominated to a matter-dominated Universe occurs. From Equation 1.13 it follows that t_{eq} is such that $a(t_{eq}) \equiv a_{eq} = \Omega_{r0}/\Omega_{m0}$. During this time we have

$$\frac{da}{dt} = H_0 a^{-1/2} \Omega_{m0}^{1/2}, \tag{1.37}$$

hence yielding

$$a \propto t^{2/3}. \tag{1.38}$$

All along matter domination, some quite important events occur.

~ 300 kyrs

- *Recombination and decoupling*. As previously said, during the first stages of the cosmic history, baryonic matter and radiation are coupled via a mechanism called Thomson scattering, due to the continuous interactions between electrons and photons. As the temperature decreases, nuclei and electrons start to combine for the first time, and matter and radiation gradually decouple from each other, evolving separately. This mechanism and one of its most important consequences, i. e. the origin of baryon acoustic oscillations (BAO), are crucial for this Thesis and will be described in Chapter 3. *BAO*

  Another fundamental consequence of this period is the genesis of the cosmological microwave background (CMB), a thermal radiation (corresponding to a black-body radiation of 2.7 K) filling the entire observable Universe, and originated in the moment when the Cosmos became transparent to radiation. First detected in 1965 [Penzias and Wilson, 1965], the CMB initially proved that we live in a Universe that is undoubtedly homogeneous on large scales. On the other hand, the study of the anisotropies observed on the CMB temperature or polarization map is one of the most fertile branch of the entire cosmology, yielding probably the most stringent constraints on cosmological parameters. For some of the latest constraints coming from the

parameter	Planck	Planck+lensing	Planck+WMAP pol.
Ω_{m0}	0.314 ± 0.020	0.307 ± 0.019	$0.315^{+0.016}_{-0.018}$
$\Omega_{\Lambda 0}$	0.686 ± 0.020	0.693 ± 0.019	$0.685^{+0.018}_{-0.016}$
$\Omega_{b0}h^2$	0.02207 ± 0.00033	0.02217 ± 0.00033	0.02205 ± 0.00028
H_0	67.4 ± 1.4	67.9 ± 1.5	67.3 ± 1.2
n_s	0.9616 ± 0.0094	0.9635 ± 0.0094	0.9603 ± 0.0073
σ_8	0.834 ± 0.027	0.823 ± 0.018	0.829 ± 0.012
z_{eq}	3386 ± 69	3362 ± 69	3391 ± 60
z_{drag}	1059.29 ± 0.65	1059.43 ± 0.64	1059.25 ± 0.58
Age [Gyr]	13.813 ± 0.058	13.796 ± 0.058	13.817 ± 0.048

Table 1.1: Constraints on Ω_{m0} (matter density parameter), $\Omega_{\Lambda 0}$ (dark energy density parameter), Ω_{b0} (baryonic matter density parameter), H_0 (Hubble constant), n_s (spectral index of the primordial power spectrum), σ_8 (power spectrum normalization), z_{eq} (equality redshift), z_{drag} (baryon drag redshift), and the age of the Universe, as estimated by Planck Collaboration et al. [2013a].

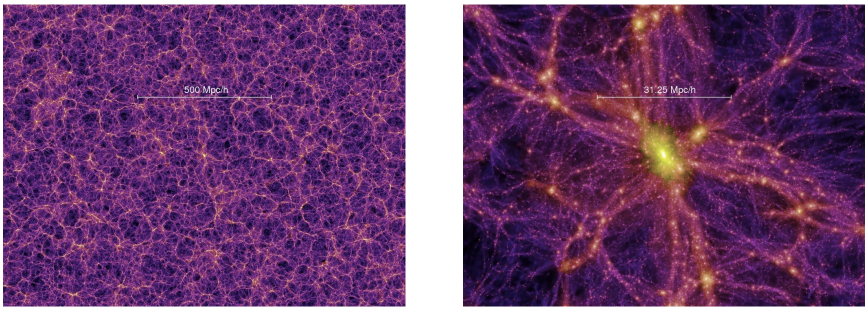

Figure 1.1: Snapshots of the Millennium N-body simulation at $z = 0$, displaying the dark matter distribution on different scales. The Millennium Run simulated a cubic region of side $500h^{-1}$ Mpc, containing 10^{10} particles. Credit: Millennium Run Database.

Planck experiment [Planck Collaboration et al., 2013a], see Table 1.1.

- *Structure formation.* After an interval of time during which primordial perturbations have the opportunity to grow (see Section 1.2.1), the first structures start to form via gravitational instability. The first non-linear systems to collapse are dark matter halos. Stars, galaxies, clusters of galaxies, or any baryonic structure in general, will see the light later, by collapsing in the potential wells of the already formed halos.

  from 0.1 Gyrs *on*

  It is thought that the structure formation process is hierarchical: Small structures (e.g. Population III stars) are supposed to form earlier, whereas larger objects should appear later via a clustering mechanism.

As density fluctuations grow, there comes one point when the small-perturbations approximation does not hold anymore. Even though simplified models exist, able to have predictions about the statistical properties of collapsed objects (e. g. the Press-Schechter mass function [Press and Schechter, 1974]), the description of what happens in the non-linear regime of gravitational collapse needs to be addressed by means of tools such as numerical N-body simulations (see Figure 1.1).

from $\sim$ 9.5 Gyrs *to now*

DARK ENERGY DOMINATION Observation coming from Type Ia supernovae showed that the Universe is right now undergoing an accelerated expansion, yielding the scientific community to believe that there exists a non-zero dark energy (or cosmological constant, in its simplest form) component. A domination of the term Ω_Λ gives

$$\frac{da}{dt} = H_0 a \Omega_\Lambda^{1/2}, \tag{1.39}$$

hence bringing

$$a \propto e^t. \tag{1.40}$$

Recent constrains on Ω_Λ lead to believe that the dark energy component started to dominate the Universe energy density in a recent time, whose correspondent redshift seems to be of the order of the unity.

In this chapter I gave a synthetic overview of the most important results obtained in Cosmology. The main purpose was giving a wider context to better collocate the original work that will be presented in Part ii and Part ii. The background, however, would not be complete without a proper introduction to the method that has been used in the original investigations addressed in this Thesis: gravitational weak lensing. I will present this topic in the following chapter.

2

GRAVITATIONAL LENSING

The main purpose of modern cosmology is the understanding of Universe's evolution over time, from its very beginning to its fate, knowing the Cosmos' statistical properties and how structures developed or how they will evolve. Most of this is done by means of some theoretical models and via quantities that, defined within such models, parametrize the most important properties of the cosmos: These quantities are called the cosmological parameters. Constraints on the cosmological parameters can be placed in a multiplicity of ways, ranging from the study of the cosmological microwave background, to statistics of the galaxy distribution or of high-redshift objects such as Type Ia supernovae. Diverse methods often probe different scales, are subject to independent systematics, or are sensitive to different cosmological parameters. Gravitational lensing is one of this methods, and has been proposed as a cosmological tool over the last years.

The lensing effect from gravitation is a relativistic phenomenon, due to the fact that, as matter produces curvature in space-time, it also distorts geodesics of that given space-time, causing light trajectories to bend. In cosmology we observe gravitational lensing when light coming from a distant source, e. g. a galaxy or a quasar, passes close to massive objects like clusters of galaxies. As a result, the image of the source galaxy gets distorted. This deformation can be minimal, as in weak lensing, or considerable, like the giant arcs or the Einstein rings produced by strong lensing (see for instance Figure 2.1).

It is intuitive that the amount of deflection that different light bundles will undergo, or, equivalently, the amount of distortion suffered

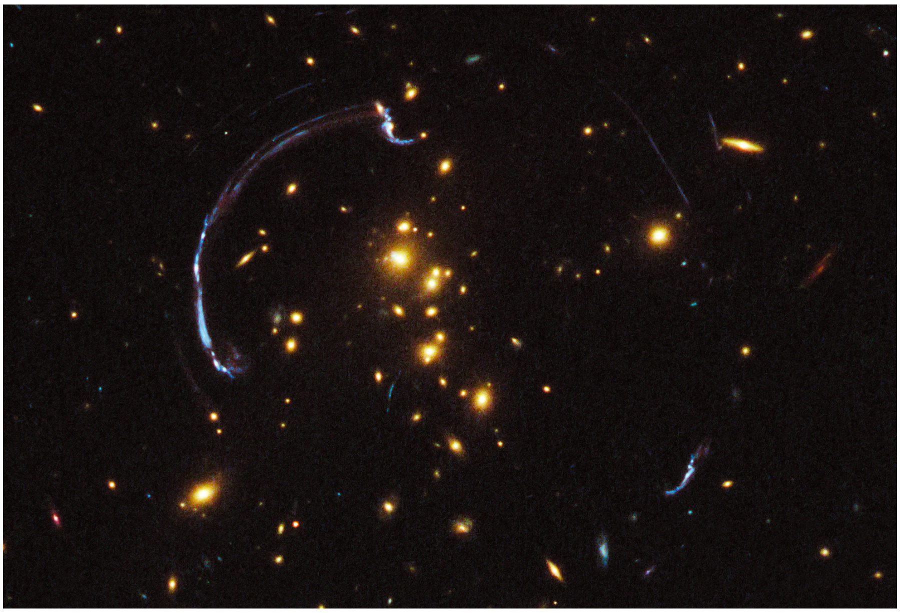

Figure 2.1: Giant arcs due to the effect of gravitational lensing. The cluster RCS2 032727-132623 acts as a lens for a background galaxy, whose image gets extremely magnified and stretched. Credit: NASA, ESA/Hubble.

by a source image, will depend on the mass distribution that lies between the observer and the source. Weak lensing can therefore be used to study the statistics of such a distribution, and infer constraints on cosmological parameter from it. One important advantage of lensing, is that it is sensitive to both baryonic and dark matter, and it is therefore immune, for instance, to systematic errors due to the galaxy bias.

The aim of this Chapter is to give an overview of gravitational lensing. A special attention was devoted to weak lensing, that we adopted as a method for detection of baryon acoustic oscillations and primordial non-Gaussianities of the density distribution (Part ii and Part iii, respectively). In Section 2.1, I will present the basic idea and physics behind lensing, as defined in a quite general context. A declination of the lensing formalism for the specific case of cosmological weak lensing will be treated in Section 2.2. A particular kind of formalism, aiming to derive a 3-dimensional map of the cosmic shear, is introduced in Section 2.3. This method, called 3d weak lensing, is of particular interest for this Thesis, since it was proposed by our work as a tool for detecting baryon acoustic oscillations in the matter power spectrum, as we will see in Part ii.

The content of this chapter is based on Bartelmann and Schneider [2001], Refregier [2003], Bartelmann [2010a], and I refer to these reviews for a more accurate and extended analysis of the topic.

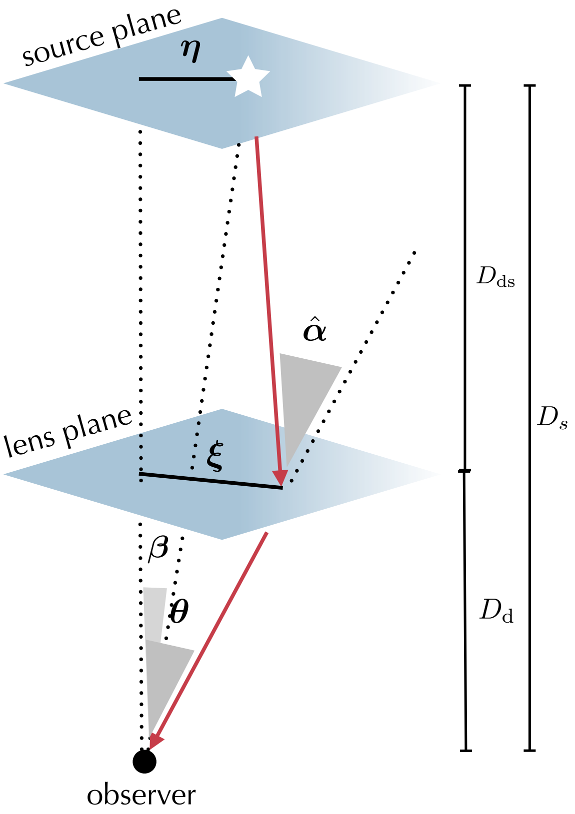

Figure 2.2: The basic lensing process acting when a point-like source is subject to the effect of a single lens.

2.1 LIGHT DEFLECTION BY GRAVITATION

2.1.1 *Lens equation*

The simplest situation that involves the lensing mechanism is drawn in Figure 2.2. Here we have an observer, a source placed at the angular diameter distance D_s and a mass concentration placed in between the two, at distance D_d from the observer and D_{ds} from the source.

thin lens and Born approximations

If the dimension of the lens is negligible with respect to the distances D_s, D_{ds}, and D_d, we can use the *thin-lens approximation*. In this framework, the deflection is assumed to take place instantaneously on the *lens plane*, a surface perpendicular to the line-of-sight and passing through the lens. The *Born approximation*, also often used, supposes that the slightly curved light-ray path can be replaced by a single straight ray.

The path of the light ray traveling to the observer is bent by the action of the lens. As a consequence, the source object will appear at a different position, now subtending an angle β (and not θ, as it would be without the lens) with the line-of-sight.

deflection angle

The deflection is quantified by the angle $\hat{\alpha}$ (see Figure 2.2), that is predicted by general relativity and reads

$$\hat{\alpha} = \frac{4GM}{c^2}\frac{\xi}{|\xi|^2}, \tag{2.1}$$

where ξ is the impact parameter, denoting the distance from the lens, defined on the lens plane[1].

Once we define the relations

$$\theta = \frac{\xi}{D_d} \qquad \text{and} \qquad \beta = \frac{\eta}{D_s}, \tag{2.2}$$

lens equation

then the relation, called *lens equation*, that the geometry of the light ray path has to fulfill is

$$\beta \equiv \theta - \frac{D_{ds}}{D_s}\hat{\alpha}(D_d\theta) = \theta - \alpha(\theta), \tag{2.3}$$

with α being defined as in the equation, and called the *reduced deflection angle*.

If we choose to abandon the simplified model of deflection by a single mass, and

- consider instead a mass distribution, characterized by a density $\rho(\xi, z)$,
- assume that deflection angles are small, i. e. we are dealing with a weak gravitational field,
- make use of the Born approximation,

then in the continuum limit, the vectorial sum of all the small deflections can be written as an integral that looks like

$$\alpha(\xi) = \frac{4G}{c^2}\int d^2\xi' \int dz'\rho(\xi, z)\frac{\xi - \xi'}{|\xi - \xi|^2}. \tag{2.4}$$

deflection angle as the gradient of a potential

It is possible to show that the deflection angle can be expressed as a gradient of a potential ψ. In order to do that, we should first define the *surface mass density* as the mass density projected on a surface that is perpendicular to the line-of-sight:

$$\Sigma(\xi) \equiv \int dz\, \rho(\xi, z). \tag{2.5}$$

Similarly, one can introduce the quantity

$$\Sigma_{cr} = \frac{c^2}{4\pi G}\frac{D_s}{D_d D_{ds}}, \tag{2.6}$$

convergence

called *critical surface mass density*. This term allows us to write a di-

---

[1] this prediction holds only in case the impact parameter is much larger than the Schwarzschild radius, $R_S \equiv 2GM/c^2$, of the lens.

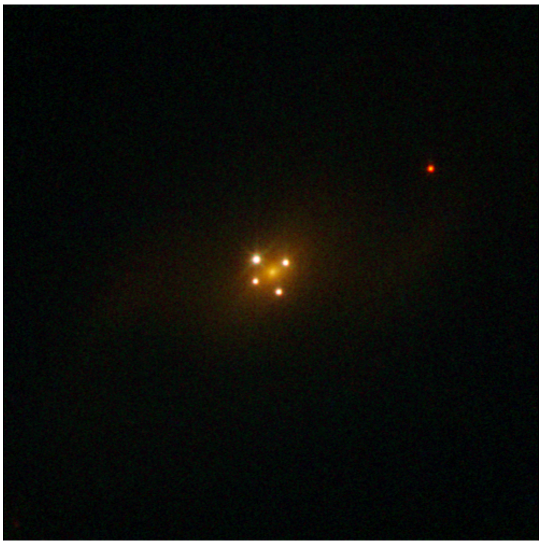

Figure 2.3: The famous Einstein's cross. The quasar QSO 2237+0305 is subject to the lensing by a foreground galaxy, producing four separate images. Credit: ESA/Hubble.

mensionless $\Sigma(\xi)$, such that

$$\kappa(\theta) \equiv \frac{\Sigma(D_d\theta)}{\Sigma_{cr}}, \tag{2.7}$$

that is now depending on the angle θ, rather than on the absolute distance ξ from the lens.

The quantity $\kappa(\theta)$ is called *convergence*. Having $\kappa \geqslant 1$ is a sufficient condition (although not necessary) for the lens equation to have multiple solutions. In other words, a surface mass density larger than the threshold value Σ_{cr}, brings to the development of multiple images (see Figure 2.3). The situation $\kappa = 1$ poses a limit for the discrimination between *weak* and *strong* gravitational lensing. Whenever the convergence is larger than, or of the order of unity, we have strong lensing, featuring multiple images or somewhat extreme distortions of the source image, such as the giant arcs pictured in Figure 2.1; weak lensing, instead, takes place when $\kappa \ll 1$, and is characterized by small image deformations, usually of the order of 2%.

multiple images

weak and strong lensing

Eventually, it is possible to write the total deflection angle in terms of the convergence κ and the angle θ on which it depends:

$$\alpha(\theta) = \frac{1}{\pi}\int d^2\theta'\kappa(\theta')\frac{\theta-\theta'}{|\theta-\theta'|^2}. \tag{2.8}$$

The previous relation makes obvious that the deflection angle can indeed be expressed as a 2-dimensional gradient of a potential ψ,

$$\alpha(\theta) = \nabla\psi(\theta), \tag{2.9}$$

where

lensing potential

$$\psi(\theta) \equiv \frac{1}{\pi} \int d^2\theta' \kappa(\theta') \ln |\theta - \theta|. \tag{2.10}$$

The quantity ψ is called *lensing potential*, and it can be seen as the lensing equivalent of the Newtonian gravitational potential. Moreover, it satisfies the Poisson equation

$$\nabla^2 \psi(\theta) = 2\kappa(\theta). \tag{2.11}$$

2.1.2 *Image distortion*

image deformation of extended sources

A point-like source whose light experiences gravitational lensing by a given mass distribution, will be perceived by an observer as if it was shifted on the plane perpendicular to the line of sight. Things are slightly more complicated for a source of finite size. In this case, light rays coming from different parts of the source will be subject to deflections that do not necessarily have to be of the same entity, depending on the values assumed by the lensing potential on the plane.

In general, light bundles that are deflected differentially will produce distorted images of the source that emitted them. This distortion can be qualitatively and quantitatively described by the Jacobian matrix of the lens equation:

$$A(\theta) = \frac{\partial \beta}{\partial \theta} \tag{2.12}$$

In case we assume the source to be considerably smaller than the scale on which the properties of the lens change, we can expand the lens equation and truncate it at the first order, yielding

$$A(\theta) = \left(\delta_{ij} - \frac{\partial^2 \psi(\theta)}{\partial \theta_i \partial \theta_j} \right) = \begin{pmatrix} 1 - \kappa - \gamma_1 & -\gamma_2 \\ -\gamma_2 & 1 - \kappa + \gamma_1 \end{pmatrix}. \tag{2.13}$$

complex shear

In the previous equation, a new complex quantity has been introduced: The shear γ, that can be written in terms of γ_1 and γ_2 as $\gamma \equiv \gamma_1 + i\gamma_2$, or equivalently $\gamma = |\gamma| \exp(2i\varphi)$, where the factor of two in the exponential reminds us that the shear is a spin-2 field. The shear components are related to the second derivatives of the lensing potential via the relations

$$\gamma_1 = \frac{1}{2} \left(\frac{\partial^2 \psi}{\partial \theta_1^2} - \frac{\partial^2 \psi}{\partial \theta_2^2} \right), \qquad \gamma_2 = \frac{\partial^2 \psi}{\partial \theta_1 \partial \theta_2}. \tag{2.14}$$

It is particularly interesting to have a look at $A(\theta)$ once we divide isotropic and anisotropic distortions. In fact, Equation 2.13 can be rewritten as

$$A(\theta) = (1 - \kappa) \begin{pmatrix} 1 - g_1 & -g_2 \\ -g_2 & 1 + g_1 \end{pmatrix}. \tag{2.15}$$

The term $(1-\kappa)$ acts in a homogeneous fashion, re-scaling the size of the lensed object. The matrix, on the other hand, will produce a distortion of the image through the action of the components of the so called *reduced shear* g, by definition:

reduced shear

$$g_i \equiv \frac{\gamma_i}{1-\kappa}. \tag{2.16}$$

Please note that, in principle, the deformation depends on both shear and convergence, although in the limit of weak lensing ($\kappa \ll 1$), we have $g_i \sim \gamma_i$.

It can be seen that for a generic, circular source, the distortion due to gravitational lensing will produce an elliptical image, whose major and minor axes are given, respectively, by the relations

distortion of a circular source

$$a = \frac{r}{1-\kappa-|\gamma|} \qquad \text{and} \qquad b = \frac{r}{1-\kappa+|\gamma|}, \tag{2.17}$$

where $|\gamma|$ is, of course, the modulus of the complex shear γ.

Lensing is just a geometrical effect, and there is no absorption or emission of photons once the light bundle has left the source. As a consequence, the surface brightness of the source is conserved. Flux is not, though, and a quantification of how much the observed flux differs from the one the source would have without lensing, is given by the *magnification* μ of the light bundle,

magnification

$$\mu \equiv \frac{1}{|\mathrm{det}A|} = \frac{1}{(1-\kappa)-|\gamma|^2}, \tag{2.18}$$

that results to be the inverse of the determinant of the Jacobian matrix $A(\boldsymbol{\theta})$. Magnification is caused by both convergence and shear, thanks to isotropic and anisotropic focusing of light, respectively.

2.2 COSMOLOGICAL WEAK LENSING

In this section, cosmological weak lensing will be analyzed, and all the results obtained so far will be generalized to the case where the lens deflecting light ray paths is not a single mass, but instead the large scale structure of the Universe.

In this framework, the deflection angle is given by an integral of the gradient of the potential, or better the component perpendicular to the line-of-sight. This integral is weighted, though, by the ratio of two angular diameter distances: The one between lens and source, over the one between observer and source. In fact,

deflection angle for LSS-induced lensing

$$\boldsymbol{\alpha}(\boldsymbol{\theta},\chi) = \frac{2}{c^2}\int_0^{\chi} d\chi' \frac{f_K(\chi-\chi')}{f_K(\chi)} \nabla_{\boldsymbol{\theta}} \Phi[f_K(\chi')\boldsymbol{\theta},\chi'], \tag{2.19}$$

where χ is a comoving coordinate.

Similarly as before, it is possible to define an *effective convergence*

effective convergence

$\kappa_{\rm eff}$, and express it in terms of the density contrast making use of the Poisson equation

$$\nabla^2\Phi = \frac{3H_0^2\Omega_{m0}}{2a}\delta. \tag{2.20}$$

The effective convergence is given by

$$\kappa_{\rm eff}(\boldsymbol{\theta},\chi) = \frac{1}{2}\nabla_{\boldsymbol{\theta}}\boldsymbol{\alpha}(\boldsymbol{\theta},\chi), \tag{2.21}$$

hence depending, in principle, on a 2-dimensional Laplacian $\nabla_{\boldsymbol{\theta}} \cdot \nabla_{\boldsymbol{\theta}}$ of the gravitational potential (see Equation 2.19). It is possible to promote this Laplacian to a 3-dimensional one by adding a factor $\partial^2\Phi/\partial\chi^2$. The legitimacy of the operation comes from the fact that derivatives along the line-of-sight average to zero[2]; its convenience, on the other hand, comes from the fact that it permits the exploitation of the Poisson equation, i.e. $\kappa_{\rm eff}$ to be written in terms of the density contrast:

$$\kappa_{\rm eff}(\boldsymbol{\theta},\chi) = \frac{3\Omega_{m0}}{2\chi_H^2}\int_0^{\chi} d\chi \frac{f_K(\chi)f_K(\chi-\chi')}{f_K(\chi)}\frac{\delta[f_K(\chi)\boldsymbol{\theta},\chi]}{a(\chi)}, \tag{2.22}$$

with $\chi_H = c/H_0$ being the Hubble distance.

averaged effective convergence

Assumed that the sources are not all at the same distance χ, but are placed according to a redshift distribution $n(\chi)$, one can construct an effective convergence that is averaged over $n(\chi)$, therefore only depending on the angular coordinates $\boldsymbol{\theta}$:

$$\bar{\kappa}_{\rm eff}(\boldsymbol{\theta}) = \frac{3\Omega_{m0}}{2\chi_H^2}\int_0^{\chi_H} d\chi\, G_\kappa(\chi)f_K(\chi)\frac{\delta[f_K(\chi)\boldsymbol{\theta},\chi]}{a(\chi)}, \tag{2.23}$$

and G_κ a weighting function such that

$$G_\kappa(\chi) \equiv \int_{\chi}^{\chi_H} d\chi' n(\chi')\frac{f_K(\chi-\chi')}{f_K(\chi)}, \tag{2.24}$$

with $n(\chi')$ as the redshift distribution of the sources. Thus, the (averaged) effective convergence is an integral of the cosmological density contrast, all along the unperturbed light path, conveniently weighted by the function G_κ.

2.2.1 *Angular power spectrum*

Although we cannot exactly predict the exact amount of light deflection for a given source, we can infer something about the statistical properties of these deflections. In effect, we have seen that it is possible to express the quantities responsible for image distortions in

---

[2] White and Hu [2000] verified the validity of this statement with numerical simulations.

terms of δ (the *effective shear* can also be defined in a similar way, although calculations are slightly more complex than for the convergence). The density contrast, as already mentioned in the previous chapter (see Section 1.2.2), can be assimilated to a stochastic field and is well described by its two-point statistics.

Limber's equation

Is it possible to construct such statistics also in weak lensing? The answer is yes, and it is given by Limber's equation. Suppose we have a generic, Gaussian stochastic field φ defined in the sky and its power spectrum $P_\varphi(k)$. Then, given any projection of φ on the plane perpendicular to the line-of-sight that can be written as

$$g(\theta) = \int_0^\chi d\chi' q(\chi') \varphi(\chi' \theta), \tag{2.25}$$

(where $q(\chi)$ is a certain weighting function along the line-of-sight) this projection allows its own power spectrum to be written

$$P_g(\ell) m = \int_0^\chi d\chi' \frac{q^2(\chi')}{\chi'^2} P\left(k = \frac{\ell}{\chi'}\right). \tag{2.26}$$

This result holds as far as the weighting function $q(\chi)$ is comparatively smooth with respect to the scales on which the density contrast is expected to vary [Limber, 1953].

The Limber equation can be applied also in our case, in particular if we consider the effective convergence as a projection of the density field δ, and G_κ, or better its rescaling

$$W_\kappa(\chi) = \frac{3\Omega_{m0}}{2\chi_H^2} \frac{G(\chi) f_K(\chi)}{a}, \tag{2.27}$$

angular power spectrum

as its weighting function. These assumptions bring us to the following expression for the angular power spectrum of the lensing convergence

$$C_\kappa(\ell) = \int_0^{\chi_H} d\chi \frac{W_\kappa^2(\chi)}{\chi^2} P_\delta\left(k = \frac{\ell}{f_K(\chi)}\right). \tag{2.28}$$

Moreover, a elementary Fourier analysis can show that the shear power spectrum, derived in an analogous way, is exactly identical to the convergence one

$$C_\kappa(\ell) \equiv C_\gamma(\ell), \tag{2.29}$$

since both κ and γ depend on the second derivative of the lensing potential.

2.2.2 *Measuring the lensing distortions*

power spectrum sensitivity to cosmological parameters

The lensing convergence (or shear) angular power spectrum defined in Equation 2.28 is particularly interesting because of its sensitivity to cosmological parameters, via the Ω_m factor and of course via the density contrast two-point statistics $P_\delta(k)$, and its evolution with time.

shear from ellipticity measurements

In principle, there is no way to know exactly how, and by how much, the image of a single galaxy is distorted by gravitational lensing. Nonetheless, one can still infer statistical deformations once there is a larger sample of galaxies. Suppose that the observed ellipticity of a galaxy is a sum of two effects: Its *intrinsic* ellipticity, and the shear γ (we are in the weak-lensing limit, therefore $\kappa \ll 1$ and its effect on the image shape distortion is negligible). In such a case, the two-point correlation function of the observed ellipticity ϵ_i^{obs} can be written

$$\begin{aligned}\langle\epsilon_i^{\text{obs}}\epsilon_j^{\text{obs}}\rangle &= \langle(\epsilon_i^{\text{int}}+\gamma_i)(\epsilon_j^{\text{int}}+\gamma_j)\rangle \\ &= \langle\epsilon_i^{\text{int}}\epsilon_j^{\text{int}}\rangle + \langle\epsilon_i^{\text{int}}\gamma_j\rangle + \langle\gamma_i\epsilon_j^{\text{int}}\rangle + \langle\gamma_i\gamma_j\rangle \\ &\simeq \langle\gamma_i\gamma_j\rangle, \end{aligned} \tag{2.30}$$

where ϵ^{int} is the intrinsic ellipticity. The main assumption done in weak lensing (and in the last equivalence of the previous equation) is that there are neither correlations between the intrinsic ellipticities of galaxies ($\langle\epsilon^{\text{int}}\epsilon^{\text{int}}\rangle$), nor between ϵ_i^{int} and the surrounding tidal field ($\langle\epsilon^{\text{int}}\gamma\rangle$). In this way, the correlation function between observed ellipticities equals the shear two-point statistics.

intrinsic alignments

In reality, this simplification is not completely exact. Intrinsic alignments between galaxies that formed in a common environment do exist, and can partly contaminate the results if not properly taken into account. See Schäfer [2009] for a review on the subject.

2.3 3D WEAK LENSING

line-of-sight averaging is not necessary

The expression for the effective covariance in terms of the density contrast (Equation 2.22) shows that, originally, this is a 3-dimensional quantity, depending on the distance χ between the source and the observer. Averaging κ_{eff} over the supposed redshift distribution of the sources has become common practice over the years, leading to analyses of 2-dimensional shear fields. Performing this simplification has been a mere consequence of poor measurements of individual galaxy distances.

This weighing, though, is not necessary if we can know such distances with good approximation. Upcoming surveys such as Euclid[3] or DES[4], able to measure galaxy photometric redshift with high accuracy, allow to use this z as a good and precise estimate of individual galaxy distances.

3d expansion of lensing observables

Heavens [2003] was the first to develop a framework to fully exploit the gain of information coming from a 3d weak lensing analysis. The main idea is to perform a special spectral expansion of lensing

---

[3] euclid-ec.org

[4] darkenergysurvey.org

observables, like the convergence or the shear[5] (a detailed description of the theory can be found in Castro et al. [2005], Massey et al. [2007], Heavens et al. [2006], Kitching et al. [2008a]).

spherical harmonics and spherical Bessel functions

A combination of spherical harmonics and spherical Bessel functions, respectively taking care of the angular and radial components, is the most natural choice for a Fourier expansion in spherical coordinates. In fact, such a combination is an eigenfunction of the Laplacian in spherical coordinates, and turns out to be particularly useful when we want to express all the lensing quantities in terms of the density field. For a generic scalar field $f(\mathbf{r})$, such an expansion reads

$$f_{\ell m}(k) \equiv \sqrt{\frac{2}{\pi}} \int d^3 r \, f(\mathbf{r}) \, j_\ell(kr) Y^*_{\ell m}(\theta), \tag{2.31}$$

where j_ℓ and $Y_{\ell m}$ are, respectively, a spherical Bessel function of the first kind and a spherical harmonic.

Quantities like the lensing potential, the shear, or the convergence can thus be decomposed and expressed in terms of coefficients of this expansion. For the convergence, for instance, we have:

$$\kappa_{\ell m}(k) \equiv \sqrt{\frac{2}{\pi}} \int \chi^2 d\chi \, d\theta \, \kappa(\theta, \chi) \, j_\ell(k\chi) Y^*_{\ell m}(\theta). \tag{2.32}$$

An estimator of $\kappa_{\ell m}$ can be constructed, that in the case of a full-sky survey of galaxies is given by the relation

$$\bar{\kappa}_{\ell m}(k) = \frac{3\Omega_m}{2\chi_H^2} \frac{\ell(\ell+1)}{2} \frac{B_\ell(k, k'')}{(k'')^2} \, \delta_{\ell m}(k''). \tag{2.33}$$

mode-coupling matrix

As we will see in Section 4.3 (Part ii), where a more detailed derivation of this quantity will be provided, the matrix $B_\ell(k, k'')$ carries all the information on additional mode couplings coming from lensing, the galaxy redshift distribution, and uncertainties in the measurement of the photometric redshift.

Statistics of the convergence (or shear, of course) coefficients[6] in the considered 3d expansion depend on that of the coefficients $\delta_{\ell m}$ without any averaging along the line-of-sight distribution of galaxies. The power spectrum of $\delta_{\ell m}$ is exactly equal to the spectrum of the density contrast itself [Castro et al., 2005], and therefore inherits its sensitivity to cosmological parameters. Moreover, the absence of a line-of-sight weighing results in a more direct correspondence between a 3d lensing statistics and the underlying matter power spectrum, at least with respect to the classical 2d weak lensing approach.

valuable tool for dark energy study

It has been shown [Heavens et al., 2006] that a 3d analysis would be

---

[5] please note that such observables depend on the gravitational potential, that evolves with time and is not perceived as homogeneous by galaxies that are lensed under its effect. It is more correct, then, to refer to the transform of such quantities as the transform of the corresponding, homogeneous fields that exist in correspondence of the time on which the galaxy emitted its light [Castro et al., 2005]

[6] in this work only 3d two-point statistics have been considered; for higher order statistics please refer to Munshi et al. [2011].

of particular interest regarding constraints on the dark energy equation of state, providing a reduction of the marginalized errors on its coefficients w_0 and w_a, especially when combined to measurements from CMB and baryon acoustic oscillations experiments.

possible application for baryon acousticc oscillations

The lack of an averaging along the line-of-sight source distribution, on the other hand, resulting as already said in a tighter relation between the 3d weak lensing and the matter power spectra, leads to the idea of exploiting this kind of approach for detecting localized features of the matter $P(k)$, e. g. baryon acoustic oscillations (that will be introduced in the next chapter). Such features are usually smoothed out from the classical weak lensing power spectrum, due to the presence of the weighting function defined in Equation 2.24. On the contrary, they are inherited by the 3d weak lensing spectrum, and their detectability depends on the sensitivity of the 3d method. In Part ii of this Thesis, I will give an overview on baryon acoustic oscillations as a cosmological tool, and on our predictions regarding the feasibility of their detection with a 3d weak lensing approach [Grassi and Schäfer, 2013].

Part II

DETECTING BARYON ACOUSTIC OSCILLATIONS BY 3D WEAK LENSING

3

BARYON ACOUSTIC OSCILLATIONS

Baryon acoustic oscillations are features of the matter power spectrum $P(k)$, where they show up as a damped series of peaks and troughs. As the power spectrum is defined in Fourier space, it makes sense to identify a BAO counterpart in configuration space: the baryon acoustic peak, namely a bump-shaped feature of the two-point matter correlation function. Both this peak and BAO are manifestation of the same phenomenon: In fact, they originate during the decoupling between matter and radiation, and represent a preferred clustering scale in the global matter distribution. As we will see, BAO have been suggested to be among the most powerful and promising new cosmological tools for cosmological parameter constraining. In particular, they can help us studying and determining our Universe's expansion history. For a recent review, please see Bassett and Hlozek [2010].

In this Chapter, I will briefly introduce baryon acoustic oscillations by explaining, in Section 3.1, what kind of physical processes they originate from, whereas in Section 3.2 I will analyze BAO's potentialities as a cosmological tool and, more specifically, as a statistical standard ruler.

3.1 THE PHYSICS OF BARYON ACOUSTIC OSCILLATIONS

3.1.1 *The plasma era*

A plasma *is defined as a globally neutral collection of free-moving charged particles*

During the first $300-400$ kyrs of the Universe, the baryonic and radiation components of the Cosmos are in the form of a hot, dense plasma composed by electrons, nuclei and photons. All along this epoch, radiation and baryons result tightly coupled thanks to Thomson scattering by electrons, a mechanism describing an elastic collision between a free charged particle and a photon. As long as the timescale of the scattering is much smaller than the expansion timescale $t_H(z) = H(z)^{-1}$, we observe a continuous momentum transfer between baryonic matter and radiation, causing them to be in thermal equilibrium. If we define the average time between two Thomson scatterings to be

$$t_s = \frac{1}{\sigma_T n_e}, \tag{3.1}$$

where σ_T is the Thomson cross section and n_e the number density of free electrons, it is clear that, as long as n_e is large enough to make the relation $t_s \ll t_H$ hold, baryons and photons will be coupled, and their temperatures will evolve in the same manner. This state of course causes the plasma to be opaque to electromagnetic radiation.

acoustic waves in the primordial photon-baryon plasma

One important consequence of coupling between baryons and radiation, is that any perturbation in the plasma behaves like an acoustic wave, thanks to the competing forces of gravity and radiation pressure. In simple words:

1. given a certain, primordial, perturbation in density, e. g. an overdensity, gravitation acts to compress the plasma in correspondence of the overdensity itself;
2. this process also increases photon density;
3. the temperature rises, and so does the radiation pressure,
4. causing the plasma to expand.

A more rigorous analysis can be found in Eisenstein et al. [2007b], where they remind that, given the rapidity of the scattering compared to time it takes to travel along the wavelength of a generic perturbation, the Euler equation can be expanded in powers of the term $k/\dot{\tau}$, namely the Compton free path $\lambda_s = \dot{\tau}^{-1}$, over a wavelength $\lambda \propto k^{-1}$, where k is the perturbation's wavenumber, $\dot{\tau} = a\sigma_T n_e$ is the differential optical depth, and the dot denotes a derivative with respect to conformal time $\eta = \int dt/a$, while a is, as usual, the scale factor [Montanari and Durrer, 2011]. In this way it is possible to write the evolution of a single Fourier mode of the plasma perturbation in the so called tight coupling approximation:

$$\frac{d}{d\eta}[(1+R)\dot{\delta}]+\frac{k^2}{3}\delta=-k^2(1+R)\Phi-\frac{d}{d\eta}[3(1+R)\dot{\Psi}], \qquad (3.2)$$

[Peebles and Yu, 1970; Doroshkevich et al., 1978; Ma and Bertschinger, 1995] where Φ is the gravitational potential, Ψ the perturbation of spatial curvature and

$$R \equiv \frac{3\rho_b}{4\rho_\gamma} \qquad (3.3)$$

is the ratio between baryon and photon momentum density. It is easy to see that Equation 3.2 describes a driven oscillator with original frequency $c_s k$, where c_s is defined as the sound speed

$$c_s=\frac{c}{\sqrt{3(1+R)}}, \qquad (3.4)$$

and can assume at most the value of $c/\sqrt{3}$. The period decay can anyway be neglected for small values of R, typical for the range of redshifts here considered ($z \gtrsim 1000$).

3.1.2 *After recombination*

When considering the timeline of Universe's evolution, some events, more than others, mark exceptional changes in the state and physical properties of the Cosmos's content. The epoch of recombination and decoupling is undoubtedly part of this category. We have seen that during the plasma era, perturbations are not allowed to grow in amplitude, on the contrary they propagate as acoustic waves with a certain sound speed (Equation 3.4); there comes a moment, though, when things change. As both temperature and density of the plasma decrease due to cosmic expansion, the equilibrium state for baryons moves towards a situation where nuclei and electrons combine together [Zeldovich et al., 1969; Peebles, 1968], no longer being ionized:

Recombination

$$H^+ + e^- \rightleftharpoons H+\gamma. \qquad (3.5)$$

By convention, the instant when 50% of baryonic matter is in the form of neutral atoms is called *recombination* time $t_{rec} \sim 360000$ yrs, corresponding to a redshift of $z_{rec} \sim 1090$ [Komatsu et al., 2011; Planck Collaboration et al., 2013a].

Shortly after this process begins to take place, scattering between photons and electrons starts to become more and more sporadic. In other words: The Hubble distance is now comparable or even smaller than the photon mean free path. Photons gradually stop noticing the

Decoupling and drag epoch

presence of baryons, meaning that they *decouple* from them and that the total optical depth up to the present becomes smaller than one. This is when last scattering and cosmic microwave background originate. As a consequence of recombination, also baryons stop noticing photons, although these two specular processes do not necessarily have to take place at the same time. In fact, since there are vastly more γ than baryons, photon's optical depth approaches 1 earlier than baryon's τ_b. The moment when the baryon optical depth

$$\tau_b(\eta) \equiv \int_{\eta}^{\eta_0} d\eta \frac{\dot{\tau}}{(1+R)} \tag{3.6}$$

drops below unity, is when baryons are released from the drag of photons due to Compton scattering, and is usually called *drag epoch* [Hu and Sugiyama, 1996]. From this time on, matter and radiation evolve separately: Photons now freely propagate, the Universe is already transparent to electromagnetic radiation, and baryons must now be treated as a pressureless species, meaning that they can now cool down at a different rate compared to photons, and eventually collapse. Of course the tight coupling approximation seen in Equation 3.2 doesn't hold anymore, and perturbations in the baryon density can no longer propagate as acoustic waves after decoupling. The drag epoch doesn't coincide, in principle, with recombination, although the two moments are comparable and both depend on Ω_m and Ω_b. A fitting formula for the derivation of the drag redshift was proposed by Eisenstein and Hu [1998]:

$$z_{\mathrm{drag}} = 1291 \frac{(\Omega_m h^2)^{0.251}}{1+0.659(\Omega_m h^2)^{0.828}} \left(1 + b_1 (\Omega_b h^2)^{b_2}\right), \tag{3.7}$$

with

$$\begin{aligned} b_1 &= 0.313(\Omega_m h^2)^{-0.419}[1+0.607(\Omega_m h^2)^{0.674}], \\ b_2 &= 0.238(\Omega_m h^2)^{0.223}. \end{aligned} \tag{3.8}$$

Evolution of a point-like density perturbation

An interesting and instructive analysis of the evolution of a point-like overdensity in configuration space was carried out by Eisenstein et al. [2007b], as shown in Figure 3.1. Here they analyze the mass profile behavior of such an overdensity with respect to a radial coordinate, as time passes by (different panels). The density perturbation is initially present in all species, i. e. dark matter, photons, baryons, and neutrinos. The figure clearly displays how, while at first the wave propagates through baryons and photons as a single pulse, after $z \sim 1100$ (time of recombination) this starts to be not valid anymore. In fact, after recombination photons can freely propagate, not supplying radiation pressure to baryons; the sound speed obviously drops and this causes the baryons perturbation to slow down and eventually freeze. Not only does the perturbation stall, but it grows by gravitational instability.

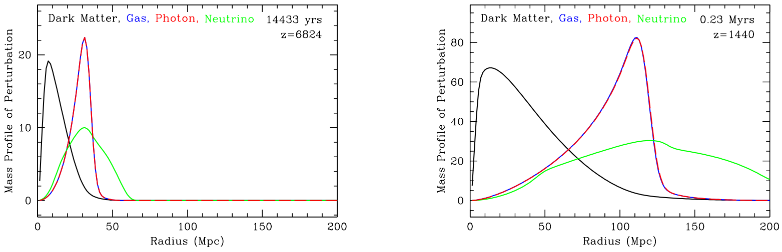

(a) $z = 6824$, $t \sim 1.4 \cdot 10^4$yrs

(b) $z = 1440$, $t \sim 2.3 \cdot 10^5$yrs

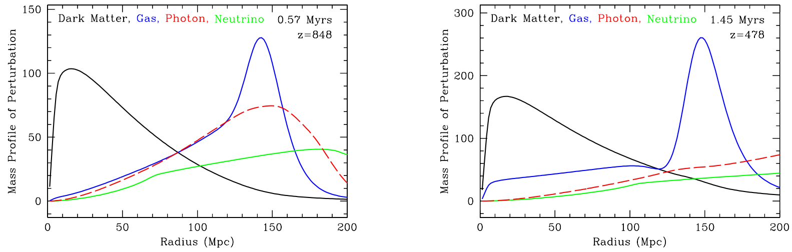

(c) $z = 848$, $t \sim 5.7 \cdot 10^5$yrs

(d) $z = 478$, $t \sim 1.45 \cdot 10^6$yrs

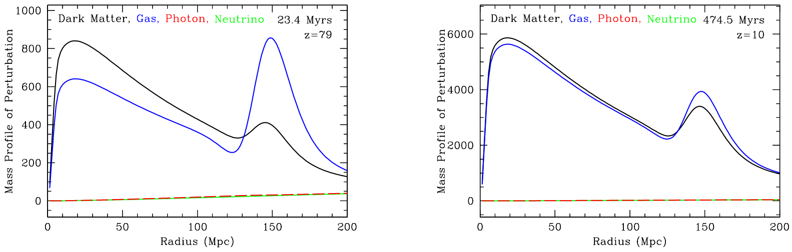

(e) $z = 79$, $t \sim 2.3 \cdot 10^7$yrs

(f) $z = 10$, $t \sim 4.7 \cdot 10^8$yrs

Figure 3.1: The evolution with time of the radial mass profile of a point-like overdensity initially located at $r = 0$. Different panels display the mass profiles at chosen redshifts, while the colors represent mass profiles of dark matter (black), baryons (blue), photons (red), neutrinos (green). Time increases (and z gets smaller) as we look at panels from left to right, and from top to bottom. The first two panels show how coupling between baryons and photons makes the perturbation evolve in an identical way for the two species. A smoothing of the DM overdensity over $r > 0$, due to gravitational interaction with the plasma, is also visible from Figure 3.1b on. After Figure 3.1c it becomes evident that photons have already decoupled from matter and start streaming away, while the baryon perturbation gradually stops at a radius ~ 150 Mpc. Both baryon and DM overdensity grow in amplitude and interact gravitationally, yelding a double-peaked mass profile like the one in Figure 3.1f. Figure taken from Eisenstein et al. [2007b].

In this scenario, what remains after recombination and decoupling are two overdensities:

- the CDM's one, located at the center;

- the baryons' one, that from t_0 to t_{rec} managed to travel up to a distance r_s from the center, and that now forms a shell around the origin.

The distance covered by the baryons perturbation, i. e. the radius of the overdensity spherical shell, is of course related to the size of the sound horizon at the drag epoch, that is assumed to be comparable to the sound horizon at recombination [Eisenstein and White, 2004]:

$$\begin{aligned} r_s &= \int_0^{t_{\text{rec}}} c_S(1+z)dt \\ &= \frac{1}{\sqrt{\Omega_m H_0^2}} \frac{2c}{\sqrt{3z_{\text{eq}}R_{\text{eq}}}} \ln\left[\frac{\sqrt{1+R_{\text{rec}}}+\sqrt{R_{\text{rec}}+R_{\text{eq}}}}{1+\sqrt{R_{\text{eq}}}}\right], \end{aligned} \tag{3.9}$$

where z_{eq} is the redshift at the moment of equality between matter and radiation, and R_{eq}, R_{rec} are the baryon-photon momentum density ratios for, respectively, equality and recombination, giving r_S of the order of 150 Mpc. Interacting via gravitation, CDM and baryons drag each other, eventually reaching the intermediate situation shown in the last panel of Figure 3.1, where the final radial mass profile features a peak close to the perturbation origin, and a secondary one located at the distance the baryon-photon acoustic wave could travel before recombination.

Galaxies and collapsed objects tend to form in correspondence of overdensities. As a consequence, the scale of the sound horizon at recombination remains as a characteristic separation length in the matter distribution, because there is where galaxies will be more likely to form. In other words, it can be considered as a preferred scale for matter clustering. Since, of course, the overall baryon distribution will consist in a superposition of perturbations similar to the one considered, this length can only be recovered statistically. In effect, it will appear in the correlation function as a peak[1] around the scale r_s.

The power spectrum and the two-point correlation function of the matter distribution form a Fourier pair. Therefore, since the transform of a single bump gives a harmonic sequence, the baryon acoustic peak will be visible in $P(k)$ as wiggles (BAO) whose wavelength is strictly related to the sound horizon scale at the time of recombination $k_S = 2\pi/r_S$. Power spectra with and without the presence of a baryonic components are plotted in Figure 3.2.

---

[1] it is a peak because we are dealing with an excess of clustering at a certain scale; a scarcity of clustering, on the other hand, would produce a dip.

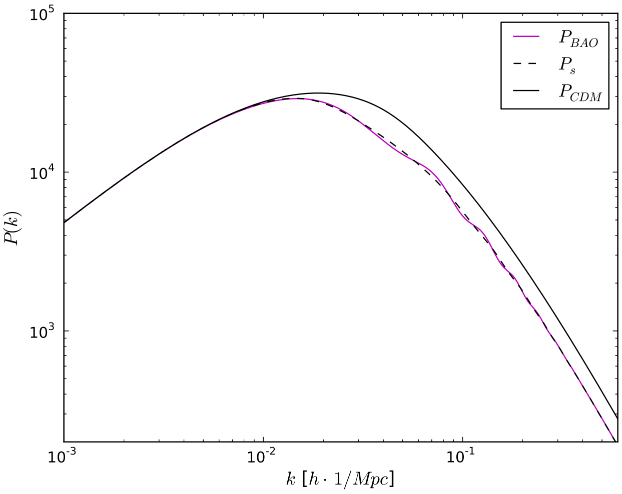

Figure 3.2: The difference between a CDM-only power spectrum (black, solid line), a power spectrum where also a baryonic presence was considered, in the amount of $\Omega_b = 0.44$ (magenta line) and the corresponding smooth spectrum (black, dashed line). We can also observe that the presence of baryons acts as an overall suppression in intermediate and small scales. The spectra were calculated using the prescription by Eisenstein and Hu [1998]

3.2 BARYON ACOUSTIC OSCILLATIONS AS A COSMOLOGICAL TOOL

3.2.1 *What is a statistical standard ruler*

Since Riess et al. [1998] and Perlmutter et al. [1999] proved for the first time that the Universe was accelerating (see Figure 3.3), cosmologists have strived for years aiming to explain what kind of mechanism is behind this peculiar type of expansion. Whether be this phenomenon related to the cosmological constant, or to a *dark energy* with some still unknown equation of state, there is no doubt that the understanding of the expansion of the Universe relies on our ability to investigate the redshift-distance relation, unless we consider, for instance, modified-gravity theories.

The expansion rate in function of redshift, i. e. the Hubble parameter $H(z)$, can be inferred by measuring quantities such as the angular diameter distance

$$d_A = \frac{c}{1+z} \int_0^z \frac{dz}{H(z)} \tag{3.10}$$

or the luminosity distance (see Section 1.1.4)

$$\begin{aligned} d_L &\equiv \sqrt{\frac{L}{4\pi F}} \\ &= (1+z)^2 d_A. \end{aligned} \tag{3.11}$$

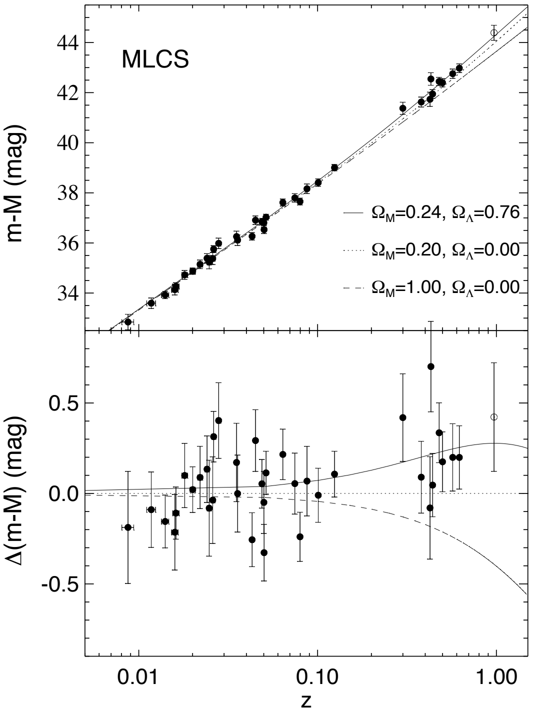

Figure 3.3: Difference between relative and absolute magnitude (top panel) for a sample of Type Ia supernova as a function of their redshift. The lines represent the expected behavior for different cosmologies, while the bottom panel displays the residuals with respect to the reference model, characterized by $\Omega_m = 0.2$ and $\Omega_\Lambda = 0$. The data appear to give evidence for a flat Universe with a non-zero Λ-component, implying an acceleration of the cosmic expansion. Figure taken from Riess et al. [1998].

If we assume the expansion to be ascribable to the effect of dark energy, and described by its density parameter Ω_Λ and its equation of state (assumed that it can be treated as an ideal fluid)

$$w(z) = \left.\frac{p_\Lambda}{\rho_\Lambda}\right|_z , \tag{3.12}$$

Hubble parameter as a proxy for dark energy contribution

then the Hubble parameter for a flat, matter and dark-energy dominated universe can be written:

$$H(z) = H_0 \sqrt{\Omega_{m0}(1+z)^3 + \Omega_{\Lambda 0} \exp\left[3 \int_0^z \frac{1+w(z)}{1+z} dz\right]}, \tag{3.13}$$

where H_0, Ω_{m0}, and $\Omega_{\Lambda 0}$ are, respectively, the expansion rate parameter, the matter density and dark energy density parameters at present time. The Hubble parameter is thus the fundamental observable related to $\Omega_{\Lambda 0}$ and $w(z)$.

standard candles and standard rulers

To measure quantities like d_L and d_A and their trend with redshift, though, we need respectively

- *standard candles*: Objects whose absolute magnitude, or luminosity, is known or, alternatively, whose luminosity change with redshift in a well understood way;
- *standard rulers*: Objects of known absolute size, or whose size-redshift relation is well acknowledged.

Rulers and candles are especially useful, in cosmology, for solving issues related to the degeneracy that exists between radial distance, intrinsic size (or luminosity) of the object, and space curvature. In fact, if we observe an object to be small (or faint), theoretically we are not allowed to know whether it is intrinsically small (faint), whether it looks like this because it is very far away from us, or whether space curvature acts as a lens and distorts its shape. Standard rulers and candles can, in principle, break this degeneracy.

Several examples of this two very special category of objects can be found in cosmology. Type Ia supernovae (SNIa) are probably the most famous among standard candles : Since their collapse always occurs at the Chandrasekar mass, they happen to have a characteristic brightness at the peak of their light curve, that can be used as standard candle after appropriate calibrations. Unlike other standard candles (e. g. Cepheids, RR Lyrae), Type Ia supernovae are particularly suited for cosmology thanks to their extremely high brightness, that makes them visible even at cosmologically relevant distances. Riess et al. [1998], for instance, used supernovae up to $z \sim 1$ in their study, corresponding to a distance of the order of the Gpc.

Concerning cosmological standard rulers, some have been proposed over the years: Double-lobed [Buchalter et al., 1998] and ultra-compact radio sources [Kellermann, 1993; Gurvits, 1994; Jackson and Dodgson, 1997], or even galaxy clusters [Allen et al., 2002; Schäfer et al., 2005; Mantz et al., 2008]. All of them gave results similar or at least compatible with the ones obtained by Riess et al. [1998] from SNIa.

statistical standard rulers

A slightly different class of standard rulers also exists. Imagine to have, rather than an object, a particular behavior or phenomenon that has a characteristic, known scale, e. g. clustering of galaxies. In this case we are not dealing with one single object of known size, but instead with a certain distribution whose characteristic scale can be recovered only statistically (see Figure 3.4): Such a tool is called *statistical standard ruler*.

3 rules for the perfect standard ruler

The ideal (statistical) standard ruler allows for very accurate constraints on $H(z)$, and in order to achieve that it should satisfy the following properties[2]:

---

[2] these considerations are based on Martin White's lectures on BAO, that he kindly provides on mwhite.berkeley.edu

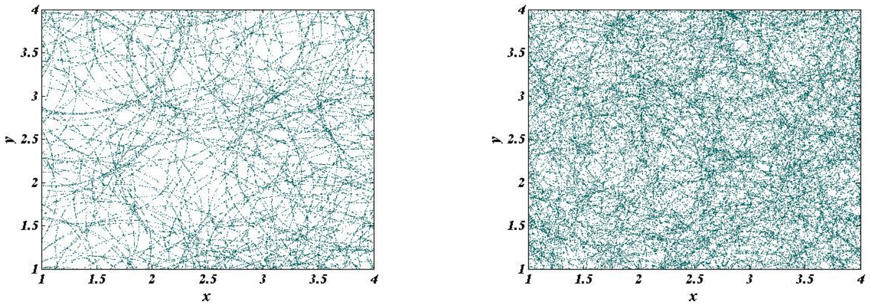

Figure 3.4: The concept behind statistical standard rulers, taken from Bassett and Hlozek [2010]. It shows a very simple, two-dimensional galaxy distribution featuring a preferred clustering scale. In the left panel, the relatively small number of galaxies makes the correlation visible to the naked eye. The right panel, instead, shows a distribution with the same characteristics but where the number of galaxies is much larger: In this case, the distribution's characteristic scale is not obvious anymore and can only be regained statistically, by means of a correlation function.

- it should be possible to calibrate the ruler over the largest possible redshift interval (i. e. we can precisely predict how the ruler size evolves with z);
- the ruler size should be small enough to be measured with high statistical accuracy over the volume of the surveys;
- it should be possible to get a high-precision measurement of the ruler.

We will see in the following sections that baryonic features in the matter distribution statistics can satisfy all of these properties.

3.2.2 *Constraining cosmological parameters with baryon acoustic oscillations*

Since BAO and the baryon acoustic peak are manifestations of the existence of a preferred clustering scale, and since this scale's absolute value can be relatively easily calculated from theory, they make excellent statistical standard rulers, as it was first suggested by Cooray et al. [2001] and later developed in more detail by Eisenstein [2003] and Blake and Glazebrook [2003].

By measuring both the transverse, angular size of the BAO feature and its interval in redshifts at different z (namely, transverse and radial Fourier modes of the matter distribution) we can get estimates of, respectively, $d_A(z)$ and $H(z)$. Since the physical, absolute scale of BAO is known, they are not considered an Alcock-Paczynski test [Alcock and Paczynski, 1979] and the two quantities themselves, rather than their product, can be inferred separately.

Baryon acoustic oscillations fulfill, in theory, all the characteristics of a good ruler, in fact:

- within a certain grade of accuracy, BAO scale is predicted by well understood, linear theory and depends mainly on matter and baryon density, meaning that CMB constrains on Ω_m and Ω_b, for instance, can be used to accurately calibrate the BAO ruler;
- recent galaxy surveys have reached sufficiently large volumes so that BAO features can be detected in the galaxy density distribution;
- the oscillatory behavior (peak) of the matter power spectrum (two-point correlation function) is a relatively sharp and easily recognizable feature to detect.

3.2.2.1 *Observing baryon acoustic oscillations*

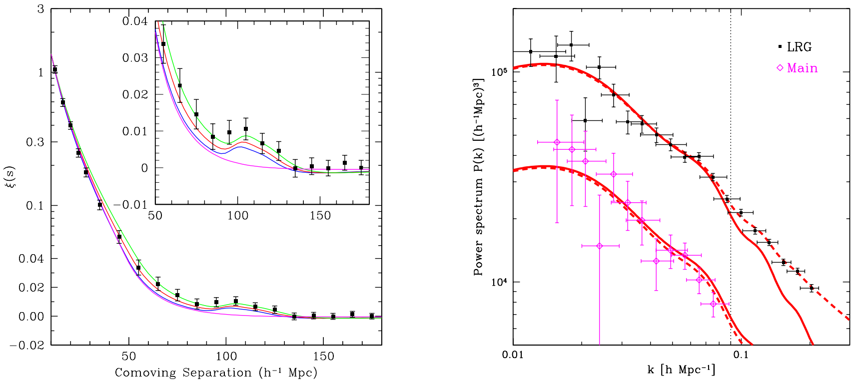

(a) (b)

Figure 3.5: On the left, the baryon acoustic peak in the correlation function of a SDSS galaxy sample. The three upper lines represent models with, from top to bottom, $\Omega_m h^2 = 0.12, 0.13, 0.14$, while for all three $\Omega_b h^2 = 0.024$; the bottom line shows a model with no baryons, and therefore no acoustic peak. The right panel, on the other hand, exhibits a power spectrum derived from an SDSS (top curve) and an LRG (bottom curve) galaxy sample. Solid and dashed lines represent, respectively, a ΛCDM fit to WMAP3 [Spergel et al., 2007] data, and a fit that includes also non-linear corrections. Left and right panels are taken respectively from Eisenstein et al. [2005] and Tegmark et al. [2006].

The two primary channels for observing a baryon acoustic signature are the power spectrum of CMB temperature anisotropies and statistics of galaxy distributions. While oscillatory features in the CMB power spectrum were already observed by WMAP [Hinshaw et al., 2003, 2007; Nolta et al., 2009; Larson et al., 2011], BAO signatures in the galaxy distribution have been detected for the first time by Eisenstein et al. [2005] in the SDSS survey, as shown in Figure 3.5a.

Further detection have been carried out, ever since, in particular with SDSS [Eisenstein et al., 2005; Padmanabhan et al., 2007; Percival et al., 2007b, 2010; Kazin et al., 2010b; Padmanabhan et al., 2012; Mehta et al., 2012], the 2-Degree Field Galaxy Redshift Survey [2dFGRS, Percival et al., 2007a; Beutler et al., 2011], the WiggleZ-survey [Parkinson et al., 2012] and Lyman-α forest data coming from the Baryon Oscillation Spectroscopic Survey (BOSS) [Busca et al., 2012; Slosar et al., 2013]. Moreover, [Gaztañaga et al., 2009a; Kazin et al., 2010a; Gaztañaga et al., 2009b] managed to observe both longitudinal and transverse modes in the galaxy distribution. All the observations confirmed what already determined in CMB measurements, namely spatial flatness and low matter density when a flat geometry is assumed as a prior.

A very interesting insight on issues related to model testing and parameter estimation with baryon acoustic oscillations was made by [Cabré and Gaztañaga, 2011], who find that although BAO cannot be used for model selection, yet, they can still help to constrain cosmological parameter once a specific model is assumed to be valid.

3.2.3 *Nonlinear effects and observational complications*

In an ideal frame, as White [2005] nicely phrased it, we should be able to measure the linear-theory, matter power spectrum, in real space. What is usually measured, instead, is

- the *non-linear*,
- *galaxy* power spectrum,
- in *redshift* space.

Although it seems that BAO probably have the lowest systematic uncertainties among the methods used for studying cosmic expansion [Albrecht et al., 2006], it is clear that these three factors have repercussions on the detection of the BAO scale, degrading the reconstruction of the peak position, or, equivalently, of the oscillations wavelength.

redshift space distortions

Redshift space must be considered every time we take a galaxy's z as an estimate of its distance. In reality, a galaxy's redshift is determined not only by its distance from us, via the Hubble relation, but also by its peculiar velocity, not to mention the fact that the redshift uncertainty of the survey, σ_z, also plays a role. As a result, what we observe is an altered version of real space, with misestimates of true galaxy distances leading to the so called *redshift space distortions*. These kind of deformations are mainly radial, and will therefore mostly affect measurements of the Hubble expansion rate $H(z)$, leaving the transverse BAO scale derivation (and subsequently d_A

measurements) almost unblemished. The main effect is a suppression of the power spectrum $P(k)$

$$P_{obs}(k) = P(k) \exp\left[-\left(k_{||}\sigma_z \frac{1+z}{H(z)}\right)^2\right], \tag{3.14}$$

over the radial modes $k_{||}$ [Seo and Eisenstein, 2003], where $P_{obs}(k)$ is of course the resulting, observed power spectrum. This suppression clearly depends on the redshift uncertainty σ_z, and it acts more strongly on higher order oscillations. Its main effect is to smear out the baryon acoustic peak in the correlation function. I refer to Blake et al. [2006], Benitez et al. [2008], Cai et al. [2009], Simpson et al. [2009] for a more detailed analysis of the subject.

distortions due to non-linear structure formation

An other source of complications is undoubtedly non-linear structure formation. At $z < 1$, there is already a deviation of the non-linear $P(k)$ from the linear one concerning wave numbers that contain acoustic information [Eisenstein et al., 2007b]. Since non-linear collapse tend to displace matter with respect to its initial position by an order of ~ 10 Mpc, due to an object's combined interactions with all the other density fluctuations, a broadening of the baryon acoustic peak will be observed. A broadening that adds to the natural, finite width of the peak of ~ 10 Mpc h^{-1}, due to Silk damping [Silk, 1968]. In $P(k)$, this will be observed as a damping of the oscillations at higher k (smaller scales). It is straightforward that a broadening of the peak will have important consequences in the precision with which the position of the peak itself, i.e. the scale of the sound horizon r_s, is measured. Mode-mode couplings in the density distribution induced by non-linear structure formation also play a role, producing a shift in the baryon acoustic peak. This phenomenon has been thoroughly analyzed by Crocce and Scoccimarro [2006b], Crocce and Scoccimarro [2006a] and Crocce and Scoccimarro [2008]. On the other hand, reconstruction methods have also been proposed [Eisenstein et al., 2007a] to account for this kind of non-linear distortion, recovering the true peak position, and have been proved to be successful [Eisenstein et al., 2007a; Huff et al., 2007; Seo et al., 2008; Noh et al., 2009; Mehta et al., 2011]

Silk damping: Dissipation of perturbations below a given Silk scale; it is due to photons randomly walking out of overdense regions

distortions from galaxy bias

Lastly, a further shift of the BAO peaks emerges as a consequence of the bias mechanism. Indeed, if we aim to obtain constraints on the shape of the matter power spectrum, we should keep in mind that objects like galaxies or Type Ia supernovae (proposed as a target to measure BAO by Zhan et al. [2008]) trace the underlying dark matter distribution in an incomplete, partially unknown way, quantified by the bias parameter b as shown in the equation

$$P_{obj}(k) = b^2(k, z) P_{CDM}(k), \tag{3.15}$$

with $P_{obj}(k)$ standing for the power spectrum of the considered class of objects, $P_{CDM}(k)$ for the dark matter one, and where it was pointed out that the bias parameter can in principle be both scale and redshift dependent [Coles, 1993; Weinberg, 1995; Fry, 1996; Smith et al., 2007]. Mehta et al. [2011] used numerical simulations to extensively analyze repercussions of galaxy bias on BAO measurements, combined with the reconstruction technique by Eisenstein et al. [2007a]. They find that such shifts on the final determination of the peak position should not be noticeable in current surveys, e. g. SDSS, BOSS, or the WiggleZ dark energy survey. Despite that, they claim it is not excluded that upcoming surveys like BigBOSS or Euclid could measure the BAO scale with a precision that could allow for a bias shift to be noticed.

what about gravitational lensing?

A weak lensing measurement of the matter power spectrum would be immune to bias mechanisms, as gravitational lensing traces the overall matter distribution, rather than only baryons. We will see in Chapter 4 that, while classical weak lensing cannot be a valuable candidate for BAO detection due to its wide line-of-sight weighting functions, three-dimensional weak lensing can, instead, prove to be able to resolve oscillatory features in $P(k)$ [Grassi and Schäfer, 2013].

4

BARYON ACOUSTIC OSCILLATIONS WITH 3D WEAK LENSING

This chapter reproduces the content of the paper "Detecting baryon acoustic oscillations by 3d weak lensing" [Grassi and Schäfer, 2013]. The original analysis we carried out and the results are presented in Section 4.4 and summarized in Section 4.5.

ABSTRACT

We investigate the possibility of detecting baryon acoustic oscillation features in the cosmic matter distribution by 3d weak lensing. Baryon oscillations are inaccessible even to weak lensing tomography because of wide line-of-sight weighting functions and require a specialized approach via 3d shear estimates. We quantify the uncertainty of estimating the matter spectrum amplitude at the baryon oscillations wave vectors by a Fisher-matrix approach with a fixed cosmology and show in this way that future weak lensing surveys such as Euclid and DES are able to pick up the first four or three wiggles, respectively, with Euclid overall giving a better precision in the measurement. We also provide a detailed investigation of the correlation existing between errors and of their scaling behavior with respect to survey parameters such as median redshift, error on redshift, error on the galaxy shape measurement, sky coverage, and finally with respect to the number of wiggles one is trying to determine.

4.1 INTRODUCTION

Baryon acoustic oscillation (BAO) features are modulations in the cosmic matter distribution on very large spatial scales of roughly $\sim 100\,\mathrm{Mpc}/h$ [for a review, see Bassett and Hlozek, 2010]. These BAOs are the imprint of oscillations of the photon-baryon fluid in the early universe on the matter density field driven by gravity and the equation of state providing a restoring force, and they are observable in two primary channels: through the observation of anisotropies in the cosmic microwave background (CMB) and through galaxy surveys. The most important features such as their spatial scales, their signature in the CMB, their statistical properties, and their dependence on cosmological parameters is very well understood analytically [Seljak and Zaldarriaga, 1996; Hu and Sugiyama, 1996; Montanari and Durrer, 2011; Sutherland, 2012].

Concerning the determination of cosmological parameters, it is a fortunate situation that they are observable at high redshifts through the primary CMB and at much lower redshifts in the galaxy distribution. Due to the fact that BAOs provide a standard yardstick at two different cosmological epochs, it is possible to constrain the density parameters of cosmic fluids and the possible time evolution of their equation of state parameters in a geometric way, breaking degeneracies that may arise if the equations of state of cosmological fluids are allowed to change with time.

CMB observations carried out by the Cosmic Background Explorer [COBE, Bennett et al., 1994; Wright et al., 1996] first revealed anisotropies in the CMB, but only the Wilkinson Microwave Anisotropy Probe [WMAP, Hinshaw et al., 2003, 2007; Nolta et al., 2009; Larson et al., 2011] had sufficient angular resolution such that the BAO scale of $\sim 100\,\mathrm{Mpc}/h$ could be resolved at a comoving distance of $\sim 10\,\mathrm{Gpc}/h$, revealing temperature modulations of the CMB of the order $\Delta T/T_{\mathrm{CMB}} \simeq 10^{-5}$ at an angular scale of roughly 2°, with subsequent higher harmonics. Likewise, galaxy surveys have now reached sufficient depth and solid angle that BAO features could be detected as modulations of the galaxy density of the order 10% in both radial and transverse directions. With the assumption of a galaxy biasing model, the longest wavelength BAO modes survive nonlinear structure formation to the present epoch [Meiksin et al., 1999] and will be targeted by future surveys for the precision determination of cosmological parameters [Dolney et al., 2006; Angulo et al., 2008; Labatie et al., 2012], in particular dark energy [Seo and Eisenstein, 2003; Eisenstein et al., 2007a]. Both avenues have contributed significantly to the estimation of cosmological parameters and to the selection of most plausible cosmological models.

Specifically, there are quite a number of detection reports with ongoing surveys, for instance with the Sloan Digital Sky Survey [SDSS, Eisenstein et al., 2005; Padmanabhan et al., 2007; Percival et al., 2007b, 2010; Kazin et al., 2010b; Padmanabhan et al., 2012; Mehta et al., 2012], the 2-Degree Field Galaxy Redshift Survey [2dFGRS, Percival et al., 2007a; Beutler et al., 2011], the WiggleZ-survey [Parkinson et al., 2012] and Lyman-α data [Busca et al., 2012] with subsequent determination of cosmological parameters which confirm spatial flatness and the low matter density found by CMB observations, if flatness is assumed prior to the analysis. Recent studies [Parejko et al., 2012; Zhao et al., 2012] were able to constrain neutrino masses. BAO modulations have been found as longitudinal as well as transverse modes in the galaxy density [Gaztañaga et al., 2009a; Kazin et al., 2010a; Gaztañaga et al., 2009b] and their issues of model selection and parameter estimation have been addressed thoroughly [Cabré and Gaztañaga, 2011].

motivation

The motivation for this paper is the fact that the detection of BAOs as a modulation feature in the galaxy field depends on the assumption of a biasing mechanism [Gaztañaga et al., 2009a; Desjacques et al., 2010] which relates the galaxy number density to the ambient density of dark matter is well as a control of redshift space distortions effects [Nishimichi et al., 2007; Taruya et al., 2009] and it would be desirable to measure the dark matter density directly. Weak lensing would be a prime candidate for such a measurement, but the wide line-of-sight weighting functions cause the weak lensing signal to depend rather on the integral of the spectrum of cold dark matter (CDM) than on individual, localized features, even in the case of tomographic lensing surveys [Hu, 1999]. This is the reason why investigate the sensitivity of 3d weak lensing [3dWL, Heavens, 2003] for constraining the dark matter spectrum on BAO scales: 3dWL provides a direct estimate of the 3-dimensional matter distribution and gives Gaussian errors on the amplitude of the CDM spectrum in wavelength bands from sparsely sampled data [Leonard et al., 2012]. In this way, we aim to quantify the statistical precision at which 3dWL constraints the CDM spectrum at the BAO wavelengths, and the statistical significance for inferring the presence of one or more wiggles from 3dWL data relative to the null-hypothesis of absent wiggles.

why using 3dWL?

After a short compilation of basic results concerning distances, structure growth, structure statistics, and conventional weak lensing in Section 4.2, we recapitulate the main results of 3dWL in Section 4.3 and motivate its usage in constraining BAO wiggles. Our statistical approach and the estimation of statistical errors on the BAO measurement is given in Section 4.4, followed by a discussion of our main results in Section 7.9.

The reference cosmological model used is a spatially flat wCDM cosmology with Gaussian adiabatic initial perturbations in the matter distribution. The specific parameter choices are $\Omega_m = 0.25$, $n_s = 1$, $\sigma_8 = 0.8$ and $H_0 = 100\,h\,\mathrm{km/s/Mpc}$, with $h = 0.72$. The dark energy equation of state is set to $w = -0.9$ and we assume the dark energy to be smooth. The baryon density $\Omega_b = 0.04$ is used for correcting the CDM shape parameter and for predicting BAO-wiggle amplitudes and wave-vectors.

4.2 COSMOLOGY AND STRUCTURE FORMATION

4.2.1 *Dark energy cosmologies*

In spatially flat dark energy cosmologies with the present matter density Ω_m, the Hubble function $aH(a) = da/dt$ is given by

$$\frac{H^2(a)}{H_0^2} = \frac{\Omega_m}{a^3} + (1-\Omega_m)\exp\left(3\int_a^1 d\ln a\,(1+w(a))\right), \tag{4.1}$$

with the dark energy equation of state $w(a)$. A constant value $w \equiv -1$ corresponds to the cosmological constant. The relation between comoving distance χ and scale factor a is given by

$$\chi = c\int_a^1 \frac{da}{a^2 H(a)}, \tag{4.2}$$

with the Hubble distance $\chi_H = c/H_0$ as the cosmological distance scale. Redshift z and comoving distance are related by $dz/d\chi = H(z)/c$.

4.2.2 *CDM power spectrum*

The linear CDM-density power spectrum $P(k)$ describes the fluctuation amplitude of the Gaussian homogeneous density field δ,

$$\langle\delta(\mathbf{k})\delta(\mathbf{k}')^*\rangle = (2\pi)^3\delta_D(\mathbf{k}-\mathbf{k}')P(k) \propto k^{n_s}T^2(k), \tag{4.3}$$

with the the spectral index n_s and the transfer function $T(k)$. The restoring force provided by the baryon-photon fluid in the early Universe generates a set of wiggles in the spectrum $P(k)$ and an overall suppression due to diffusion. Both effects are discussed in detail by Eisenstein and Hu [1998] and Eisenstein and Hu [1999] who also provide a fitting formula for $T(k)$ in terms of the density parameters Ω_m, Ω_b, and the Hubble parameter h.

The spectrum $P(k)$ is normalized in such a way that it exhibits the variance σ_8^2 on the scale $R = 8$ Mpc/h,

$$\sigma_R^2 = \int \frac{k^2 dk}{2\pi^2} P(k) W^2(kR) \tag{4.4}$$

with a Fourier transformed spherical top hat filter function, $W(x) = 3j_1(x)/x$, where $j_\ell(x)$ is the spherical Bessel function of the first kind of order ℓ [Abramowitz and Stegun, 1972].

4.2.3 *Structure growth*

The growth of density fluctuations in the cosmic matter distribution can be described as a self-gravitating hydrodynamical phenomenon, in the limit of Newtonian gravity. Homogeneous growth of the density field

$$\delta(\mathbf{x}, a) = D_+(a)\delta(\mathbf{x}, a = 1) \tag{4.5}$$

in the linear regime $|\delta| \ll 1$ is described by the growth function $D_+(a)$, which is the solution to the growth equation [Turner and White, 1997; Wang and Steinhardt, 1998; Linder and Jenkins, 2003],

$$\frac{d^2}{da^2}D_+(a) + \frac{1}{a}\left(3 + \frac{d\ln H}{d\ln a}\right)\frac{d}{da}D_+(a) = \frac{3}{2a^2}\Omega_m(a)D_+(a). \tag{4.6}$$

Nonlinear structure formation leads to a strongly enhanced structure growth on small scales, generates non-Gaussian features and, most importantly, wipes out BAO wiggles as features in the initial matter distribution. This can be understood in an intuitive way as corrections to the CDM spectrum in perturbation theory to order n assume the shape of integrals over polyspectra up to order $2n$ [which separate into a product of n spectra by application of the Wick's theorem, see the review by Bernardeau et al., 2002] and are therefore becoming insensitive to localized features that are not strongly influencing the normalization of $P(k)$ [Springel et al., 2005; Jeong and Komatsu, 2006; Pietroni, 2008; Matarrese and Pietroni, 2008; Crocce and Scoccimarro, 2008; Nishimichi et al., 2009; Jeong and Komatsu, 2009; Jürgens and Bartelmann, 2012; Anselmi and Pietroni, 2012]. Since nonlinear structure formation affects small scales first, we will target BAO wiggles with 3dWL beginning at the largest wavelength before proceeding to successively shorter wavelengths.

4.2.4 *Weak gravitational lensing*

The weak lensing convergence κ provides a weighted line-of-sight average of the matter density δ [for reviews, see Bartelmann and Schneider, 2001; Munshi et al., 2008; Hoekstra and Jain, 2008; Bartelmann, 2010c],

$$\kappa = \int_0^{\chi_H} d\chi\, W_\kappa(\chi)\delta, \tag{4.7}$$

with the weak lensing efficiency $W_\kappa(\chi)$ as the weighting function,

$$W_\kappa(\chi) = \frac{3\Omega_m}{2\chi_H^2}\frac{D_+}{a}G(\chi)\chi, \tag{4.8}$$

and the lensing efficiency weighted galaxy redshift distribution, rewritten in terms of comoving distance,

$$G(\chi) = \int_{\chi}^{\chi_H} d\chi' \, n(\chi') \left(1 - \frac{\chi'}{\chi}\right). \tag{4.9}$$

$n(z)$ denotes a common parametrization of the redshift distribution of the lensed background galaxy sample,

$$n(z) = n_0 \left(\frac{z}{z_0}\right)^2 \exp\left(-\left(\frac{z}{z_0}\right)^{\beta}\right) dz \quad \text{with} \quad \frac{1}{n_0} = \frac{z_0}{\beta}\Gamma\left(\frac{3}{\beta}\right), \tag{4.10}$$

which can be rewritten in terms of a distribution in comoving distance with the relation $n(\chi)d\chi = n(z)dz$ using $d\chi/dz = c/H(a)$. These expressions allow to carry out a Limber projection [Limber, 1954] of the weak lensing convergence, which yields the angular convergence spectrum $C_\kappa(\ell)$,

$$C_\kappa(\ell) = \int_0^{\chi_H} \frac{d\chi}{\chi^2} W_\kappa^2(\chi) P(k = \ell/\chi). \tag{4.11}$$

We will formulate our derivations in terms of the lensing convergence κ instead of the observable shear γ because it is a scalar quantity and possesses identical statistical properties. Equation 4.11 illustrates why line-of-sight averaged weak lensing spectra are ineffective in picking up BAO wiggles (and is almost a repetition of the previous argument why nonlinear structure formation destroys BAO features): They provide only an integrated measure of the CDM spectrum $P(k)$ weighted with wide weighting functions $W_\kappa(\chi)$ that is very insensitive to local features of the spectrum such as BAO wiggles. This argument holds even for advanced tomographic surveys [Hu, 1999; Takada and Jain, 2004] and motivates the need of a 3-dimensional mapping of the cosmic matter distribution. With reference to Gaztañaga et al. [2009b] and Kazin et al. [2010a], we would like to emphasize that weak lensing, due to its sensitivity to gravitational shear components perpendicular to the line of sight, will provide measurements of BAO wiggles in the transverse direction.

4.3 3D WEAK LENSING

no line-of-sight averaging in 3dWL

The method of 3dWL was introduced by Heavens [2003], who proposed to include distances of lensed galaxies estimated from their photometric redshifts to infer the 3-dimensional *unprojected* tidal shear, i.e. the second derivatives of the gravitational potential perpendicular to the line-of-sight from distortions in the galaxies' ellipticity. Therefore, this approach differs from estimations of the angular line-of-sight averaged spectrum $C_\kappa(\ell)$ or corresponding tomographic spectra $C_\kappa^{ij}(\ell)$ in the important respect that the statistics of the full 3-dimensional matter distribution is inferred without any averaging of shears with the line-of-sight galaxy distribution, which has been performed in Equation 4.9. As such, 3dWL is particularly suited for the problem at hand, namely to provide a precise estimate of the amplitude of the dark matter power spectrum at the BAO wavelengths. Additionally, Heavens [2003] showed that if 3dWL is used for constraining $P(k)$ at a fixed cosmology, the smallest errors are expected in the BAO regime of the CDM spectrum.

In this section, we recapitulate the main results of 3dWL in terms of the weak lensing convergence in the Fourier-convention we prefer to work with; please also refer to Castro et al. [2005], Massey et al. [2007], Heavens et al. [2006], Kitching et al. [2008a] for a detailed description of the theory, to Munshi et al. [2011] for higher-order statistics through 3dWL and to Ayaita et al. [2012] for details of our numerical implementation. We assume spatial flatness and lensing in linearly evolving structures, which can be, in principle, relaxed from the 3dWL point of view [Pratten and Munshi, 2013]. The impact of systematic errors is nicely investigated by Kitching et al. [2008b], and for an application to observational data we refer the reader to Kitching et al. [2007].

The most natural choice for carrying out a Fourier transform in spherical coordinates is a combination of spherical harmonics for the angular and spherical Bessel functions for the radial dependence. We can therefore write the transformation for the convergence κ as

convergence transformation

$$\kappa_{\ell m}(k) \equiv \sqrt{\frac{2}{\pi}} \int \chi^2 d\chi \, d\Omega \, \kappa(\chi, \boldsymbol{\theta}) \, j_\ell(k\chi) Y^*_{\ell m}(\boldsymbol{\theta}), \qquad (4.12)$$

[see Ballinger et al., 1995; Heavens and Taylor, 1995], where j_ℓ and $Y_{\ell m}$ are, respectively, a spherical Bessel function of the first kind and a spherical harmonic, and $\boldsymbol{\theta} \equiv (\theta, \varphi)$. There exist algorithms for fast computation of $\kappa_{\ell m}(k)$ [Percival et al., 2004; Rassat and Refregier, 2012; Lanusse et al., 2012; Leistedt et al., 2012]. Such a transformation is particularly convenient as the combination of j_ℓ and $Y_{\ell m}$ is an eigenfunction of the Laplacian in spherical coordinates, leading to a quite simple relationship between the coefficients of the density field $\delta_{\ell m}(k)$ and the lensing convergence $\kappa_{\ell m}(k)$, as the observable:

$$\kappa_{\ell m}(k) = \frac{3\Omega_m}{2\chi_H^2} \frac{\ell(\ell+1)}{2} \frac{\eta_\ell(k, k')}{(k')^2} \delta_{\ell m}(k'), \qquad (4.13)$$

with the lensing-induced mode coupling $\eta_\ell(k, k')$

mode coupling induced by lensing

$$\eta_\ell(k, k') = \frac{4}{\pi} \int_0^\infty \chi'^2 d\chi' \int_0^{\chi'} d\chi \, \frac{\chi' - \chi}{\chi\chi'} \frac{D_+}{a} \, j_\ell(k\chi') j_\ell(k'\chi), \qquad (4.14)$$

with implicit assumption of the Einstein summation convention

$$X(k, k') \, Y(k', k'') \equiv \int_0^\infty k'^2 dk' \, X(k, k') \, Y(k', k''). \qquad (4.15)$$

It is then possible to construct an estimator for $\kappa_{\ell m}(k)$ by including the uncertainty of the galaxy distance estimates coming from errors in the measurements of redshift. If we denote by χ the true radial coordinate of a galaxy, and by χ' the one inferred by its observed redshift $z' = z(\chi')$, then they will be related by the probability $p(\chi'|\chi)$, which we assume to be Gaussian for simplicity:

$$p(\chi'|\chi)d\chi = \frac{1}{\sqrt{2\pi\sigma_z^2}} \exp\left[-\frac{(z(\chi)-z(\chi'))^2}{2\sigma_z^2}\right] dz', \tag{4.16}$$

where σ_z is the width of the distribution and is assumed to be constant throughout the entire galaxy sample. Furthermore, galaxies receive a statistical weight according to their distribution in distance $n(\chi)d\chi$. Following the derivation in Heavens [2003], we define the two additional matrices

mode coupling induced by redshift errors and galaxy distribution

$$Z_\ell(k,k') = \frac{2}{\pi}\int \chi'^2 d\chi' \int d\chi\, p(\chi'|\chi)\, j_\ell(k'\chi) j_\ell(k\chi'), \tag{4.17}$$

$$M_\ell(k,k') = \frac{2}{\pi}\int \chi^2 d\chi\, n(\chi)\, j_\ell(k\chi) j_\ell(k'\chi), \tag{4.18}$$

where $n(\chi)$ is the number density of galaxies, as defined in Equation 4.10. These matrices describe the correlations in spherical Fourier modes generated by the measurement process: While $\eta_\ell(k,k')$ describes mode couplings due to weak lensing, $Z_\ell(k,k')$ and $M_\ell(k,k')$ define, respectively, the contributions in the mode couplings coming from redshift errors and from the galaxy distribution along the radial coordinate χ.

full sky limit

We restrict ourselves to observations of the entire sky. In this case, the expression for the estimator $\bar{\kappa}_{\ell m}$ of the convergence is then expected to be

$$\bar{\kappa}_{\ell m}(k) = \frac{3\Omega_m}{2\chi_H^2} \frac{\ell(\ell+1)}{2} \frac{B_\ell(k,k'')}{(k'')^2} \delta_{\ell m}(k''). \tag{4.19}$$

mode-coupling matrix

where the mode-coupling matrix $B_\ell(k,k')$ describes two integrations over k_1 and k_2:

$$B_\ell(k,k'') = Z_\ell(k,k_1) M_\ell(k_1,k_2) \eta_\ell(k_2,k''). \tag{4.20}$$

convergence 3dWL covariance

Since the average values of a field like $\kappa_{\ell m}(k)$ are zero for all-sky surveys, we can only infer information about any parameter the field may depend on by means of its covariance,

$$\langle \bar{\kappa}_{\ell m}(k)\, \bar{\kappa}^*_{\ell m}(k') \rangle = S_{\kappa,\ell}(k,k') + N_{\kappa,\ell}(k,k') \equiv C_{\kappa,\ell}(k,k') \tag{4.21}$$

which consists of a signal term $S_{\kappa,\ell}(k,k')$ and a noise term $N_{\kappa,\ell}(k,k')$. The signal term $S_{\kappa,\ell}$ can be calculated directly from Equation 4.19:

$$S_{\kappa,\ell}(k,k') = \left(\frac{3\Omega_m}{2\chi_H^2}\right)^2 \left[\frac{\ell(\ell+1)}{2}\right]^2 \frac{B_\ell(k,k'')}{(k'')^2} \frac{B_\ell(k',k'')}{(k'')^2} P_\delta(k''), \tag{4.22}$$

with the abbreviations

$$\begin{aligned} B_\ell(k,k'') &= Z_\ell(k,k_1)\, M_\ell(k_1,k_2)\, \eta_\ell(k_2,k'') && (4.23) \\ B_\ell(k',k'') &= Z_\ell(k',k_3)\, M_\ell(k_3,k_4)\, \eta_\ell(k_4,k'') && (4.24) \end{aligned}$$

with implicit integration over k_1, k_2 and k_3, k_4. The corresponding noise part $N_{\kappa,\ell}$ is given by

$$N_{\kappa,\ell}(k,k') = \frac{\sigma_\epsilon^2}{4} M_\ell(k,k'), \qquad (4.25)$$

which is proportional to the shape noise σ_ϵ^2, namely the variance of the galaxy ellipticity distribution. It is important to notice that $N_{\kappa,\ell}$ is independent of cosmology or variations in the CDM spectrum $P(k)$. Intrinsic ellipticity correlations were neglected, which would greatly complicate the 3dWL description.

4.4 DETECTING BAO WIGGLES

4.4.1 *Construction of the Fisher matrix*

Fisher matrix definition

We choose a Fisher matrix approach to determine how precisely 3dWL can constrain baryon acoustic oscillations in the matter power spectrum $P(k)$. The Fisher matrix is a square matrix whose elements are defined as the expectation values of the second derivative of the logarithmic likelihood with respect to the fiducial parameters θ_α and θ_β:

$$F_{\alpha\beta} = -\left\langle \frac{\partial^2 \ln \mathcal{L}}{\partial\theta_\alpha \partial\theta_\beta} \right\rangle . \qquad (4.26)$$

As a general statement, if the likelihood $\mathcal{L}$ can be expressed as an N-dimensional Gaussian

$$\mathcal{L} = \frac{1}{\sqrt{(2\pi)^N \det(C)}} \exp\left(-\frac{1}{2}\vec{x}^T C^{-1} \vec{x}\right), \qquad (4.27)$$

where $\vec{x}$ is a generic data vector and C is the corresponding covariance, we can then write

$$F_{\alpha\beta} = \frac{1}{2} \mathrm{tr}\left[(C^{-1}\,\partial_\alpha C) \times (C^{-1}\,\partial_\beta C)\right], \qquad (4.28)$$

or, equivalently,

$$F_{\alpha\beta} = \frac{1}{2} \mathrm{tr}\left[\partial_\alpha \ln C \times \partial_\beta \ln C\right], \qquad (4.29)$$

where ∂_α and ∂_β stand for the derivatives with respect to the parameters θ_α and θ_β. Given a particular experimental framework, the Fisher matrix specifies what are the best errors to expect for the inferred parameters θ_α via the Cramér-Rao relation.

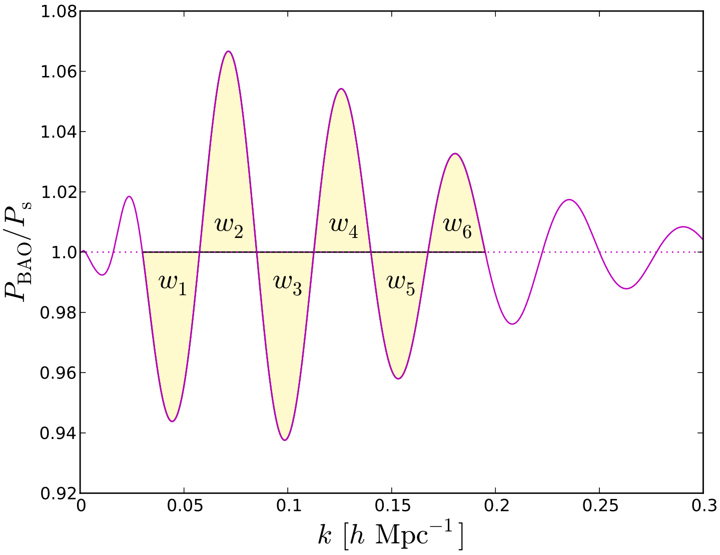

Figure 4.1: Ratio between the power spectrum with baryon acoustic oscillations $P(k)$ and the smooth power spectrum $P_s(k)$. The largest wiggles in amplitude have been highlighted and labeled as $w_\alpha, \alpha = 1, ..., 6$. These are the wiggles used to parametrize the power spectrum in our Fisher matrix approach.

It can be proved that, since ℓ-measurements are independent in the case of full-sky coverage, we can reformulate Equation 4.28: We consider our estimator to be $\bar{\kappa}_{\ell m}(k)$ and its covariance as defined in Equation 4.21, and find

$$F_{\alpha\beta} = \frac{f_{\rm sky}}{2} \sum_{\ell=\ell_{\rm min}}^{\ell_{\rm max}} (2\ell+1)\, {\rm tr}\left[({C_{\kappa,\ell}}^{-1}\, \partial_\alpha C_{\kappa,\ell}) \times ({C_{\kappa,\ell}}^{-1}\, \partial_\beta C_{\kappa,\ell})\right] . \tag{4.30}$$

our parametrization of the spectrum

In our specific case, we consider the power spectrum as parametrized not by usual cosmological parameters, such as Ω_m or σ_8, but rather by its own wiggles amplitudes, namely by the values assumed by $P(k)$ in a range of k where the wiggles w_α are located. In Figure 4.1 we plot the wiggle-only power spectrum, i.e. the ratio between the power spectrum with baryon acoustic oscillations $P(k)$ and an equivalent, smoothed out spectrum that has the same shape as $P(k)$ but shows no oscillating feature, $P_s(k)$. We highlight the wiggles that have been used to parametrize $P(k)$, $w_\alpha, \alpha = 1, ..., 6$. By calculating the derivative $\partial_\alpha C$ of the covariance with respect to a variation of the amplitude of a maximum number of wiggles n_w, we can build up (Equation 4.28) a Fisher matrix $F_{\alpha\beta}$, where $\alpha, \beta = 1, ..., n_w$. Such a matrix carries information about the best errors to expect on the detection of each wiggle w_α, $\alpha = 1, ..., n_w$, and the cross-correlations

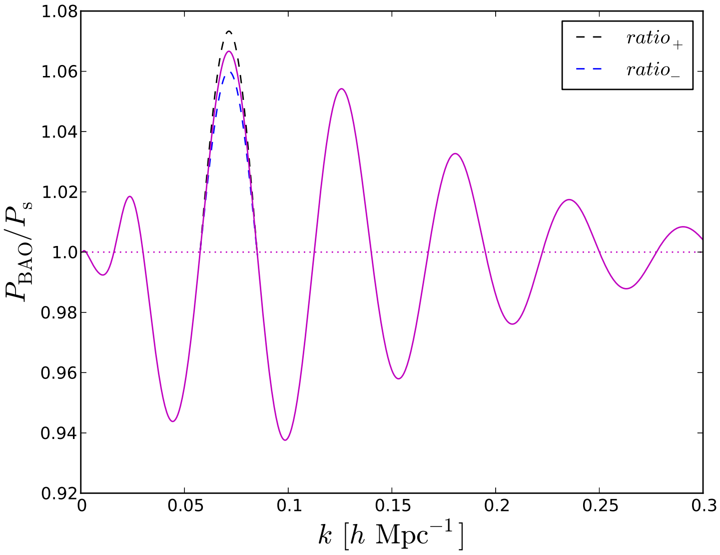

Figure 4.2: The ratio between $P(k)$ and $P_s(k)$. The figure shows a pictorial representation of the variation of the amplitude of one wiggle when calculating the derivative of the covariance matrix, $\partial_{\alpha=2}C_\ell$.

between inferred wiggle amplitudes. Given our aim, what we are actually performing in the calculation of $\partial_\alpha C$ is a functional derivative, also known as Fréchet derivative. In fact, we can imagine the power spectrum as depending on features, i.e. the wiggles in Figure 4.1. Each one of them can be approximated to a sin-like function defined in a range of k as wide as $\lambda/2$, where λ is the wavelength of the function itself. The covariance derivative is numerically estimated for one wiggle at a time as a finite difference:

covariance derivative

$$\partial_\alpha C_{\kappa,\ell} = \frac{C^+_{\kappa,\ell,\alpha} - C^-_{\kappa,\ell,\alpha}}{2\epsilon}, \tag{4.31}$$

where $C^\pm_{\kappa,\ell,\alpha}$ are the covariance matrices calculated using the power spectra $P^\pm_\alpha(k)$ and ϵ is an arbitrarily small number. The spectra $P^\pm_\alpha(k)$ are equivalent to the original $P(k)$ for all k of the domain, exception made for the wave numbers belonging to the interval I_α that corresponds to wiggle w_α. In this interval $P^\pm_\alpha(k)$ is then

$$P^\pm_\alpha(k) = P(k) \pm \epsilon P(k). \tag{4.32}$$

We would like to point out that, since what we are actually performing by means of the spectrum variation in Equation 4.32 is in a way a logarithmic derivative of C_ℓ, the denominator in Equation 4.31 lacks a factor $P(k)$ and is therefore just two times the fraction of the spectrum used in the variation. In Figure 4.2 we show a representation of an example of the variation performed in the calculation of the derivative

	z_{med}	$\bar{n}$	f_{sky}	σ_z	σ_ϵ
Euclid	0.9	30	0.5	0.1	0.3
DES	0.7	10	0.1	0.12	0.3
DEEP	1.5	40	0.1	0.05	0.3

Table 4.1: Basic survey characteristics used for the Fisher-analysis: median redshift z_{med} of the galaxy sample, galaxy density per squared arcminute $\bar{n}$, sky coverage fraction f_{sky}, redshift error σ_z and shape measurement error σ_ϵ of the surveys Euclid, DES and a hypothetical deep-reaching survey labeled DEEP.

of the covariance matrix, $\partial_\alpha C$; in this case the second wiggle, w_2, has been considered.

It is worth noticing that the Fisher-matrix approach for inferring the error σ_α on the dark matter spectrum $P(k_\alpha)$ (where k_α are simply the $k \in I_\alpha$, for brevity) as a Gaussian standard deviation is perfectly justified because of the linearity of the lensing observable and the linearity of the random field, so we do not need to use Monte-Carlo sampling for evaluating the likelihood $\mathcal{L}(P(k_\alpha))$ and to measure its widths σ_α from Monte-Carlo samples of the likelihood.

noise sources:
- shape noise
- redshift error

assumptions and simplifications

surveys

As noise sources for the inference of $P(k_\alpha)$, we consider a Gaussian shape measurement error σ_ϵ for the galaxy ellipticities, which are assumed to be intrinsically uncorrelated, and a Gaussian error σ_z for the redshift determination uncertainty. Likewise, we work in the approximation of neglecting all geodesic effects [Seitz and Schneider, 1994; Seitz et al., 1994] like deviations form the Born approximation, lens-lens couplings [Shapiro and Cooray, 2006; Krause and Hirata, 2010], source clustering [Schneider et al., 2002], source-lens correlations [Hamana et al., 2002], and deviations from Newtonian gravity [Acquaviva et al., 2004]. While performing the necessary variations for computing the Fisher matrix, we keep all other cosmological parameters fixed and calculate everything using an ℓ-range between $\ell_{\mathrm{min}} = 2$ and $\ell_{\mathrm{max}} = 100$ (please see the next section for a justification of this choice). As surveys, we consider the cases of Euclid, DES, and a hypothetical deep-reaching galaxy survey we refer to by the name DEEP. The respective survey properties are summarized in Table 4.1. For the calculation of the covariance matrices, we adopted the numerical implementation by Ayaita et al. [2012], also described in Appendix A.

4.4.2 *Statistical errors*

Cramér-Rao error

The error σ_α for inferring the amplitude of the CDM spectrum $P(k_\alpha)$

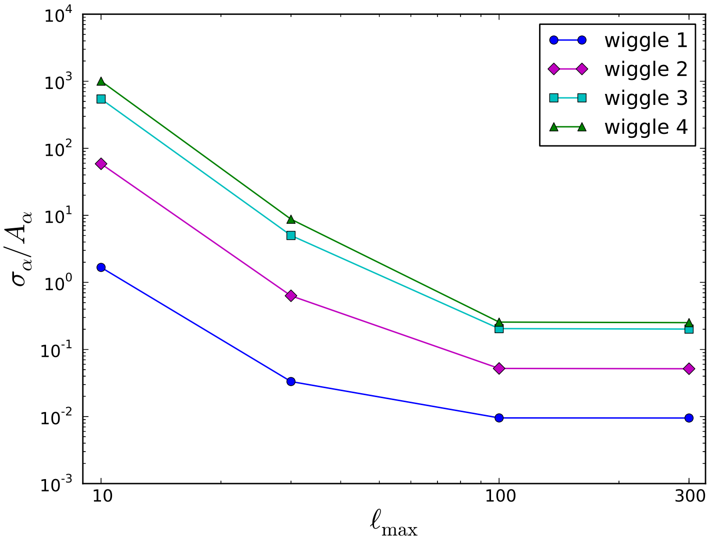

Figure 4.3: The marginalized errors on the first four wiggles, normalized with respect to their amplitude, as the maximum ℓ used for the calculation of the Fisher matrix increases. It shows that choosing $\ell_{\max} > 100$ brings no particular advantage in the precision of the wiggles measurement. In the calculation of the errors we considered the power spectrum as parametrized by the first 4 wiggles.

at wiggle positions k_α is given by the Cramér-Rao relation,

$$\sigma_\alpha^2 = (F^{-1})_{\alpha\alpha}, \tag{4.33}$$

and

$$\sigma_\alpha^2 = 1/F_{\alpha\alpha}, \tag{4.34}$$

for marginalized and conditional likelihoods, respectively.

sensitivity to survey parameters

Before carrying out our analysis for surveys like Euclid, DES, and DEEP, we implement some tests in order to determine the optimal value for the maximum number of modes to be used in the calculation of the Fisher matrix, $\ell_{\max}$. Besides, we tried to find out how and by how much are the errors sensitive to some of the usual survey parameters, such as

1. the shape noise σ_ϵ;
2. the error σ_z in the measurement of redshift;
3. the median redshift z_{med};
4. the fraction of sky coverage f_{sky}.

Throughout these tests, when not stated otherwise, we make use of a default set of survey parameters such that $\sigma_z = 0.02$, $\sigma_\epsilon = 0.3$,

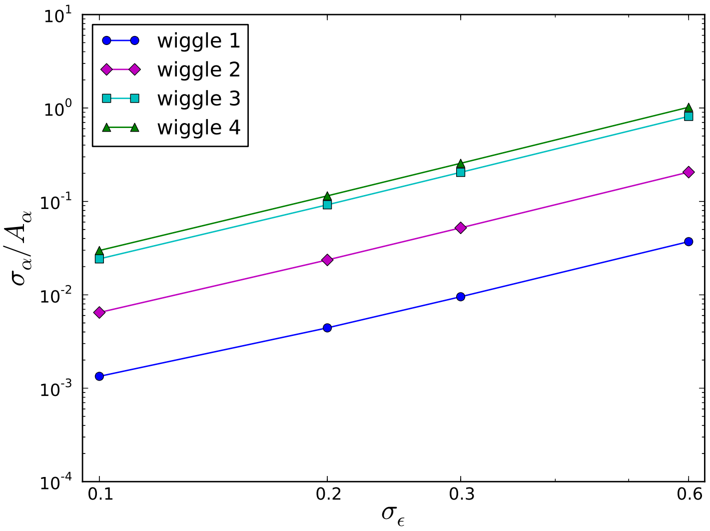

Figure 4.4: The relative marginalized error for the first 4 wiggles, as the shape noise σ_ϵ varies. Again, we assumed $\sigma_z = 0.02$, $\sigma_\epsilon = 0.3$, $z_{\text{med}} = 0.9$, $f_{\text{sky}} = 0.4$ and $\bar{n} = 20$. As we expected, larger values of σ_ϵ bring along larger errors on the detection of the wiggles.

$z_{\text{med}} = 0.9$, $f_{\text{sky}} = 0.4$ and $\bar{n} = 20$. Additionally, we assumed we want to constrain simultaneously the first four wiggles (see Figure 4.1).

finding the optimal ℓ_{max}

We start our investigation by determining the errors σ_α, $\alpha = 1, 2, 3, 4$, as the maximum number of modes ℓ_{max} in the summation in Equation 4.30 increases. Please refer to Figure 4.3 for a plot of the behavior of σ_α normalized to the oscillation amplitude A_α, where A_α is defined as the maximum value of $|P(k) - P_s(k)|$ for each wiggle. In particular, we considered $\ell_{\text{max}} = 10, 30, 100, 300$, and observe that, after $\ell_{\text{max}} = 100$, there is practically no gain in the precision with which the first 4 wiggles would be constrained in a 3dWL approach. Therefore, we decide to stick to a maximum number of modes of 100 for all the subsequent calculations. This is a fair approximation also from a theoretical point of view: In fact, extending too much the ℓ interval for the $F_{\alpha\beta}$ summation could make us fall out of the linear regime; in addition, the assumption of a Gaussian shape for the likelihood $\mathcal{L}$ could not to be anymore reasonable in such a multipole range [Heavens, 2003].

shape-noise

In Figure 4.4, we show what happens as soon as we keep all the survey parameters fixed and vary the shape noise σ_ϵ. As one can expect, larger values of σ_ϵ lead to larger σ_α, therefore to a greater uncertainty in the detection of the wiggles. Moreover, the rate at which σ_α grows with the shape noise seems to be of the type of a power law, and seems independent of the wiggle considered, at least for the wiggles sample we evaluated. The situation turns out to be similar when the error in the determination of redshift σ_z is considered, in Figure 4.5:

redshift error

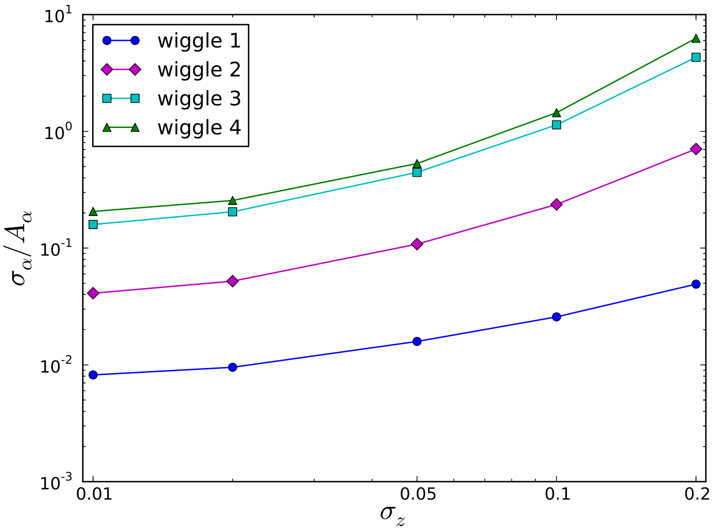

Figure 4.5: The relative marginalized error for the first 4 wiggles as a function of the error in the measurement of the photometric redshift, σ_z. The sensitivity of the errors on the value of σ_z is not as steep as it is for the shape noise σ_ϵ. In addition, the increasing rate of σ_α seems to change as we consider higher order wiggles.

increasing σ_z still produces larger errors on all the wiggles under investigation, although here the relation is somewhat slower, especially as long as $\sigma_z \lesssim 0.1$; the relation also appears to be slightly dependent on the wiggle, becoming steeper as higher order oscillations are taken. In fact, by incrementing the error on redshift from 0.01 to 0.1, we get an error larger only by a factor of ~ 2 on the first wiggle and by a factor of ~ 8 on the second. Additionally, the correspondence between σ_α and the median redshift of the survey (Figure 4.6) seems again like a power law that gives larger errors for an increasing z_{med}, and is independent of the wiggle. Qualitatively, this trend makes sense in light of the fact that, as we increase the median redshift, we keep fixed all other survey parameters such as, for example, the galaxy density per squared arcminute $\bar{n}$. By doing so, we consider surveys where a number $\bar{n}$ of galaxies is distributed over a deeper cone, meaning that we are actually sampling the 3D convergence field in a more diluted way, and therefore inheriting a larger noise. Naturally, varying the sky covarage propagates to the errors $\sigma_\alpha \propto 1/\sqrt{f_{\text{sky}}}$.

median redshift

sky coverage

4.4.3 *Detectability of BAO wiggles*

In this section, we would like to present the results obtained when estimating the best errors to expect on BAO wiggles for the surveys Euclid, DES, and DEEP (please see Table 4.1 for specifications).

We started our analysis by calculating both marginalized ($\sigma_\alpha =$

marginalized and conditional errors

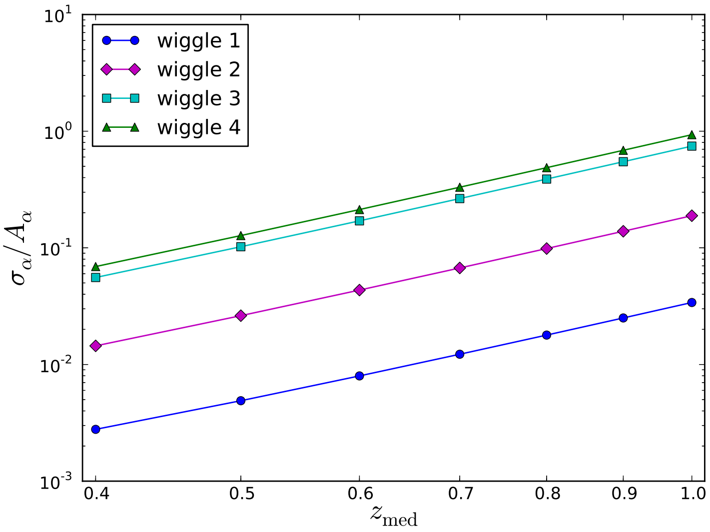

Figure 4.6: Relative marginalized errors on the first 4 wiggles when the median redshift $z_{\rm med}$ of the survey increases. Since all other parameters are kept fixed, especially the mean galaxy density per squared arcminute, $\bar{n}$, increasing $z_{\rm med}$ is equivalent to having more and more diluted surveys, where the same amount of galaxies is distributed along a deeper survey cone.

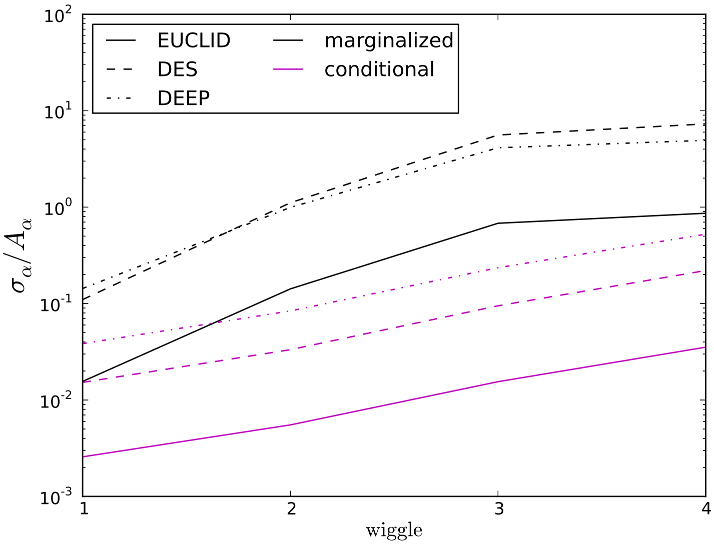

Figure 4.7: Conditional (magenta lines) and marginalized relative errors (black lines) for the three surveys under investigations Euclid (solid line), DES (dashed line) and DEEP (dash-dot line) as a function of the wiggles, when the first 4 oscillations are simultaneously constrained.

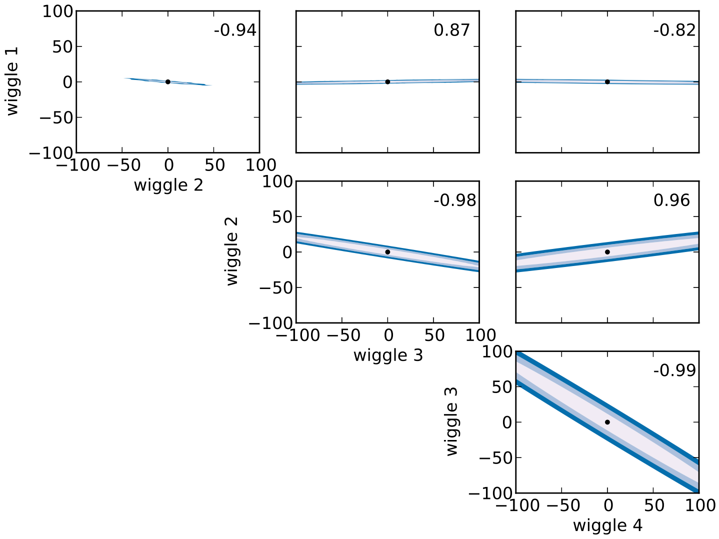

Figure 4.8: Confidence ellipses for the first four wiggles in a Euclid-like survey, showing that the wiggles are indeed highly correlated. In fact, taking, for example, two consecutive wiggles, such as w_2 and w_3, we see that by increasing the amplitude of $P(k)$ at the position of wiggle 2, we must then have the amplitude at w_3 decreased in order to remain in the confidence region. The x- and y-axes show the variation of the wiggle in terms of percentage of its amplitude A_α, the three contours areas correspond to $1-2-3\sigma$, and every panel shows the correlation coefficient in the upper-right corner.

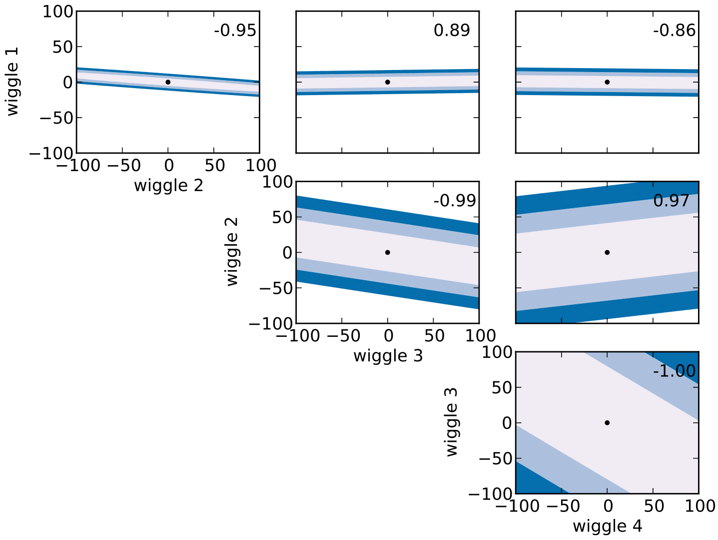

Figure 4.9: Fisher confidence ellipses for DES, when one tries to simultaneously constrain the first four wiggles. Again, contours areas correspond to $1-2-3\sigma$ and the number in every panel is the correlation coefficient; the axes represent variation of wiggles in terms of their amplitude fraction. Also in this case we can observe correlation between the amplitudes of $P(k)$ at different wiggles positions.

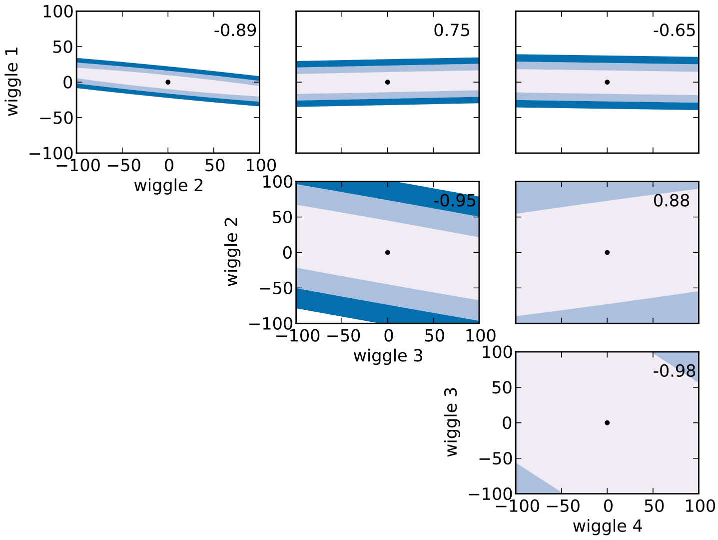

Figure 4.10: Confidence ellipses for the DEEP survey, with the variation of the oscillations in terms of the wiggle amplitude. Again, we assumed we wanted to constrain jointly the first four wiggles, contour areas stand for $1-2-3\sigma$ and the correlation coefficient can be read in the panels.

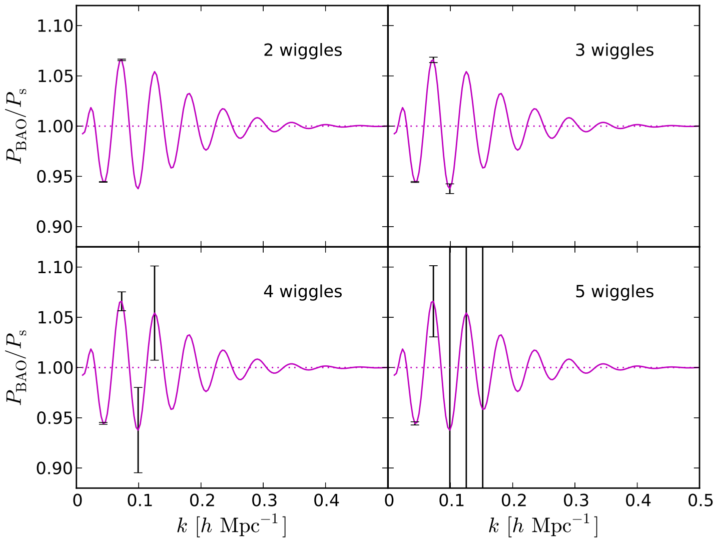

Figure 4.11: The bars show the marginalized errors in the detection of the wiggles, normalized with respect to $P_s(k)$, when the first 2 (upper left panel), 3 (upper right panel), 4 (bottom left panel), 5 (bottom right panel) wiggles are used to parametrize the power spectrum. Here, we considered a Euclid-like survey with $\sigma_z = 0.1$, $\sigma_\epsilon = 0.3$, $z_{\rm med} = 0.9$, $f_{\rm sky} = 0.5$ and $\bar{n} = 30$.

$\sqrt{(F^{-1})_{\alpha\alpha}}$) and conditional errors ($\sigma_\alpha = 1/\sqrt{F_{\alpha\alpha}}$) relative to the wiggle amplitude. These errors were computed for the three types of surveys, considering the first four oscillations, as shown in Figure 4.7. As we could expect, marginalized errors are always larger than the correspondent conditional ones, namely the σ_α on each wiggle when we assume to know precisely all the other wiggle amplitudes.

confidence ellipses

We continue the investigation considering the confidence ellipses calculated from the corresponding Fisher matrices obtained for the three surveys. We assume we are aiming to jointly constrain the first four wiggles and plot the results in Figure 4.8, Figure 4.9, and Figure 4.10 for, respectively, Euclid, DES, and DEEP. The sizes of the ellipses, whose contours stand for $1-2-3\sigma$, already tell us that, among the ones evaluated, Euclid will probably be the survey with largest constraining power on the BAO wiggles. It is of particular interest noticing the orientation of the ellipses, or their correlation coefficients (upper-right corner in every panel), that tell us something about the interdepence between different wiggles: In fact, neighboring wiggles are anti-correlated , i.e. increasing the amplitude of the power spectrum in correspondence to one oscillation would cause the $P(k)$ at the position of the adjacent wiggle to take smaller values in order to stay among the confidence region, and vice versa, whereas the opposite holds for alternated wiggles.

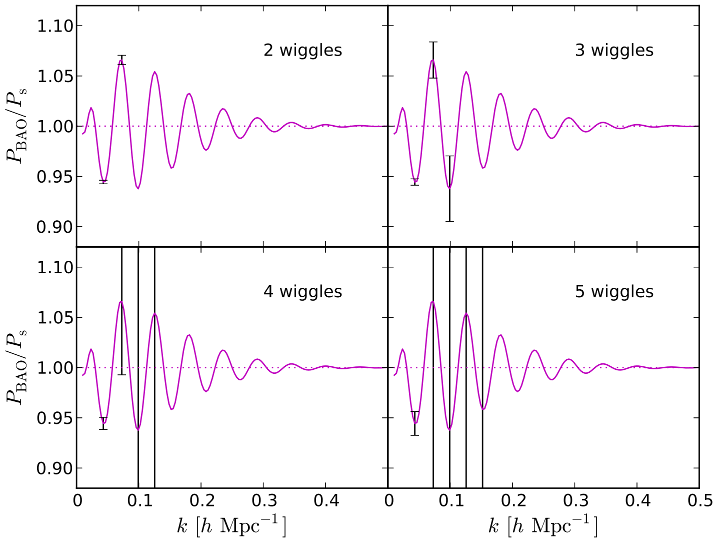

Figure 4.12: Marginalized errors on the detection of BAO wiggles when one tries to detect the first 2 (upper left panel), 3 (upper right panel), 4 (bottom left panel), 5 (bottom right panel) wiggles at the same time, for a DES-like survey ($\sigma_z = 0.12$, $\sigma_\epsilon = 0.3$, $z_{med} = 1.5$, $f_{sky} = 0.12$ and $\bar{n} = 10$). Again, we considered the relative marginalized errors, dividing by $P_s(k)$.

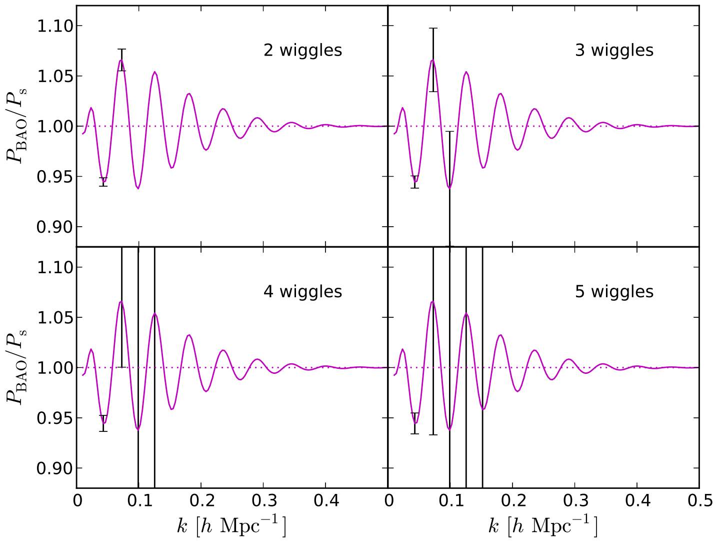

Figure 4.13: The marginalized errors on the detection of the wiggles in the power spectrum, relative to $P_s(k)$, for the hypothetical survey DEEP, characterized by the parameters $\sigma_z = 0.05$, $\sigma_\epsilon = 0.3$, $z_{med} = 1.5$, $f_{sky} = 0.1$ and $\bar{n} = 40$.

In order to better understand whether the constraining power of the three surveys will allow us to detect any oscillatory feature in the CDM power spectrum, we plot the σ_α obtained from the Cramér-Rao relation in Equation 4.33 as error bars in the usual wiggle-only power spectrum for DEEP (Figure 4.13), DES (Figure 4.12), and Euclid (Figure 4.11). Since what is shown is a ratio between $P(k)$ and a smooth spectrum, the σ_α have of course also been normalized with respect to $P_s(k)$. The four different panels show how the errors change when we try to jointly constrain the first 2, 3, 4, or 5 wiggles with a 3dWL approach.

What these and the following plots show, first of all, is an expected feature: As we increment the number of wiggles we expect to simultaneously examine, the precision with which the amplitudes $P(k_\alpha)$ would be measured gets poorer and poorer for all the oscillations. Our purpose would then be to evaluate how many BAO wiggles one is allowed to constrain before the errors on them become too large. It can be seen that all three surveys would allow for quite good constraints on the first 2 wiggles. The hypothetical survey DEEP already shows error bars of the order of the wiggle amplitude A_α when the first 3 wiggles are considered, and the errors become much larger than A_α ($\alpha > 1$) as soon as one tries to detect 4 or more wiggles (Figure 4.13). On the other hand, DES and Euclid give a better performance, allowing for, respectively, the first 3 and 4 wiggles to be simultaneously constrained, with Euclid giving smaller errors overall (Figure 4.11).

A better comparison between the three surveys can be carried out analyzing Figure 4.14 and Figure 4.15, where we plotted relative errors σ_α/A_α as functions of the maximum number of wiggles we want to jointly constrain, n_w, and we collate results coming from, respectively, DEEP and Euclid, and DES and Euclid. It becomes straightforward that a DEEP-like survey cannot compete against Euclid: The relative errors coming from DEEP are always larger than the latter's, independently of the maximum number of wiggles to be constrained, and remain safely under the unity only for the first 2 wiggles.

The situation is better for DES, that seems to be at least able to detect the first three wiggles. However, DES gives a worse performance than Euclid, with errors larger of a factor ~ 6.

Concluding, Euclid seems to grant the best results, allowing for the simultaneous detection of up to 4 wiggles with expected errors that are smaller than the ones predicted for both DES and, of course, DEEP, and that range between $\sim 1\%$ and $\sim 10\%$ (with respect to the wiggle amplitudes) for the first harmonics.

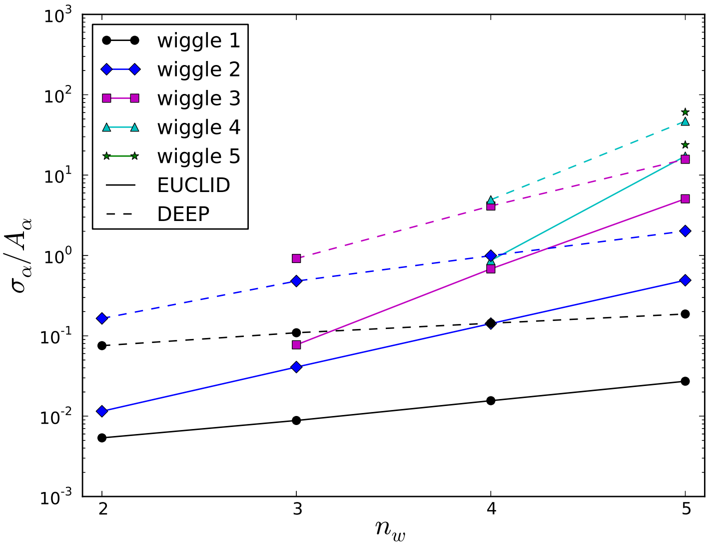

Figure 4.14: Relative marginalized errors as a function of n_w for a Euclid-like survey (solid lines) and a DEEP-like survey (dashed lines). The relative σ_α for a DEEP survey appear to be always larger than the ones obtained from Euclid, independently of the maximum number of wiggles n_w we want to constrain.

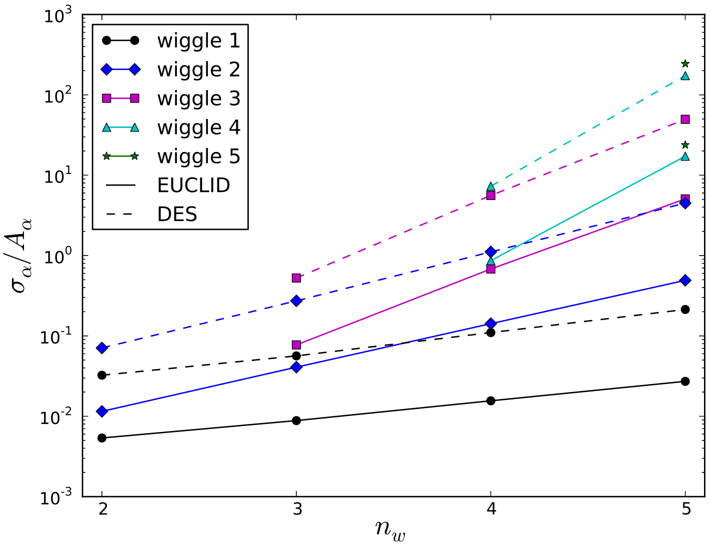

Figure 4.15: Relative marginalized errors (with respect to the wiggles amplitude) as a function of the maximum number of wiggles that we try to simultaneously detect, n_w. Here, we show the results for a Euclid-like survey (solid lines) and a DES-like survey (dashed lines). Different colors and point types correspond to the different wiggles on which the error σ_α is calculated. The relative errors coming from a DES-like survey turn out to be larger than Euclid's over all the n_w interval, nevertheless still allowing DES to detect the first three wiggles simultaneously.

4.5 SUMMARY AND CONCLUSIONS

Subject of this paper has been a statistical investigation on whether future weak lensing surveys are able to detect baryon acoustic oscillations in the cosmic matter distribution by application of the 3d weak lensing method. For a fixed *w*CDM cosmology, we have estimated the statistical precision σ_α on the amplitude of the CDM spectrum $P(k)$ at the BAO wiggle positions in a Fisher-matrix approach. Throughout, we worked under the assumption of Gaussian statistics, independent Fourier modes and in the limit of weak lensing. Noise sources were idealized and consisted in independent Gaussian-distributed shape-noise measurements for the lensed background galaxy sample, as well as a Gaussian error for the redshift determination. As surveys, we considered the cases of Euclid, DES and a hypothetical deep-reaching survey DEEP.

1. We have constructed the Fisher matrix considering our model as parametrized by the amplitudes of the CDM power spectrum at the baryon acoustic oscillations anticipated positions. In particular, we started taking the two BAO wiggles with largest amplitude and progressively increased the number of oscillations considered. Keeping the cosmology fixed to a standard *w*CDM parameter choice, we carried out variations of $P(k)$ that preserved its wiggle-shape in those wave number intervals; we then estimated the Fisher matrix accordingly, in order to quantify whether the statistical power of future weak lensing surveys suffices to place bounds on the amplitudes of the considered harmonics. By means of the Cramér-Rao relation, we calculated the best errors σ_α to expect for the amplitudes of $P(k)$ at wiggle positions.

2. The sensitivity of σ_α with respect to some typical survey-parameters was tested. In particular, we considered the shape noise σ_ϵ, the redshift error σ_z, the median redshift z_{med}, and the sky coverage f_{sky}. We found that, as expected, increasing the uncertainty in the estimate of either the redshift or the galaxy shapes brings a larger error in the inference of the presence of wiggles, and that the sensitivity of these errors on σ_z is less pronounced for small values of σ_z, although it grows as soon as we consider higher order wiggles or large σ_z. An increase of z_{med} leads as well to larger errors on the wiggles amplitudes, as one would expect from considering less and less populated surveys; for the same reason, a wider sky coverage, i.e. larger f_{sky}, yields to higher precision in constraining the wiggle amplitudes $\sigma_\alpha \propto 1/\sqrt{f_{\mathrm{sky}}}$.
   Overall, we may conclude that the volume of a survey seem to

be overcoming the importance of a high precision in the redshift measurement of galaxies, at least for $\sigma_z < 0.1 - 0.2$.

3. Finally, we evaluated the σ_α for the surveys under investigation and found that, among them, Euclid gave the best results, potentially allowing for the detection of up to the first four BAO wiggles with a good statistical confidence. Given our tests on the sensitivity of the errors on $P(k_\alpha)$ to certain survey parameters, we may conclude that Euclid's good performance is probably due to the volume of the survey in terms of total galaxy number and sky coverage, that seem to prevail over the negative effects brought by the error on redshift measurements, σ_z, larger than the ones predicted for the other two surveys.

Given these results, we conclude that measurements of BAO wiggles based on future weak lensing data are entirely possible, and avoid issues related to galaxy biasing and redshift-space distortions. We forecast a detection of the first four or three wiggles with Euclid and DES by applying 3dWL techniques. Future developments from our side include estimates of the precision that can be reached on inferring dark energy density and equation of state by including the estimate of the BAO scale at low redshifts probed by lensing to the estimates at intermediate redshift provided by galaxy surveys and those at high redshifts such as the CMB. Additionally, we are investigating the impact of systematical errors on the estimation process from 3dWL-data and biases in the estimation of BAO-wiggle amplitudes.

The next Part of this thesis will analyze another possible use of the weak lensing method: the detection of primordial non-Gaussianities in the density fluctuations distribution.

Part III

PROBING PRIMORDIAL NON-GAUSSIANITIES WITH WEAK LENSING

5

INFLATION AND PRIMORDIAL NON-GAUSSIANITIES

Inflation is probably among the most controversial topics in Cosmology. Inflation models theorize an accelerated expansion that happened in the very first moments after the big bang. Such an expansion could, in fact, solve some of the contradictions of the standard hot big bang model, and produce the distribution of density anisotropies we observe in the CMB, and from which the Milky Way originated.

Under the inflation paradigm, many models flourished, trying to explain in detail the mechanism behind the expansion, and what is responsible for it. Up to now, we still do not know if such an accelerated expansion really took place, and what kind of fields generated it. One way to help us discriminating among the wide range of candidate models, is measuring the amount of deviation from Gaussianity in the distribution of primordial density fluctuations: In fact, many inflationary models predict different degrees of non-Gaussianities, making them a valuable tool.

In the present Chapter, I will schematically introduce the main problems of the standard big bang model, and how the hypothesis of an accelerated expansion can solve some of them in an elegant an simple fashion (Section 5.1). In Section 5.2, I will address primordial non-Gaussianities in the density fluctuations: how they form and how they can be described by means of the local, equilateral, and orthogonal shapes.

When not stated otherwise, all the content of this Chapter is based on the reviews by Bartolo et al. [2004], Wang [2013], Chen [2010], and on Komatsu [2010], Liddle and Lyth [2000].

5.1 THE INFLATIONARY PARADIGM

5.1.1 *Standard model: successes and issues*

The standard hot big bang model arises as a natural consequence when the following assumptions are adopted:

1. gravity is described by the theory of general relativity, and laws of physics as we know them are also valid during the early Universe;

Cosmological Principle

2. the Universe is homogeneous and isotropic on large scales;
3. some initial conditions must hold, in particular:
   - the content of the Universe is initially in thermal equilibrium;
   - $\Omega_{\text{tot}}(t = 0)$, i. e. the total density parameter of the Universe, is very close to unity, meaning that the Universe is very close to perfect flatness at its early stages;
   - some kind of spectrum of initial fluctuations in the density distribution is provided.

standard model successes

Given these premises, one can construct a theory that easily (or *almost* easily)

1. explains the Universe's expansion,
2. predicts the observed light-element abundances,
3. gives a natural explanation for the isotropy of the cosmic microwave background,
4. provides a framework for a theory of structure formation, aiming to understand how the initial density fluctuations evolved and eventually generated collapsed objects such as galaxies, or the large scale structure.

standard model issues

Despite such important successes of the standard hot big bang model, there are still some issues that cannot find a solution in this system. For instance, the cosmological constant problem, that I will not address here (for a review on the topic see Sahni [2002], Martin [2012], or the broader Padmanabhan [2003]), the absence of evidence for topological defects such as magnetic monopoles [Preskill, 1979], our ignorance on what exactly constitutes dark matter (see for instance the reviews Einasto [2009], Silk [2013]), or the standard model's inability to explain the existence of primordial density fluctuations, that must be given as an initial condition. Other problems are the horizon and the flatness ones, briefly described below.

" *The horizon of many people is a circle with zero radius, which they call their point of view.*" A. Einstein

THE HORIZON PROBLEM The existence of a limiting velocity like c comes naturally with the presence of a particle horizon. The particle horizon defines, for every point in space, the radius of the sphere containing everything the point itself could have been in causal contact with. This means that from the moment of big bang to a generic moment t, information could travel only a finite distance. If we imagine information to be carried by photons with speed c, then this distance can be calculated from imposing a null geodesic

$$0 = ds^2 = c^2dt^2 + a^2dr^2, \tag{5.1}$$

hence yelding

$$r_H(t) = c\int_0^{a(t)} \frac{dt'}{a(t')}. \tag{5.2}$$

The problem arises as soon as we estimate the particle horizon at the time of recombination $r_H(t_{rec})$. In fact, it turns out that the portion of sky every point could have already been in causal contact with, at recombination, is roughly $1/100$ of our observable universe. This, of course, is in strong contradiction with CMB observations, clearly showing that at t_{rec} the Universe is already homogeneous and isotropic, at least if we leave aside fluctuations of the order of $\Delta T/T \sim 10^{-5}$. How can CMB spots separated by $r > r_H$ look like they had been casually connected?

THE FLATNESS PROBLEM As the Universe expands, its curvature evolves with time: the first Friedmann's equation (Equation 1.5) can be rewritten in terms of the total density parameter Ω_{tot}:

$$\left[\Omega_{tot}^{-1}(t) - 1\right] \rho(t)\, a^2(t) = -\frac{3Kc^2}{8\pi G}. \tag{5.3}$$

The quantities on the right hand side of the equation are clearly all constants, and, since $\rho(t)\, a^2(t)$ diminishes over time, the meaning of Equation 5.3 is that curvature cannot change qualitatively, i.e. a Universe that is closed, flat or open for $t = 0$, will remain so forever. What the equation also tells us is that curvature does change quantitatively, though, and any initial deviation of Ω_{tot} from unity increases, also considerably, as t passes by. This implies that in order for us to observe a value of the density parameter as close to 1 as we estimate it to be nowadays, Ω_{tot} should have been (almost exactly) equal to 1, the critical value, soon after the big bang. The flatness issue is therefore a *fine-tuning* problem.

5.1.2 *The inflationary solution*

accelerated expansion, $\ddot{a} > 0$

Guth [1981] was the first to propose a way out to some of the issues of the standard hot big bang model. The idea behind his work was speculating that during its early stages, and for a limited amount of time, the Universe has undergone an accelerated expansion, called *inflation*. The plain assumption of the existence of a period where $\ddot{a} > 0$ is able to solve the flatness, the horizon, and the monopole problems.

solution to flatness problem

The flatness issue is easily addressed [Liddle and Lyth, 2000] as soon as we notice that if $\ddot{a} > 0$ holds, then for the definition itself of the Hubble parameter, we have that the comoving Hubble length $(Ha)^{-1}$ is such that

$$\frac{d}{dt}(Ha)^{-1} < 0 \tag{5.4}$$

Rewriting Equation 5.3 in terms of $(Ha)^{-1}$ yields

$$(\Omega_{\text{tot}} - 1)(Ha)^2 = Kc^2, \tag{5.5}$$

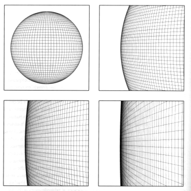

meaning that as time goes by, and as the second term of the left hand side of the equation increases, Ω_{tot} must get closer to one. In other words, as a consequence of the accelerated expansion, the Universe tends to look flatter. This happens because expansion made the size of our observable universe small with respect to any original curvature radius.

solution to horizon problem

Also the solution to the horizon problem is a consequence of the shrinking comoving Hubble length during inflation. In fact, the observable Universe could have originated in a region contained in the sub-horizon scale before the accelerated expansion, hence before inflation caused the comoving horizon scale to decrease.

solution to monopole problem

Similarly, such an accelerated expansion, if long enough, would drastically diminish the monopole density and make it compatible with observations.

5.1.2.1 *Inflation dynamics*

Describing all the dynamical aspects of the main inflationary models would be beyond the purpose of this work. Nonetheless, I would like to briefly describe the main aspects of the inflationary mechanism, focussing on the standard slow-roll scenario, usually associated to models characterized by a single field.

From the Friedmann's Equation 1.6, it is straightforward to see that the condition $\ddot{a} > 0$ is met only when

$$\rho + \frac{3p}{c^2} < 0, \tag{5.6}$$

an entity with a negative pressure

meaning that we need the Universe to be dominated by a species with a *negative pressure*, i.e. $w < -1/3$, in order to have an exponential expansion.

To date, there is no indication on what exactly could be responsible for inflation. Nonetheless, the most credited general hypothesis is that it could originate in conjunction with the phase transition of a generic scalar field subject to a flat potential: As soon as the potential gets slightly tilted, the slowly rolling scalar field produces a negative pressure, as desired. Such a scalar is usually called *inflaton* and denoted by the symbol ϕ.

standard slow-roll scenario

Assuming that the choice of a Robertson-Walker metric is justified, and therefore that the space is homogeneous and isotropic on large scale, and given a generic potential $V(\phi)$, the equation of motion for the inflaton under the influence of $V(\phi)$ reads [Mukhanov, 2005]

$$\ddot{\phi} + 3H\dot{\phi} + \frac{d}{d\phi}V(\phi) = 0. \tag{5.7}$$

This equation differs from the correspondent equation of motion in flat space in the second term, that represent the coupling of the scalar field ϕ to gravity, and acts as a friction.

The H term must be known in order for Equation 5.7 to be solved. It can be proved that

$$H^2 = \frac{8\pi G}{3}\left[\frac{1}{2}\dot{\phi}^2 + V(\phi)\right]. \tag{5.8}$$

slow-roll approximation

The two equations can be solved as soon as the potential form is well known. However, more general considerations can be done, without any restriction on the exact shape of $V(\phi)$, if we use the *slow-roll* approximation. The slow-roll approximation allows us to solve the system for any choice of the potential, assumed that $V(\phi)$ is sufficiently flat. The assumption of flatness is quantified by the condition

$$|\ddot{\phi}| \ll 3H|\dot{\phi}|. \tag{5.9}$$

In fact, we want the second order term of Equation 5.7 to be negligible for ϕ to slowy roll down under the potential action. On the other hand, since the inflation pressure and density turn out to be

$$\rho_\phi = \frac{\dot{\phi}^2}{2} + V(\phi), \quad p_\phi = \frac{\dot{\phi}^2}{2} - V(\phi), \tag{5.10}$$

we also need the following condition to imply a negative pressure, i.e. $p \simeq -\rho$, and therefore for inflation to take place:

$$\frac{1}{2}\dot{\phi}^2 \ll V(\phi). \tag{5.11}$$

The restrictions found in Equation 5.9 and Equation 5.11 can be expressed in terms of the potential by means of the slow-roll parameters

$$\epsilon(\phi) \equiv \frac{M_{Pl}^2}{2}\left(\frac{V'(\phi)}{V(\phi)}\right)^2 \ll 1 \tag{5.12}$$

and

$$|\eta(\phi)| \equiv \left| M_{Pl}^2 \frac{V''(\phi)}{V(\phi)} \right| \ll 1, \tag{5.13}$$

where the primed quantities are derived with respect to ϕ. The condition on parameter $\epsilon(\phi)$ assures that the pressure is negative enough, while the one on $\eta(\phi)$ allows inflation to last as long as it should.

After the slow rolling of ϕ towards an equilibrium configuration ϕ_0, it starts to oscillate around the potential minimum $V(\phi_0)$, until it decays, coupling to other fields. This process is called reheating, and its dynamical details vary quite a lot among different models (refer to Bassett et al. [2006], Allahverdi et al. [2010] for reviews addressing this topic). The reheating constitutes the threshold between inflationary epoch and the standard model framework; after this moment, the radiation starts to dominate.

Many alternatives to this simple scenario exist, like the curvaton mechanism [Mollerach, 1990; Enqvist and Sloth, 2002; Lyth and Wands, 2002], the ekpyrotic scenario [Lehners, 2010], not to mention the entire class of multi field models (for a review see Wands [2008]).

5.2 PRIMORDIAL NON-GAUSSIANITIES

inflation generates a primordial distribution of density fluctuations

One of the most important successes of the inflationary scenario is that it gives a natural explanation for the existence of primordial density fluctuations. What happens is that quantum fluctuations of the scalar field ϕ also get stretched during the accelerated expansion, and imprinted in super-Hubble scales. As soon as the inflaton decays, during the end of inflation, these fluctuations are inherited by the fields with which ϕ gets coupled, namely matter and radiation, revealing themselves as anisotropies of their energy density field. Among the generic predictions that inflation models make for such density perturbations we can find that [Chen, 2010]:

- they are almost scale invariant: In fact, during inflation, each mode withstand a similar expansion;
- they are *approximately* Gaussian.

The second statement holds precisely as far as we consider the perturbations of the scalar field to be linear: In this case the Central Limit Theorem ensures that given that modes have a random distribution, then their superposition will follow a Gaussian statistic.

deviations from Gaussianity

Things are different, though, if the linearity hypothesis for the field perturbations must be discarded. It is the case, for example, when we also have to consider deviations from the slow roll approximation, or the contributions coming from the scalar field interactions with itself, with other fields, or both. In that instance, deviations from

Gaussianity could occur in the primordial density fluctuations distribution. As various inflationary models predict different degrees of non-Gaussianities, measuring the latter could lead to rule out some of these scenarios.

Unlike a normal distribution, that is completely defined by its variance, and therefore by its power spectrum in Fourier space, a non-Gaussian distribution needs higher order momenta to be exhaustively described. Since the primordial distribution of density fluctuations is still Gaussian to a good approximation, deviations can be treated perturbatively, and in this case the bispectrum and trispectrum, defined in Fourier space as follows,

higher order statistics are necessary: bispectrum, trispectrum, ...

$$\langle \Phi(\mathbf{k}_1)\Phi(\mathbf{k}_2)\Phi(\mathbf{k}_3)\rangle = (2\pi)^3 \delta_D\Big(\sum_{n=1}^{3} \mathbf{k}_n\Big) B_\Phi(\mathbf{k}_1, \mathbf{k}_2, \mathbf{k}_3) \quad (5.14)$$

$$\langle \Phi(\mathbf{k}_1)\Phi(\mathbf{k}_2)\Phi(\mathbf{k}_3)\Phi(\mathbf{k}_4)\rangle = (2\pi)^3 \delta_D\Big(\sum_{n=1}^{4} \mathbf{k}_n\Big) T_\Phi(\mathbf{k}_1, \mathbf{k}_2, \mathbf{k}_3, \mathbf{k}_4), \quad (5.15)$$

(where Φ stands for the curvature perturbation) contain a good part of the additional information, apart from being the most accessible higher order momenta, both from an observational and a theoretical point of view.

5.2.1 *Shapes of non-Gaussianities*

There are many different ways a distribution can deviate from a Gaussian. For this reason, non-Gaussianities are usually classified depending on what modes configurations give the strongest signal. In the following sections, I will give a brief description of the three main classifications, and provide an analytical prediction for the bispectrum for local, equilateral, and orthogonal non-Gaussianities.

These three shapes, or a linear combination of them, cover almost the totality of the inflationary models giving deviations from Gaussianity. Nonetheless, there are still some scenarios predicting peculiar shapes of non-Gaussianity, independent from the following (see for instance Chen et al. [2007, 2008]; Barnaby [2010]).

LOCAL NON-GAUSSIANITY Local-shape non-Gaussianity is probably the most studied. In the local ansatz, the curvature perturbation $\Phi(\mathbf{x})$ can be written as a local expansion around a point $\mathbf{x}$ and by means of the perturbation variable $\Phi_g(\mathbf{x})$, that is assumed to satisfy a Gaussian statistics [Wang, 2013]:

local ansatz

$$\Phi(\mathbf{x}) = \Phi_g(\mathbf{x}) + f_{NL}\Phi_g^2(\mathbf{x}) + g_{NL}\Phi_g^3(\mathbf{x}) + \ldots \quad (5.16)$$

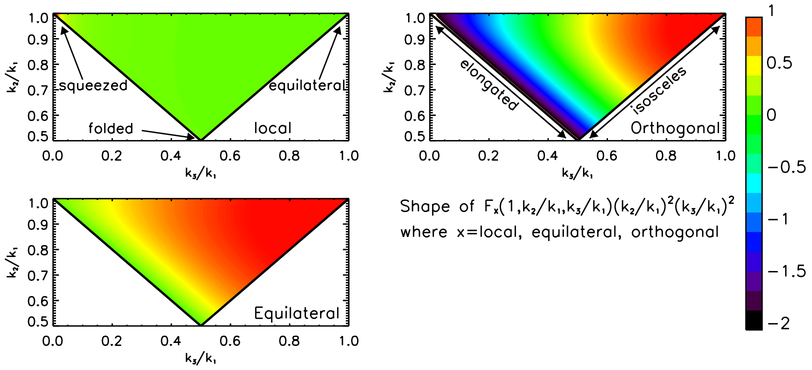

Figure 5.1: Three main shapes for the primordial bispectra, normalized as $B_x(k_1, k_2, k_3)(k_2/k_1)^2(k_3/k_1)^2$ with respect to the maximum value assumed, where x stands for local, equilateral, or orthogonal. In the top-left panel, it can be seen that the local form peaks at squeezed triangle configurations. The equilateral shape (bottom-left panel), on the other hand, provides larger bispectrum values in correspondence of configurations where $k_1 \simeq k_2 \simeq k_3$, whereas the orthogonal form (top-right panel) features a peak at equilateral configurations, and a negative valley all along elongated shapes, i.e. $k_1 = k_2 + k_3$. Figure taken from Komatsu [2010].

Of course this is not a general way for expanding $\Phi(\mathbf{x})$: In fact, in a more general picture, the non linearity parameters could depend on a position vector that is different from the one around which the expansion itself takes place.

This ansatz makes the study of non-Gaussianities much simpler from an analytical point of view. It implicitly assumes that they arise at different spatial points in an independent way, and that they are generated on super-Hubble scales.

The local form bispectrum is given by the relation [Gangui et al., 1994; Verde et al., 2000; Komatsu and Spergel, 2001]

$$\begin{aligned} B_\Phi^{\text{local}}(\mathbf{k}_1, \mathbf{k}_2, \mathbf{k}_3) &= 2f_{\text{NL}}^{\text{local}}\Big[P_\Phi(k_1)P_\Phi(k_2) + P_\Phi(k_2)P_\Phi(k_3) \\ &\quad + P_\Phi(k_3)P_\Phi(k_1)\Big] \\ &= 2A^2 f_{\text{NL}}\Big[k_1^{n_s-4}k_2^{n_s-4} + k_2^{n_s-4}k_3^{n_s-4} \\ &\quad + k_3^{n_s-4}k_1^{n_s-4}\Big], \end{aligned} \tag{5.17}$$

where the approximation $P_\Phi(k) \simeq P_{\Phi_g}(k)$ was made, and where the coefficient

$$A \equiv \frac{P_\Phi(k)}{k^{n_s-4}} \tag{5.18}$$

describes the departure from a scale invariant spectrum [Sefusatti and Komatsu, 2007]. The local bispectrum given in Equation 5.17 peaks among the squeezed triangle configurations, namely when $k_3 \ll k_2 \simeq k_1$ (see top-left panel of Figure 5.1).

The effect of a positive f_{NL} would be, for instance, to enhance the right-hand tail of the density distribution, and suppress the left-hand one, making overdensities overall more likely to happen, and on the contrary, underdensities less likely, with respect to a Gaussian distribution. Vice versa, of course, for a negative f_{NL}.

Local shape non-Gaussianities occur, in general, in models where non-linearities are expected to be produced by super-horizon evolution of perturbation; this is typically expected to happen in several types of multi-field models [Lyth et al., 2003; Zaldarriaga, 2004; Lyth and Rodríguez, 2005; Bond et al., 2009].

One peculiarity of local non-Gaussianity resides in the fact that, as Creminelli and Zaldarriaga [2004] proved, every single-inflation model give a bispectrum like

$$B_{\Phi}^{\text{local}}(\mathbf{k}_1,\mathbf{k}_2,\mathbf{k}_3) = \frac{5}{3}(1-n_s)P_{\Phi}(k_1)P_{\Phi}(k_3), \quad k_3 \ll k_1, k_2 \tag{5.19}$$

in the squeezed triangle limit. Such a case would imply an extremely small value for f_{NL}^{local}. Detecting a f_{NL}^{local} sensibly different from zero would then rule out the entire class of single-field inflationary.

single-field models do not predict local non-Gaussianities

EQUILATERAL NON-GAUSSIANITY Equilateral non-Gaussianities are characterized by a bispectrum that peaks, as bottom-left panel of Figure 5.1 shows, at equilateral configurations ($k_1 \simeq k_2 \simeq k_3$). This form is almost orthogonal to the local one, meaning that they can be detected independently, and its bispectrum reads [Creminelli et al., 2006]

$$\begin{aligned} B_{\Phi}^{\text{equil}}(\mathbf{k}_1,\mathbf{k}_2,\mathbf{k}_3) = \; & 6A^2 f_{NL}^{\text{equil}}\Big[-2\big(k_1k_2k_3\big)^{2(n_s-4)/3} \\ & -\big(k_1k_2\big)^{n_s-4} - \big(k_2k_3\big)^{n_s-4} - \big(k_3k_1\big)^{n_s-4} \\ & +\big(k_1^{(n_s-4)/3}k_2^{2(n_s-4)/3}k_3^{n_s-4} \\ & +5 \text{ perm.}\big)\Big]. \end{aligned} \tag{5.20}$$

In general, a positive equilateral bispectrum corresponds to having strong overdensities encircled by large regions characterized by a milder underdensity; on the other hand, a negative equilateral bispectrum describes a higher likelihood to have very concentrated under densities surrounded by regions with a blander overdensity [Lewis, 2011].

This type of non-linearities arises from several inflationary models [Arkani-Hamed et al., 2004; Seery and Lidsey, 2005; Chen et al., 2007; Cheung et al., 2008; Li et al., 2008]. In general, equilateral non-Gaussianities are produced in models with non-canonical kinetic terms, such as the well known Dirac-Born-Infeld (DBI) inflation [Alishahiha et al., 2004; Silverstein and Tong, 2004]. It is worth pointing out that a positive, and almost entirely equilateral bispectrum also arises from non-linear collapse of dense filaments in the large scale structure [Lewis, 2011].

ORTHOGONAL NON-GAUSSIANITY This form is constructed to be orthogonal to both local and equilateral forms, and therefore independent. It actually arises from a linear combination of higher-derivative interaction terms of the scalar field. Its bispectrum

$$\begin{aligned} B_{\Phi}^{\text{ortho}}(\mathbf{k}_1,\mathbf{k}_2,\mathbf{k}_3) &= A^2 f_{\text{NL}}^{\text{ortho}}\Big[-8\big(k_1k_2k_3\big)^{2(n_s-4)/3} \\ &\quad -3\big(k_1k_2\big)^{n_s-4} - 3\big(k_2k_3\big)^{n_s-4} - 3\big(k_3k_1\big)^{n_s-4} \\ &\quad +\big(3k_1^{(n_s-4)/3}k_2^{2(n_s-4)/3}k_3^{n_s-4} \\ &\quad +5 \text{ perm.}\big)\Big], \end{aligned} \tag{5.21}$$

when normalized in amplitude, i.e. $B_{\Phi}^{\text{ortho}} \cdot (k_2/k_1)^2 \cdot (k_3/k_1)^2$, features a peak for the equilateral configurations, and a negative trough in correspondence of the elongated ones ($k_1 = k_2 + k_3$), as Figure 5.1 displays in the top-right panel.

5.2.2 *The Suyama-Yamaguchi inequality*

The Suyama-Yamaguchi inequality is a very general result that links the two non-linearity parameters f_{NL} and τ_{NL}, introduced and proved for the first time by Suyama and Yamaguchi [2008].

In the local ansatz, once performed the expansion of Equation 5.16, we notice that the cubic term does not contribute to the bispectrum, instead it generates the trispectrum, that can be written as follows

$$\begin{aligned} T_{\smile}(\mathbf{k}_1,\mathbf{k}_2,\mathbf{k}_3,\mathbf{k}_4) &= A^3\Big\{6g_{\text{NL}}\Big[k_1^{n_s-4}k_2^{n_s-4}k_3^{n_s-4} + 3 \text{ perm.}\Big] \\ &+ \frac{25}{18}\tau_{\text{NL}}\Big[k_1^{n_s-4}k_3^{n_s-4}|\mathbf{k}_1+\mathbf{k}_2|^{n_s-4} \\ &+ 11 \text{ perm.}\Big]\Big\}, \end{aligned} \tag{5.22}$$

and that depends on the parameters g_{NL} and τ_{NL}

Generalizing the local ansatz to multi-field inflation by means of the δN formalism [Starobinskiĭ, 1985; Sasaki and Stewart, 1996], we can expand the primordial curvature perturbation ζ, whose relation to Φ is $\zeta = 5\Phi/3$, in terms of the inflation perturbations $\delta\phi$ and the

e-folding number

e-folding number, defined as

$$N(t_i, t_f, \mathbf{r}) = \int_{t_i}^{t_f} H(t, \mathbf{r}) dt, \tag{5.23}$$

namely the time integral of the Hubble parameter, evaluated locally. By means of such an expansion, it is possible to write the non-linear parameters in terms of derivatives of N with respect to the i-th inflation perturbation $\delta\phi_i$, i. e. $N_i = \partial N/\partial\phi_i$ (for a detailed derivation, please see Suyama and Yamaguchi [2008]):

$$f_{NL} = \frac{5\sum_{ij} N_{ij} N_i N_j}{6(\sum_i N_i^2)^2}, \quad g_{NL} = \frac{25\sum_{ijk} N_{ijk} N_i N_j N_k}{54(\sum_i N_i^2)^3}, \tag{5.24}$$

and

$$\tau_{NL} = \frac{\sum_{ijk} N_{ij} N_{ik} N_j N_k}{(\sum_i N_i^2)^3}. \tag{5.25}$$

Due to the well known Cauchy-Schwarz inequality, that can be expressed as [Lin and Wang, 2010]

$$\sum_{ij} (A_i A_i)(B_j B_j) \geqslant \sum_{ij} (A_i B_i)(A_j B_j), \tag{5.26}$$

Suyama-Yamaguchi inequality

it can be proved that there exists a general relation between f_{NL} and τ_{NL},

$$\tau_{NL} \geqslant \left(\frac{6}{5} f_{NL}\right)^2, \tag{5.27}$$

called *Suyama-Yamaguchi inequality*.

Suyama-Yamaguchi inequality as a tool to discriminate among inflationary models

Such a relation should always hold. Nonetheless, it was calculated that some inflationary models could predict a violation of the inequality. Hence, detecting a departure from the condition in Equation 5.27, could help us ruling out some scenarios.

5.2.3 *Measuring primordial non-Gaussianities*

scale-dependent f_{NL}

Many efforts have been made, over the years, to provide independent methods able to constrain the degree of primordial non-Gaussianities in the density distribution. Not only do diverse approaches experience different kinds of systematic errors, yielding in this way complementary results: they also often probe different scales. This last fact is of fundamental importance if we consider f_{NL} to be scale-dependent, as a number of studies seem to suggest [Byrnes et al., 2010a; Chen, 2005; Bartolo et al., 2010; Riotto and Sloth, 2011].

constraints from CMB

The tightest constraints on primordial non-Gaussianities definitely come from the study of CMB and the bispectrum of temperature fluctuations $\Delta T/T$ [Komatsu, 2003; Casaponsa et al., 2011; Komatsu et al., 2011]. One undeniable advantage of this channel is that the distribution of temperature anisotropies that we observe is not so affected by deviations from Gaussianity coming from the non-linear growth of perturbations. The most recent observations constraining the nonlinearity parameter f_{NL} come from Planck [Planck Collaboration et al., 2013b] and give

$$\begin{aligned} f_{NL}^{local} &= 2.7 \pm 5.8 \\ f_{NL}^{equil} &= -42 \pm 75 \\ f_{NL}^{ortho} &= -25 \pm 39 \end{aligned}$$

constraints from LLS

Verde [2010] and Fedeli et al. [2011a] , among others, have worked on the possibility to detect non-Gaussianities from large scale structure statistics. These class of methods, of course, is highly affected by non-Gaussianities coming from structure formation, and therefore needs an adequate mechanism able to distinguish between primordial and non-primordial deviations from a normal distribution. Gravitational lensing has also been proposed [Fedeli et al., 2011b; Pace et al., 2011; Jeong et al., 2011], although observational constrains coming from this approach, so far, have focussed more on non-Gaussianities generated by non-linear structure formation. A discussion on possible observational constraints on primordial non-Gaussianities coming from weak lensing in the near future can be found in Schäfer et al. [2012] and will be presented in the next Chapter.

constraints from lensing

6

A WEAK LENSING VIEW ON PRIMORDIAL NON-GAUSSIANITIES

The content of this chapter is based on the paper "A weak lensing view on primordial non-Gaussianities" [Schäfer et al., 2012]. The development and contribution of the author of this Thesis to the following work was testing the numerical code and the convergence of the Monte-Carlo integration routines.

A weak lensing study of primordial non-Gaussianities via convergence bispectrum measurements would be of great interest. In fact, lensing sums up two interesting features:

- since lensing is not affected, in principle, by galaxy bias, it has smaller systematic errors than other large scale structure probes, such as cluster counts or the study of galaxy bispectrum;
- also, it probes smaller scales than CMB does, providing independent constraints on a possible scale dependence of the non-linearity parameter f_{NL}, for example [Lo Verde et al., 2008].

On the other hand, classical weak lensing suffers some limitations. Among the ones that could affect the problem at hand, lies the fact that all weak lensing statistics depend on integrals along the line-of-sight. In this integration, many independent effects could sum up, hence reducing the information on the primordial non-Gaussianities inherited by the convergence bispectrum [Jeong et al., 2011]. As a consequence, we expect weak lensing to be less sensitive to primordial non-linearities than probes like CMB.

In order to test weak lensing sensitivity, though, some questions naturally arise:

1. Is the power of the signal of the three different shapes of primordial non-Gaussianity compatible with a detection by a future survey like Euclid?

2. Suppose a wrong choice of the type of bispectrum (local, equilateral, or orthogonal) is made for fitting the data: How, and by how much would such a mistake affect the f_{NL} measurement? And, how likely would it be to notice such a mistake?

3. What kind of repercussions would a non-exact subtraction of the non-Gaussianities coming from structure formation have on the f_{NL} measurement?

In the present Chapter, I will recapitulate our main results published in Schäfer et al. [2012] concerning the aforementioned issues. Section 6.1 will introduce the basis of the analysis, by deriving the observable convergence bispectrum and giving an estimate of the much stronger bispectrum coming from non-linear structure formation, that has to be subtracted from the signal in order to recover the primordial non-Gaussianity signal. Section 6.2, Section 6.3, and Section 6.4 will give answers to the previous questions, by means of a calculation of the signal-to-noise ratio, and by a statistical analysis that will try to investigate what kind of consequences could a wrong assumption or a wrong fit have on the measurement of f_{NL}.

6.1 WEAK LENSING CONVERGENCE BISPECTRUM

Before addressing the mentioned problems, let me concisely introduce how we get from the original bispectra coming primordial non-Gaussianities or non-linear structure formation, to the observed, weak lensing, convergence bispectrum.

I would like to start from the statistics coming from primordial deviations from Gaussianity. Given the bispectrum with respect to the distribution of the potential $B_\Phi(\mathbf{k}_1, \mathbf{k}_2, \mathbf{k}_3)$, defined for local, equilateral and orthogonal non-Gaussianities as shown in Equation 5.17, Equation 5.20, and Equation 5.21, then the bispectrum of the density field reads

density bispectrum

$$B_\delta(\mathbf{k}_1, \mathbf{k}_2, \mathbf{k}_3, a) = \prod_{i=1}^{3} \left(\frac{2D_+(a)}{3\Omega_m} T(k_i)(\chi_H k_i)^2 \right) B_\Phi(\mathbf{k}_1, \mathbf{k}_2, \mathbf{k}_3), \quad (6.1)$$

with $T(k)$ and $D_+(a)$ as, respectively, the transfer function and the growth function. This result is of course obtained by means of the comoving Poisson equation [Munshi et al., 2012], linking the potential distribution to the density field $\delta(k, a)$:

$$\nabla^2 \Phi = \frac{3\Omega_{m0}}{2\chi_H^2} \frac{D_+(a)}{a} \delta. \quad (6.2)$$

convergence bispectrum

Once obtained $B_\delta(\mathbf{k}_1, \mathbf{k}_2, \mathbf{k}_3, a)$, the projection of the flat-sky *convergence* bispectrum B_κ is then [Schneider et al., 1998; Takada and Jain, 2003a,b, 2004; Dodelson and Zhang, 2005]

$$B_\kappa(\boldsymbol{\ell}_1, \boldsymbol{\ell}_2, \boldsymbol{\ell}_3) = \int_0^{\chi_H} \frac{d\chi}{\chi^4} W^3(\chi) B_\delta(\mathbf{k}_1, \mathbf{k}_2, \mathbf{k}_3, a), \tag{6.3}$$

where the Limber equation was used [Limber, 1954], and $\mathbf{k}_i = \boldsymbol{\ell}_i/\chi$ for $i = 1, 2, 3$. Unfortunately, since a weak lensing approach implies a line-of-sight integration, we can already forecast that many, independent effects will add up to the information, therefore reducing the power of the non-Gaussian signal because of the Central Limit theorem [Jeong et al., 2011].

spherical convergence bispectrum

The observed spherical convergence bispectrum is obtained from $B_\kappa(\boldsymbol{\ell}_1, \boldsymbol{\ell}_2, \boldsymbol{\ell}_3)$ via the following relation

$$B_\kappa(\ell_1, \ell_2, \ell_3) \simeq \begin{pmatrix} \ell_1 & \ell_2 & \ell_3 \\ 0 & 0 & 0 \end{pmatrix} \sqrt{\frac{\prod_{p=1}^{3}(2\ell_p + 1)}{4\pi}}\, B_\kappa(\boldsymbol{\ell}_1, \boldsymbol{\ell}_2, \boldsymbol{\ell}_3), \tag{6.4}$$

where the first term on the right hand side of the equation is the Wigner-3j symbol, whose purpose is to select only the configurations that satisfy the triangle inequality, and set the bispectrum to zero for all the others. A 3d representation of the values assumed by the (dimensionless) bispectra B_κ is shown in Figure 6.1.

structure formation bispectrum

As already mentioned, primordial non-Gaussianities are not the only source of deviations from normality. In fact, non-linearities coming from structure formation also generate a non-Gaussian contribution to the density field statistics, that can be described by the bispectrum term [Buchert, 1994; Bernardeau et al., 2002]

$$B_\delta^{SF}(\mathbf{k}_1, \mathbf{k}_2, \mathbf{k}_3, a) = \sum_{i,j=1\,(i\neq j)}^{3} D_+^4(a) M(\mathbf{k}_i, \mathbf{k}_j) P(k_i) P(k_j), \tag{6.5}$$

with $M(\mathbf{k}_i, \mathbf{k}_j)$ describing the coupling between modes:

$$M(\mathbf{k}_i, \mathbf{k}_j) = \frac{10}{7} + \left(\frac{k_i}{k_j} + \frac{k_j}{k_i}\right) \frac{\mathbf{k}_i \mathbf{k}_j}{k_i k_j} + \frac{4}{7} \left(\frac{\mathbf{k}_i \mathbf{k}_j}{k_i k_j}\right)^2. \tag{6.6}$$

The quantity $M(\mathbf{k}_i, \mathbf{k}_j)$ assumes the largest values when the vectors $\mathbf{k}_i$ and $\mathbf{k}_j$ are parallel, i. e. $x = 1$, so that the strongest non-Gaussian contribute comes from squeezed configurations. Since B_δ^{SF} is much stronger than the primordial non-Gaussianities bispectrum, this contribution must be subtracted in order to recover the signal coming from primordial non-linearities.

6.2 EXPECTED SIGNAL TO NOISE RATIO

Once we have the expression for the convergence bispectra, the first question can be addressed: We want to find out how strong the signal coming from primordial non-Gaussianities, and encoded in B_κ, is.

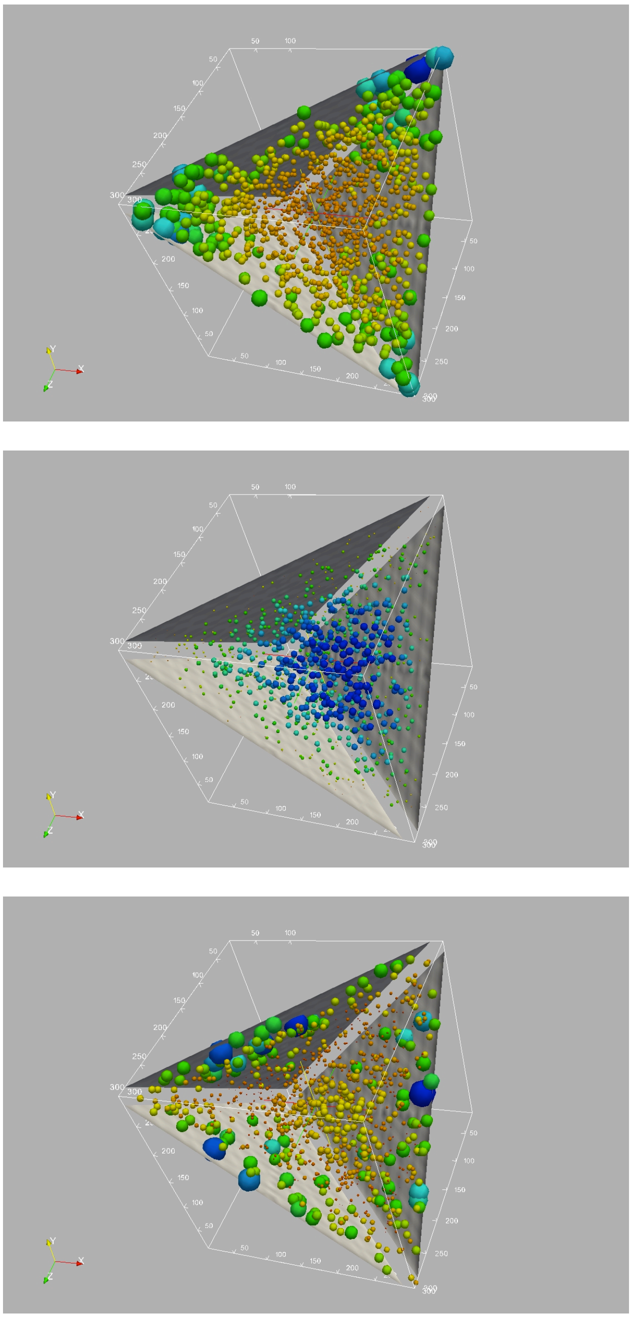

Figure 6.1: Dimensionless convergence bispectrum $(\ell_1\ell_2\ell_3)^{4/3}B_\kappa(\ell_1,\ell_2,\ell_3)$ for local (top panel), equilateral (middle panel), and orthogonal non-Gaussianity (bottom panel), plotted in the configurations space. Size and colors of the blobs are proportional to the dimensionless bispectrum values. It is evident how the properties of the original bispectra are inherited by the weak lensing B_κ. The top and middle panel, for instance, clearly show how the corresponding bispectra peak for, respectively, squeezed and equilateral configurations.

Let the covariance be [Hu, 2001; Takada and Jain, 2003a]

$$\mathrm{cov}(\ell_1,\ell_2,\ell_3) = \frac{\Delta(\ell_1,\ell_2,\ell_3)}{f_{\mathrm{sky}}}\tilde{C}(\ell_1)\tilde{C}(\ell_2)\tilde{C}(\ell_3) \tag{6.7}$$

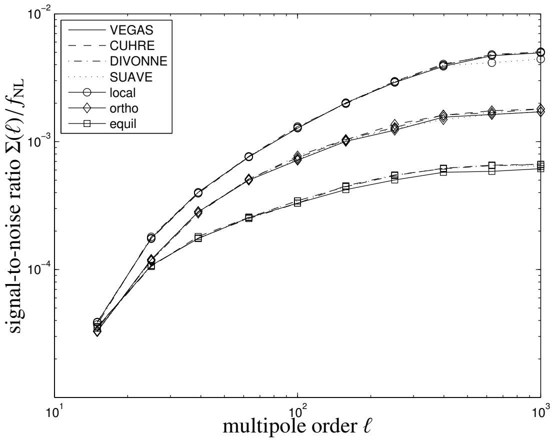

Figure 6.2: Cumulative signal-to-noise ratio $\Sigma(\ell)/f_{NL}$ as the maximum ℓ used in its evaluation increases. The ratio is evaluated for local (circles), orthogonal (rhombi), and equilateral (squares) non-Gaussianities. Different line-types represent the four CUBA algorithms, showing that they agree quite well for the calculation of $\Sigma(\ell)$.

The term f_{sky} stands for the portion of sky covered by a generic survey, whereas $\tilde{C}(\ell)$ is the observed power spectrum; both these quantity are set accordingly to Euclid predictions. On the other hand, $\Delta(\ell_1, \ell_2, \ell_3)$ takes care of the triangle configurations multiplicity. Given the expression for the covariance, the cumulative signal-to-noise ration can be evaluated:

cumulative signal-to-noise

$$\Sigma^2(\ell) = \sum_{\ell_1=\ell_{min}}^{\ell} \sum_{\ell_2=\ell_{min}}^{\ell} \sum_{\ell_3=\ell_{min}}^{\ell} \frac{B_\kappa^2(\ell_1, \ell_2, \ell_3)}{\mathrm{cov}(\ell_1, \ell_2, \ell_3)}. \tag{6.8}$$

A direct summation of Equation 6.8 among all the possible configurations of ℓ_1, ℓ_2, ℓ_3 would be extremely expensive from a computational point of view. A way out to this problem is given by Monte-Carlo integrations. In this case, the CUBA library is used [Hahn, 2005], consisting of the four different algorithms Vegas, Suave, Divonne, and Cuhre. The cumulative $\Sigma(\ell)$ is calculated using the four algorithms, whose results seem to agree with each other, and for the three shapes of non-Gaussianities, and its ratio with respect to the non-linearity parameter f_{NL} is presented in Figure 6.2. The conclusions that can be drawn from the plot are:

- with Euclid, the signal coming from primordial non-Gaussianity bispectrum can only be detected for values of f_{NL} much larger than 100;
- this is true, at least, for local non-Gaussianity, that seems to be the most easily detectable type; forms like the orthogonal one would need an even larger degree of non-Gaussianity, and the

equilateral type of non-Gaussianity directly follows, having the smallest signal (almost one order of magnitude smaller than the local type); such a difference in the magnitude of the signal for the three non-Gaussianity forms is also visible in Figure 6.3;

- the consequently estimated conditional Cramér-Rao bounds result to be much weaker than probes like, for instance, CMB. In fact they read

$$\sigma_{f_{\mathrm{NL}}} = \begin{cases} 200, & \text{local} \\ 575, & \text{orthogonal} \\ 1628, & \text{equilateral.} \end{cases} \tag{6.9}$$

The choice of stopping the $\Sigma(\ell)$ calculation at $\ell = 1000$ is motivated by the fact the the signal is not considerably increasing after this threshold. Moreover, $\ell > 1000$ correspond to scales that start to be affected by baryonic physics and intrinsic alignments [Semboloni et al., 2008, 2011].

6.3 CONSEQUENCES OF A WRONG BISPECTRUM CHOICE

The next matter aims to understand what happens when we fit the data with the wrong type of bispectrum. One can quantify the misestimation of f_{NL} by means of the multiplicative bias α, i. e. the ratio between the non-linearity parameter inferred from the wrong bispectrum, f^{w}_{NL}, and the true f^{t}_{NL}. The quantity α is calculated by minimizing the derivative of the functional

$$\chi^2 = \sum_{\ell_1=\ell_{\min}}^{\ell} \sum_{\ell_2=\ell_{\min}}^{\ell} \sum_{\ell_3=\ell_{\min}}^{\ell} \frac{\left[\alpha B^{\mathrm{wrong}}_{\kappa}(\ell_1,\ell_2,\ell_3) - B^{\mathrm{true}}_{\kappa}(\ell_1,\ell_2,\ell_3)\right]^2}{\mathrm{cov}(\ell_1,\ell_2,\ell_3)}, \tag{6.10}$$

with respect to α itself. The superscripts t and w stand of course for the true and wrong bispectra.

The ratio α (or better, its departure from unity) is depicted in Figure 6.4a. Apparently,

- differences between the wrongly inferred f_{NL} and the true one start to show up as soon as relatively large multipoles are considered; in fact, here is where the non-Gaussianity signal is stronger;
- the majority of the possible wrong fittings lead to an underestimation of f_{NL}, and the largest error (almost half an order of magnitude) is made when trying to fit a local non-Gaussianity with an orthogonal one;

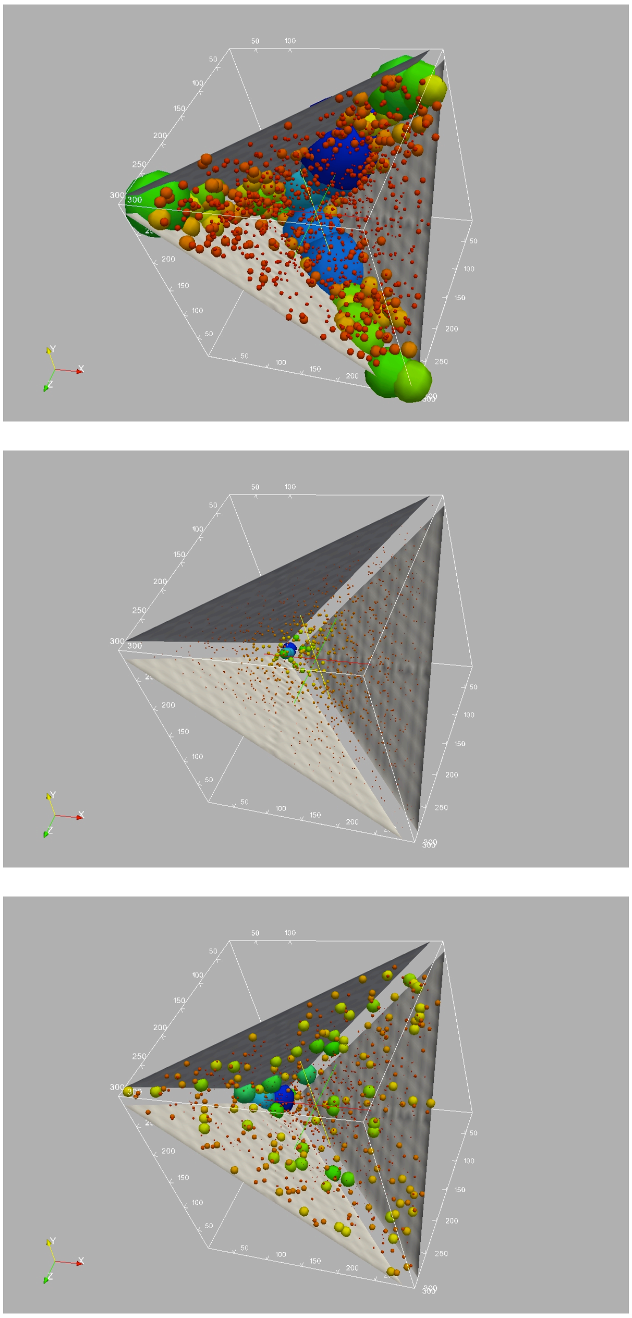

Figure 6.3: Dimensionless signal-to-noise ratio in the configurations space, $B_\kappa(\ell_1,\ell_2,\ell_3)/\sqrt{\text{cov}(\ell_1,\ell_2,\ell_3)}$. Again, size and colors of the blobs are proportional to the bispectrum values, and the top, middle, and bottom panels depict respectively bispectra for local, equilateral, and orthogonal non-Gaussianity. Local non-Gaussianity shows a much higher signal-to-noise ratio for squeezed configurations, whereas the equilateral one presents a (weak) signal only for very small values of ℓ. Signal-to-noise coming from orthogonal non-Gaussianity, on the other hand, seems more uniform.

- on the other hand, an overestimate (by a factor of around ±3) of f_{NL} occurs when an equilateral bispectrum is used to fit what is, truly, a local B_κ.

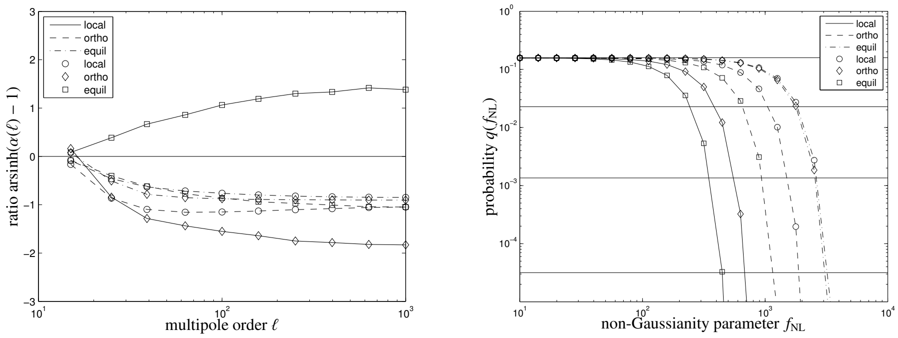

(a) (b)

Figure 6.4: *Left panel*: ratio $\alpha(\ell) = f^{w}_{NL}/f^{t}_{NL}$ as a function of the maximum multipole ℓ used in the computation of the χ^2 functional. The line styles indicate the true non-Gaussianity model: local (solid line), orthogonal (dashed line), equilateral (dash-dotted line). Markers, on the other hand, stand for the non-Gaussianity model that has been wrongly chosen to fit the hypothetical data: local (circles), orthogonal (rhombi), equilateral (squares). *Right panel*: probability $q(f_{NL})$ of obtaining data more extreme than those considered when a wrong non-Gaussianity model is chosen to fit the data. Again, line types describe the true underlying model: local (solid line), orthogonal (dashed line), equilateral (dash-dotted line). Different markers represent the wrong model chosen to explain the data: local (circles), orthogonal (rhombi), equilateral (squares). The maximum multipole ℓ used for the calculation is 1000, and the horizontal lines stand for $1, 2, 3, 4\sigma$ confidence intervals.

Hence, making a wrong ansatz regarding the type of bispectrum can lead to serious misestimates of the non-Gaussianity parameter.

is it likely to notice that a wrong bispectrum is fitting the data?

Is it possible to notice such a mistake? Figure 6.4b addresses this question by means of the quantity $q(f_{NL})$, i. e. the probability - given a certain, true f_{NL}[1] - of obtaining data more extreme than those considered. The result of the analysis is that this probability starts to get considerably small only when the true f_{NL} is of the order of 100 or larger. In fact, the strength of the signal for smaller degrees of non-Gaussianity is such that no difference between data and the wrong model are visible.

6.4 SUBTRACTION OF STRUCTURE FORMATION BISPECTRUM

Another problem concerns the subtraction from the total bispectrum of the part bringing the contribution of structure formation B^{SF}_{κ} (see Equation 6.6). Since the prediction of this quantity depends on cosmological parameters, our uncertainty on the constraints on the latter

---

[1] a Gaussian likelihood was assumed.

can propagate, yielding some possible errors in the measurement of the primordial non-Gaussianity degree.

In a similar way as in Section 6.3, one can define a functional describing the fit of the true bispectrum B_κ^t

$$\chi^2 = \sum_{\ell_1=\ell_{\min}}^{\ell} \sum_{\ell_2=\ell_{\min}}^{\ell} \sum_{\ell_3=\ell_{\min}}^{\ell} \frac{\left[\alpha B_\kappa^t(\ell_1,\ell_2,\ell_3) - \Delta B_\kappa(\ell_1,\ell_2,\ell_3)\right]^2}{\mathrm{cov}(\ell_1,\ell_2,\ell_3)}, \tag{6.11}$$

where the quantity

$$\Delta B_\kappa(\ell_1,\ell_2,\ell_3) = B_\kappa^t(\ell_1,\ell_2,\ell_3) + B_\kappa^{t,SF}(\ell_1,\ell_2,\ell_3) - B_\kappa^{w,SF}(\ell_1,\ell_2,\ell_3) \tag{6.12}$$

contains the information about the subtraction of the wrong structure formation bispectrum $B_\kappa^{w,SF}$. Again, by minimizing χ^2 with respect to $\alpha = f_{NL}^w / f_{NL}$, one can calculate the distribution of the bias between wrong and true f_{NL}, i.e. $\delta = \alpha - 1$.

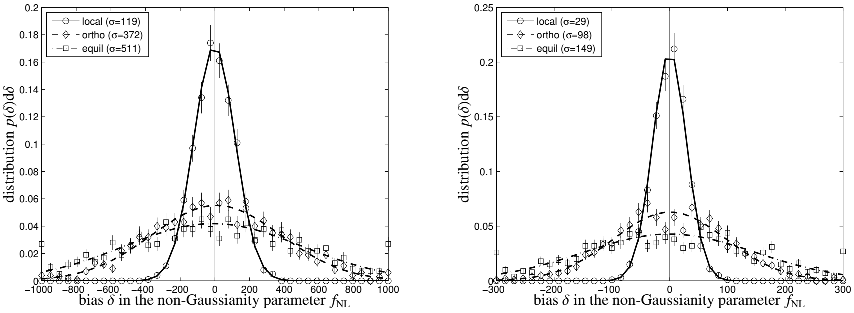

(a) (b)

Figure 6.5: Distributions of the bias between f_{NL}^w and f_{NL}^t in the case where uncertainties on cosmological parameter determination lead to a wrong or non complete subtraction of the structure formation bispectrum for local (solid line, circles), equilateral (dash-dotted line, squares), orthogonal (dashed line, rhombi) primordial non-Gaussianity. The two panels show the distributions for a prior corresponding to Euclid weak lensing and BAO results (*left panel*), and when one adds also data coming from PLANCK's CMB temperature and polarization analysis to the previous prior (*right panel*).

Figure 6.5 shows this distribution $p(\delta)d\delta$ for the three non-Gaussianity shapes, and the two panels display different choices of prior. In particular, Figure 6.5a displays the bias distribution when a prior coming from Euclid weak lensing and BAO results was used. On the other hand, Figure 6.5b makes use of a better prior, namely weak lensing and BAO coming from Euclid, plus the expected PLANCK's constraints on CMB temperature and polarization spectra.

6.5 CONCLUSIONS

Summarizing, the signal starts to dominate the noise for values of f_{NL} of $200, 575, 1628$ for local, orthogonal, and equilateral non-Gaussianities. Also, fitting data with a wrong bispectrum type can lead to under- or overestimates of f_{NL} up to a factor of $|3|$, and such an error would become visible only for $f_{NL} \sim 200$ or greater. Concerning a partially wrong subtraction of the signal coming from structure formation, it is found that the propagation on the estimate of f_{NL} is dependent on the prior considered. In particular a prior consisting in data coming from Euclid weak lensing and BAO analyses, and PLANCK's study of the temperature and polarization maps, would yield typical uncertainties of $29, 98, 149$ for local, orthogonal, and equilateral non-Gaussianities, respectively. These values seem to be much less of the statistical accuracy.

Concluding, even though a weak lensing approach to measure primordial non-Gaussianity seems to have, as expected, a smaller sensitivity than the cosmic microwave background, it nevertheless stands out as an independent investigation, able to probe smaller scales than CMB and hence a precious test for a possible scale dependence of f_{NL}.

In the next chapter I will propose a more definite application of weak lensing to the study of primordial non-Gaussianities. In particular, I will treat the possibility of testing the validity of the Suyama-Yamaguchi inequality (introduced in Section 5.2.2) with weak gravitational lensing.

7

A TEST OF THE SUYAMA-YAMAGUCHI INEQUALITY

This chapter exactly reproduces the content of the paper "A test of the Suyama-Yamaguchi inequality from weak lensing" [Grassi et al., 2013]. The original analysis we carried out and the results are presented in Section 7.5, Section 7.6, Section 7.7, Section 7.8, and summarized in Section 7.9.

ABSTRACT

We investigate the weak lensing signature of primordial non-Gaussianitites of the local type by constraining the magnitude of the weak convergence bi- and trispectra expected for the Euclid weak lensing survey. Starting from expressions for the weak convergence spectra, bispectra and trispectra, whose relative magnitudes we investigate as a function of scale, we compute their respective signal to noise ratios by relating the polyspectra's amplitude to their Gaussian covariance using a Monte-Carlo technique for carrying out the configuration space integrations. In computing the Fisher-matrix on the non-Gaussianity parameters f_{NL}, g_{NL}, and τ_{NL} with a very similar technique, we can derive Bayesian evidences for a violation of the Suyama-Yamaguchi relation $\tau_{NL} \geqslant (6/5 f_{NL})^2$ as a function of the true f_{NL} and τ_{NL}-values and show that the relation can be probed down to levels of $f_{NL} \simeq 10^2$ and $\tau_{NL} \simeq 10^5$. In a related study, we derive analytical expressions for the probability density that the SY-relation is exactly fulfilled. We conclude with an outlook on the levels of non-Gaussianity that can be probed with tomographic lensing surveys.

7.1 INTRODUCTION

Advances in observational cosmology made it possible to probe models of the early Universe and the mechanisms that can generate small seed perturbations in the density field from which the cosmic large-scale structure grew by gravitational instability. One of the most prominent of these models is inflation, in which the Universe underwent an extremely rapid exponential expansion and where small fluctuations in the inflationary field gave rise to fluctuations in the gravitational potential and which then imprinted these fluctuations onto all cosmic fluids [for reviews, see Bartolo et al., 2004; Seery et al., 2007; Komatsu et al., 2009; Komatsu, 2010; Desjacques and Seljak, 2010b,a; Verde, 2010; Lehners, 2010; Jeong et al., 2011; Wang, 2013; Martin et al., 2013; Lesgourgues, 2013]. Observationally, inflationary models can be distinguished by the spectral index n_s along with a possible scale dependence, the scalar to tensor-ratio r and, perhaps most importantly, the non-Gaussian signatures, quantified by n-point correlation functions or by polyspectra of order n in Fourier-space. They are of particular interest as the full set of non-Gaussianity parameters can be mapped onto a Taylor-expansion of the inflaton potential, providing important constraints. Additionally, the configuration space dependence of the polyspectra yields valuable information on the type of inflationary model [Byun and Bean, 2013].

The (possibly non-Gaussian) density fluctuations are subsequently imprinted in the cosmic microwave background (CMB) as temperature anisotropies [Fergusson and Shellard, 2009; Fergusson and Shellard, 2007; Fergusson et al., 2010; Pettinari et al., 2013], in the matter distribution which can be probed by e.g. gravitational lensing and in the number density of galaxies. Hereby it is advantageous that the observable is linear in the field whose statistical property we investigate. In case of linear dependence the n-point functions of the observable field can be mapped directly onto the corresponding n-point function of the primordial density perturbation, which reflects the microphysics of the early Universe.

The first important measurement quantifying non-Gaussianity is the parameter f_{NL} which describes the skewness of inflationary fluctuations and determines the amplitude of the bispectrum. Not only the bispectrum but also the trispectrum can successfully be constrained by future precisions measurements, where the parameters g_{NL} and τ_{NL} determine the trispectrum amplitude. The complementary analysis of both the bi- and the trispectra in the future experiments will make us able to extract more information about the mechanism of generating the primordial curvature perturbations and constrain the inflationary potential. Therefore, it is an indispensable task for cosmology to obtain the configuration space dependence for the higher polyspectra and to make clear predictions for the non-Gaussianity parameters. The non-Gaussianities are commonly expressed as perturbations of modes of the potential $\propto k^{n_s-4}/2$ but can in principle have scale dependences [Lo Verde et al., 2008; Sefusatti et al., 2009; Riotto and Sloth, 2011; Byrnes et al., 2010b; Becker et al., 2011; Byrnes et al., 2010b].

The description of inflationary non-Gaussianities is done in a perturbative way and for the relative magnitude of non-Gaussianities of different order the Suyama-Yamaguchi (SY) relation applies [Suyama and Yamaguchi, 2008; Suyama et al., 2010; Smith et al., 2011a; Sugiyama, 2012; Beltrán Almeida et al., 2013; Rodríguez et al., 2013], which in the most basic form relates the amplitudes of the bi- and of the trispectrum. Recently, it has been proposed that testing for violation of the SY-inequality would make it possible to distinguish between different classes of inflationary models. In this work we focus on the relation between the non-Gaussianity parameters f_{NL} and τ_{NL} for a local model, and investigate how well the future Euclid survey can probe the SY-relation: The question we address is how likely would we believe in the SY-inequality with the infered f_{NL} and τ_{NL}-values. We accomplish this by studying the Bayesian evidence [Trotta, 2007, 2008] providing support for the SY-inequality.

Suyama-Yamaguchi inequality

Models in which a single field generates the primordial curvature perturbation predict an equality between one term of the trispectrum and the bispectrum, $\tau_{NL} = (6f_{NL}/5)^2$ (provided that the loop corrections are not anomalously large, if they are then g_{NL} should also be observable). Violation of this consistency relation would prove that more than one light field present during inflation had to contribute towards the primordial curvature perturbation. However a verification of the equality would not imply single field inflation, rather that only one of the fields generated perturbations. In fact any detection of non-Gaussianity of the local form will prove that more than one field was present during inflation, because single field inflation predicts negligible levels of non-Gaussianity. A detection of $\tau_{NL} > (6f_{NL}/5)^2$ would prove that not only that inflation was of the multi-field variety, but also that multiple-fields contributed towards the primordial perturbations, which are the seeds which gave rise to all the structure in the universe today.

single-field models predictions

A violation of the Suyama-Yamaguchi inequality would come as a big surprise, since the inequality has been proved to hold for all models of inflation. Even more strongly, in the limit of an infinite volume survey it holds true simply by the definitions of τ_{NL} and f_{NL}, regardless of the theory relating to the primordial perturbations. However since realistic surveys will always have a finite volume, a breaking of the inequality could occur. It remains unclear how one should interpret a breaking of the inequality, and whether any concrete scenarios can be constructed in which this would occur. A violation may be related to a breaking of statistical homogeneity [Smith et al., 2011a].

violation of SY-inequality

After a brief summary of cosmology and structure formation in Sect. 7.2 we introduce primordial non-Gaussianities in Sect. 7.3 along with the SY-inequality relating the relative non-Gaussianity strengths in the polyspectra of different order. The mapping of non-Gaussianities by weak gravitational lensing is summarized in Sect. 7.4. Then, we investigate the attainable signal to noise-ratios (Sect. 7.5), address degeneracies in the measurement of g_{NL} and τ_{NL} in (Sect. 7.6), carry out statistical tests of the SY-inequality (Sect. 7.7) and investigate analytical distributions of rations of non-Gaussianity parameters (Sect. 7.8). We summarize our main results in Sect. 7.9.

The reference cosmological model used is a spatially flat wCDM cosmology with adiabatic initial perturbations for the cold dark matter. The specific parameter choices are $\Omega_m = 0.25$, $n_s = 1$, $\sigma_8 = 0.8$, $\Omega_b = 0.04$. The Hubble parameter is set to $h = 0.7$ and the Hubble-distance is given by $c/H_0 = 2996.9$ Mpc/h. The dark energy equation of state is assumed to be constant with a value of $w = -0.9$. We prefer to work with these values that differ slightly from the recent PLANCK results [Planck Collaboration et al., 2013a] because lensing prefers lower Ω_m-values and larger h-values [Heymans et al., 2013]. Scale-invariance for n_s was chosen for simplicity and should not strongly affect the conclusions as the range of angular scales probed is small and close to the normalization scale.

The fluctuations are taken to be Gaussian perturbed with weak non-Gaussianities of the local type, and for the weak lensing survey we consider the case of Euclid, with a sky coverage of $f_{sky} = 1/2$, a median redshift of 0.9, a yield of $\bar{n} = 40$ galaxies/arcmin^2 and a ellipticity shape noise of $\sigma_\epsilon = 0.3$ [Amara and Réfrégier, 2007; Refregier, 2009].

7.2 COSMOLOGY AND STRUCTURE FORMATION

In spatially flat dark energy cosmologies with the matter density parameter Ω_m, the Hubble function $H(a) = d\ln a/dt$ is given by

$$\frac{H^2(a)}{H_0^2} = \frac{\Omega_m}{a^3} + \frac{1-\Omega_m}{a^{3(1+w)}}, \tag{7.1}$$

for a constant dark energy equation of state-parameter w. Comoving distance χ and scale factor a are related by

$$\chi = c\int_a^1 \frac{da}{a^2 H(a)}, \tag{7.2}$$

given in units of the Hubble distance $\chi_H = c/H_0$. For the linear matter power spectrum $P(k)$ which describes the Gaussian fluctuation properties of the linearly evolving density field δ,

$$\langle\delta(\mathbf{k})\delta(\mathbf{k}')\rangle = (2\pi)^3\delta_D(\mathbf{k}+\mathbf{k}')P(k) \tag{7.3}$$

the ansatz $P(k) \propto k^{n_s} T^2(k)$ is chosen with the transfer function $T(k)$, which is well approximated by the fitting formula

$$\begin{aligned} T(q) &= \frac{\ln(1+2.34q)}{2.34q} \times \left[1 + 3.89q + (16.1q)^2 + (5.46q)^3 \right. \\ &+ \left. (6.71q)^4\right]^{-1/4}, \end{aligned} \tag{7.4}$$

for low-matter density cosmologies [Bardeen et al., 1986]. The wave vector $k = q\Gamma$ enters rescaled by the shape parameter Γ [Sugiyama, 1995],

$$\Gamma = \Omega_m h \exp\left[-\Omega_b\left(1 + \frac{\sqrt{2h}}{\Omega_m}\right)\right]. \tag{7.5}$$

The fluctuation amplitude is normalized to the variance σ_8^2,

$$\sigma_R^2 = \int \frac{k^2 dk}{2\pi^2} W_R^2(k)\, P(k), \tag{7.6}$$

with a Fourier-transformed spherical top-hat $W_R(k) = 3j_1(kR)/(kR)$ as the filter function operating at $R = 8$ Mpc/h. $j_\ell(x)$ denotes the spherical Bessel function of the first kind of order ℓ [Abramowitz and Stegun, 1972]. The linear growth of the density field, $\delta(\mathbf{x}, a) = D_+(a)\delta(\mathbf{x}, a = 1)$, is described by the growth function $D_+(a)$, which is the solution to the growth equation [Turner and White, 1997; Wang and Steinhardt, 1998; Linder and Jenkins, 2003],

$$\frac{d^2}{da^2}D_+(a) + \frac{1}{a}\left(3 + \frac{d\ln H}{d\ln a}\right)\frac{d}{da}D_+(a) = \frac{3}{2a^2}\Omega_m(a)D_+(a). \tag{7.7}$$

From the CDM-spectrum of the density perturbation the spectrum of the Newtonian gravitational potential can be obtained

$$P_\Phi(k) = \left(\frac{3\Omega_m}{2\chi_H^2}\right)^2 k^{n_s-4}\, T(k)^2 \tag{7.8}$$

by application of the Poisson-equation which reads $\Delta\Phi = 3\Omega_m/(2\chi_H^2)\delta$ in comoving coordinates at the current epoch, $a = 1$.

7.3 NON-GAUSSIANITIES

inflationary paradigm

Inflation has been a very successful paradigm for understanding the origin of the perturbations we observe in different observational channels today. It explains in a very sophisticated way how the universe was smoothed during a quasi-de Sitter expansion while allowing quantum fluctuations to grow and become classical on superhorizon scales. In its simplest implementation, inflation generically predicts almost Gaussian density perturbations close to scale-invariance. In the most basic models of inflation fluctuations originate from a single *origin of n-G*

scalar field in approximate slow roll and deviations from the ideal Gaussian statistics is caused by deviations from the slow-roll conditions. Hence, a detection of non-Gaussianity would be indicative of the shape of the inflaton potential or would imply a more elaborate inflationary model. Although there is consensus that competitive constraints on the non-Gaussianity parameters will emerge from CMB-observations and the next generation of large-scale structure experiments, non-Gaussianities beyond the trispectrum will remain difficult if not impossible to measure. For that reason, we focus on the extraction of bi- and trispectra from lensing data and investigate constraints on their relative magnitude. Furthermore, we will only consider local non-Gaussianities that would follow from a single-field inflation model.

local ansatz

Local non-Gaussianities are described as quadratic and cubic perturbations of the Gaussian potential $\Phi_G(\mathbf{x})$ at a fixed point $\mathbf{x}$, which yields the resulting field $\Phi(\mathbf{x})$ [LoVerde and Smith, 2011],

$$\begin{aligned}\Phi_G(\mathbf{x}) \to \Phi(\mathbf{x}) &= \Phi_G(\mathbf{x}) + f_{NL}\left(\Phi_G^2(\mathbf{x}) - \langle\Phi_G^2\rangle\right)\\ &+ g_{NL}\left(\Phi_G^3(\mathbf{x}) - 3\langle\Phi_G^2\rangle\Phi_G(\mathbf{x})\right),\end{aligned} \tag{7.9}$$

bispectrum

with the parameters f_{NL}, g_{NL} and τ_{NL}. These perturbations generate in Fourier-space a bispectrum $\langle\Phi(\mathbf{k}_1)\Phi(\mathbf{k}_2)\Phi(\mathbf{k}_3)\rangle = (2\pi)^3\delta_D(\mathbf{k}_1 + \mathbf{k}_2 + \mathbf{k}_3)\, B_\Phi(\mathbf{k}_1, \mathbf{k}_2, \mathbf{k}_3)$,

$$\begin{aligned}B_\Phi(\mathbf{k}_1, \mathbf{k}_2, \mathbf{k}_3) &= \left(\frac{3\Omega_m}{2\chi_H^2}\right)^3 2f_{NL}\,\left((k_1k_2)^{n_s-4} + 2\text{ perm.}\right)\\ &\cdot\ T(k_1)T(k_2)T(k_3),\end{aligned} \tag{7.10}$$

trispectrum

and a trispectrum $\langle\Phi(\mathbf{k}_1)\Phi(\mathbf{k}_2)\Phi(\mathbf{k}_3)\Phi(\mathbf{k}_4)\rangle = (2\pi)^3\delta_D(\mathbf{k}_1 + \mathbf{k}_2 + \mathbf{k}_3 + \mathbf{k}_4)\, T_\Phi(\mathbf{k}_1, \mathbf{k}_2, \mathbf{k}_3, \mathbf{k}_4)$,

$$\begin{aligned}T_\Phi(\mathbf{k}_1, \mathbf{k}_2, \mathbf{k}_3, \mathbf{k}_4) &= \left(\frac{3\Omega_m}{2\chi_H^2}\right)^4 \left[6g_{NL}\left((k_1k_2k_3)^{n_s-4} + 3\text{ perm.}\right)\right.\\ &+ \frac{25}{9}\tau_{NL}\left(k_1^{n_s-4}k_3^{n_s-4}\,|\mathbf{k}_1 + \mathbf{k}_2|^{n_s-4}\right.\\ &+ \left.\left.11\text{ perm.}\right)\right] T(k_1)T(k_2)T(k_3)T(k_4).\end{aligned} \tag{7.11}$$

The normalization of each mode $\Phi(\mathbf{k})$ is derived from the variance σ_8^2 of the CDM-spectrum $P(k)$.

Calculating the 4-point function of (7.9) one would find the coefficient $(2f_{NL})^2$ instead of the factor $25\tau_{NL}/9$ in eqn. (7.11) [see Byrnes et al., 2006]. Since eqn. (7.9) represents single-source local non-Gaussianity (all of the higher order terms are fully correlated with the linear term), this implies the single-source consistency relation $\tau_{NL} = (6f_{NL}/5)^2$. The factor of 25/9 in eqn. (7.11) is due to the conventional definition of τ_{NL} in terms of the curvature perturbation ζ, related by $\zeta = 5\Phi/3$. In more general models with multiple fields contributing to Φ, the equality between the two non-linearity parameters is replaced by the Suyama-Yamaguchi inequality $\tau_{NL} \geqslant (6f_{NL}/5)^2$.

single source: equality

multi source: inequality

7.4 WEAK GRAVITATIONAL LENSING

7.4.1 *Weak lensing potential and convergence*

Weak gravitational lensing probes the tidal gravitational fields of the cosmic large-scale structure by the distortion of light bundles [for reviews, please refer to Bartelmann and Schneider, 2001; Bartelmann, 2010c]. This distortion is measured by the correlated deformation of galaxy ellipticities. The projected lensing potential ψ, from which the distortion modes can be obtained by double differentiation,

lensing potential

$$\psi = 2\int d\chi\, W_\psi(\chi)\Phi \tag{7.12}$$

is related to the gravitational potential Φ by projection with the weighting function $W_\psi(\chi)$,

$$W_\psi(\chi) = \frac{D_+(a)}{a}\frac{G(\chi)}{\chi}. \tag{7.13}$$

The distribution of the lensed galaxies in redshift is incorporated in the function $G(\chi)$,

$$G(\chi) = \int_\chi^{\chi_H} d\chi'\, p(\chi')\frac{dz}{d\chi'}\left(1 - \frac{\chi}{\chi'}\right) \tag{7.14}$$

with $dz/d\chi' = H(\chi')/c$. It is common in the literature to use the parameterization

$$p(z)dz = p_0\left(\frac{z}{z_0}\right)^2 \exp\left(-\left(\frac{z}{z_0}\right)^\beta\right) dz \tag{7.15}$$

with

$$\frac{1}{p_0} = \frac{z_0}{\beta}\Gamma\left(\frac{3}{\beta}\right). \tag{7.16}$$

Because of the linearity of the observables following from eqn. (7.12) moments of the gravtational potential are mapped onto the same moments of the observable with no mixing taking place. At this point we would like to emphasis that the non-Gaussianity in the weak lensing signal is diluted by the line of sight integration, which, according to the central limit theorem, adds up a large number of non-Gaussian values for the gravitational potential with the consequence that the integrated lensing potential contains weaker non-Gaussianities [Jeong et al., 2011].

central limit theorem

7.4.2 *Convergence polyspectra*

Application of the Limber-equation and repeated substitution of $\kappa = \ell^2\psi/2$ allows the derivation of the convergence spectrum $C_\kappa(\ell)$ from

convergence spectrum

the spectrum $P_\Phi(k)$ of the gravitational potential,

$$C_\kappa(\ell) = \ell^4 \int_0^{\chi_H} \frac{d\chi}{\chi^2} W_\psi^2(\chi) P_\Phi(k), \tag{7.17}$$

bispectrum

of the the convergence bispectrum $B_\kappa(\boldsymbol{\ell}_1, \boldsymbol{\ell}_2, \boldsymbol{\ell}_3)$,

$$B_\kappa(\boldsymbol{\ell}_1, \boldsymbol{\ell}_2, \boldsymbol{\ell}_3) = (\ell_1 \ell_2 \ell_3)^2 \int_0^{\chi_H} \frac{d\chi}{\chi^4} W_\psi^3(\chi) B_\Phi(\mathbf{k}_1, \mathbf{k}_2, \mathbf{k}_3) \tag{7.18}$$

and trispectrum

and of the convergence trispectrum $T_\kappa(\boldsymbol{\ell}_1, \boldsymbol{\ell}_2, \boldsymbol{\ell}_3, \boldsymbol{\ell}_4)$,

$$T_\kappa(\boldsymbol{\ell}_1, \boldsymbol{\ell}_2, \boldsymbol{\ell}_3, \boldsymbol{\ell}_4) = (\ell_1 \ell_2 \ell_3 \ell_4)^2 \int_0^{\chi_H} \frac{d\chi}{\chi^6} W_\psi^4(\chi) T_\Phi(\mathbf{k}_1, \mathbf{k}_2, \mathbf{k}_3, \mathbf{k}_4). \tag{7.19}$$

This relation follows from the expansion of the tensor $\boldsymbol{\psi} = \partial^2\psi/\partial\theta_i\partial\theta_j$ into the basis of all symmetric 2×2-matrices provided by the Pauli matrices σ_α [Abramowitz and Stegun, 1972]. In particular, the lensing convergence is given by $\kappa = \mathrm{tr}(\boldsymbol{\psi}\sigma_0)/2 = \Delta\psi/2$ with the unit matrix σ_0. Although the actual observable in lensing are the weak shear components $\gamma_+ = \mathrm{tr}(\boldsymbol{\psi}\sigma_1)/2$ and $\gamma_\times = \mathrm{tr}(\boldsymbol{\psi}\sigma_3)/2$, we present all calculations in terms of the convergence, which has identical statistical properties and being scalar, is easier to work with.

Fig. 7.1 shows the weak lensing spectrum and the non-Gaussian bi- and trispectra as a function of multipole order ℓ. For the bispectrum we choose an equilateral configuration and for the trispectrum a square one. The polyspectra are multiplied with factors of $(\ell)^{2n}$ for making them dimensionless and in that way we were able to show all spectra in a single plot, providing a better physical interpretation of variance, skewness and kurtosis per logarithmic ℓ-interval. In our derivation we derive the lensing potential directly from the gravitational potential, in which the polyspectra are expressed and subsequently apply ℓ^2-prefactors to obtain the polyspectra in terms of the weak lensing convergence, for which the covariance and the noise of the measurement is most conveniently expressed. The disadvantage of this method is that the τ_NL-part of the trispectrum T_ψ diverges for the square configuration, because opposite sides of the square cancel in the $|\mathbf{k}_i - \mathbf{k}_{i+2}|$-terms which can not be exponentiated with a negative number $n_s - 4$. We control this by never letting the cosine of the angle between $\mathbf{k}_i$ and $\mathbf{k}_{i+2}$ drop below -0.95. We verified that this exclusion cone of size $\simeq 20°$ has a minor influence on the computation of signal to noise-ratios.

The contributions to the weak lensing polyspectra as a function of comoving distance χ are shown in Fig. 7.2, which is the derivative of Fig. 7.1 at fixed ℓ. At the same time, the plot presents the integrand of the Limber equation and it demonstrates nicely that the largest contribution to the weak lensing polyspectra comes from the peak of the galaxy distribution, with small variations with multipole order as higher multipoles acquire contributions from slightly lower distances.

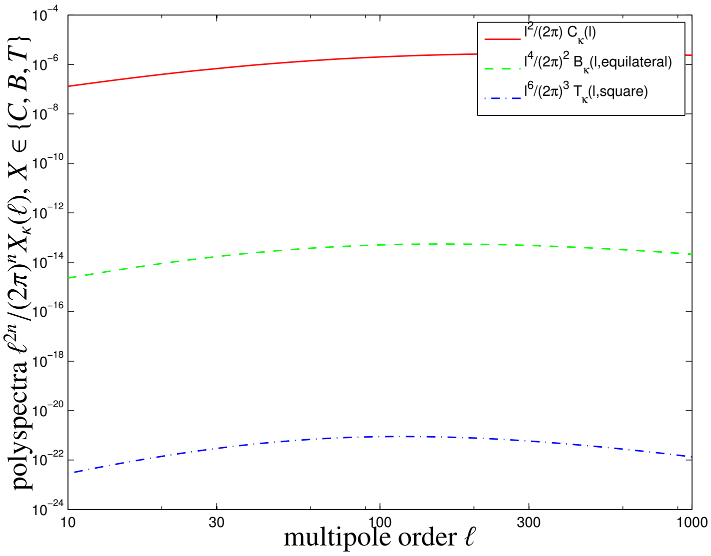

Figure 7.1: The weak convergence spectrum $C_\kappa(\ell)$ (red solid line), the weak convergence bispectrum $B_\kappa(\ell)$ for an equilateral configuration (green solid line) with $f_{NL} = 1$, and the convergence trispectrum $T_\kappa(\ell)$ for a square configuration as a function of multipole order ℓ, for $g_{NL} = 1$ (blue dashed line).

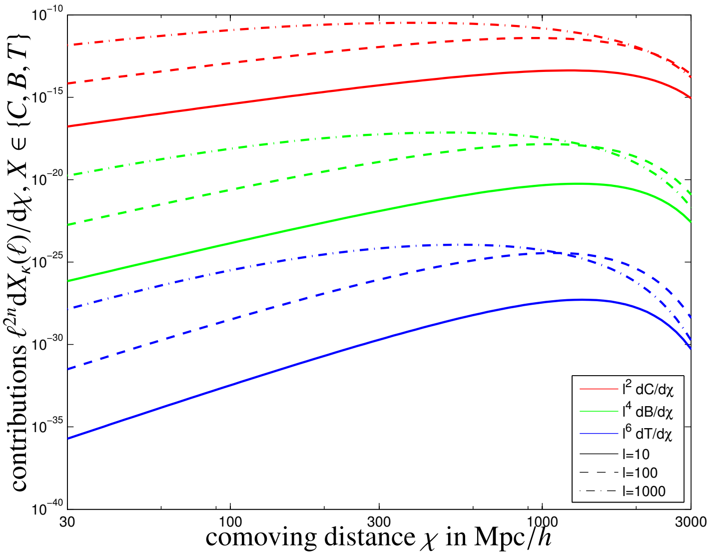

Figure 7.2: Contributions $dC_\kappa(\ell)/d\chi$ (red lines), $dB_\kappa(\ell)/d\chi$ (green lines) for the equilateral configuration and $dT_\kappa(\ell)/d\chi$ (blue lines) for the square configuration, as a function of comoving distance χ. The non-Gaussianity parameters are chosen to be $f_{NL} = 1$ and $g_{NL} = 1$. We compare the contributions at $\ell = 10$ (solid line) with $\ell = 100$ (dashed line) and $\ell = 1000$ (dash-dotted line).

7.4.3 *Relative magnitudes of weak lensing polyspectra*

The strength of the non-Gaussianity introduced by nonzero values of g_{NL} and τ_{NL} can be quantified by taking ratios of the three polyspectra. We define the skewness parameter $S(\ell)$ as the ratio

skewness

$$S(\ell) = \frac{B_\kappa(\ell)}{C_\kappa(\ell)^{3/2}} \tag{7.20}$$

between the convergence bispectra for the equilateral configuration and the convergence spectrum. In analogy, we define the kurtosis parameter $K(\ell)$,

kurtosis

$$K(\ell) = \frac{T_\kappa(\ell)}{C_\kappa(\ell)^2}, \tag{7.21}$$

as the ratio between the convergence trispectrum for the square configuration and the spectrum as a way of quantifying the size of the non-Gaussianity. The relative magnitude of the bi- and trispectrum is given by the function $Q(\ell)$,

$$Q(\ell) = \frac{T_\kappa(\ell)}{B_\kappa(\ell)^{4/3}}. \tag{7.22}$$

For computing the three parameters we set the non-Gaussianity parameters to $f_{NL} = g_{NL} = 1$.

The parameters are shown in Fig. 7.3 as a function of multipole order ℓ. They have been constructed such that the transfer function $T(k)$ in each of the polyspectra is cancelled. The parameters are power-laws because the inflationary part of the spectrum k^{n_s-4} is scale-free and the Wick theorem reduces the polyspectra to products of that inflationary spectrum. The amplitude of the parameters reflects the proportionality of the polyspectra to $3\Omega_m/(2\chi_H^2)$ and the normalization of each mode proportional to σ_8. A noticeable outcome in the plot is the fact that the ratio is largest on large scales as anticipated. Since the fluctuations in the inflationary fields give rise to fluctuations in the gravitational potential on which the perturbation theory is built. Since the effect of the potential is on large scale and the trispectrum is proportional to the spectrum taken to the third power, the ratio $K(\ell)$ should be the largest on large scales. Therefore as one can see in the Fig. 7.3 the ratio is drops to very small numbers on small scales. Similar arguments apply to $Q(\ell)$ and $S(\ell)$.

power-laws

7.5 SIGNAL TO NOISE-RATIOS

The signal strength at which a given polyspectrum can be measured is computed as the ratio between that particular polyspectrum and the variance of its estimator averaged over a Gaussian ensemble [which, in the case of structure formation non-Gaussianities, has been shown

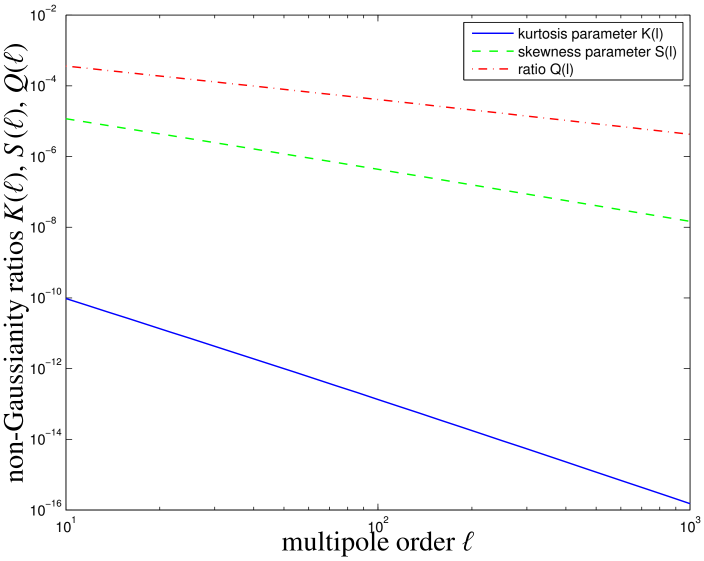

Figure 7.3: Parameters $K(\ell)$ (blue solid line), $S(\ell)$ (green dashed line) and $Q(\ell)$ (red dash-dotted line), where we chose a equilateral configuration for the convergence bispectrum and a square configuration for the trispectrum. The non-Gaussianity parameters are $f_{NL} = 1$ and $g_{NL} = 1$

to be a serious limitation Takada and Jain, 2009; Sato and Nishimichi, 2013; Kayo et al., 2013]. We work in the flat-sky approximation because the treatment of the bi- and trispectra involves a configuration-space average, which requires the evaluation of Wigner-symbols in multipole space.

flat-sky

In the flat-sky approximation the signal to noise ratio Σ_C of the weak convergence spectrum $C_\kappa(\ell)$ reads [Tegmark et al., 1997; Cooray and Hu, 2001]

spectrum signal-to-noise ratio

$$\Sigma_C^2 = \int \frac{d^2\ell}{(2\pi)^2} \frac{C_\kappa(\ell)^2}{\mathrm{cov}_C(\ell)}, \tag{7.23}$$

with the Gaussian expression for the covariance $\mathrm{cov}_C(\ell)$ [Hu and White, 2001; Takada and Hu, 2013],

$$\mathrm{cov}_C(\ell) = 2 \times 2\pi\, f_{sky}\, \tilde{C}_\kappa(\ell)^2. \tag{7.24}$$

Likewise, the signal to noise ratio Σ_B of the bispectrum $B_\kappa(\ell)$ is given by [Hu, 2000; Takada and Jain, 2004; Babich, 2005; Joachimi et al., 2009]

bispectrum signal-to-noise ratio

$$\Sigma_B^2 = \int \frac{d^2\ell_1}{(2\pi)^2} \int \frac{d^2\ell_2}{(2\pi)^2} \int \frac{d^2\ell_3}{(2\pi)^2} \frac{B_\kappa^2(\ell_1,\ell_2,\ell_3)}{\mathrm{cov}_B(\ell_1,\ell_2,\ell_3)} \tag{7.25}$$

where the covariance $\mathrm{cov}_B(\ell_1,\ell_2,\ell_3)$ follows from

$$\mathrm{cov}_B(\ell_1,\ell_2,\ell_3) = f_{sky}(2\pi)^3\, \tilde{C}_\kappa(\ell_1)\tilde{C}_\kappa(\ell_2)\tilde{C}_\kappa(\ell_2). \tag{7.26}$$

trispectrum signal-to-noise ratio

Finally, the signal to noise ratio Σ_T of the convergence trispectrum T_κ results from [Zaldarriaga, 2000; Hu, 2001; Kamionkowski et al., 2011]

$$\Sigma_T^2 = \int \frac{d^2\ell_1}{(2\pi)^2} \int \frac{d^2\ell_2}{(2\pi)^2} \int \frac{d^2\ell_3}{(2\pi)^2} \int \frac{d^2\ell_4}{(2\pi)^2} \frac{T_\kappa^2(\boldsymbol{\ell}_1, \boldsymbol{\ell}_2, \boldsymbol{\ell}_3, \boldsymbol{\ell}_4)}{\mathrm{cov}_T(\ell_1, \ell_2, \ell_3, \ell_4)}, \quad (7.27)$$

with the expression

$$\mathrm{cov}_T(\ell_1, \ell_2, \ell_3, \ell_4) = f_{\mathrm{sky}}(2\pi)^4 \tilde{C}_\kappa(\ell_1)\tilde{C}_\kappa(\ell_2)\tilde{C}_\kappa(\ell_3)\tilde{C}_\kappa(\ell_4) \quad (7.28)$$

for the trispectrum covariance $\mathrm{cov}_T(\ell_1, \ell_2, \ell_3, \ell_4)$. In all covariances, the fluctuations of the weak lensing signal and the noise are taken to be Gaussian and are therefore described by the noisy convergence spectrum $\tilde{C}_\kappa(\ell)$,

$$\tilde{C}_\kappa(\ell) = C_\kappa(\ell) + \frac{\sigma_\epsilon^2}{\bar{n}}, \quad (7.29)$$

with the number of galaxies per steradian $\bar{n}$ and the ellipticity noise σ_ϵ.

Monte Carlo integration: CUBA

The configuration space integrations for estimating the signal to noise ratios as well as for computing Fisher-matrices are carried out in polar coordinates with a Monte-Carlo integration scheme [specifically, with the CUBA-library by Hahn, 2005, who provides a range of adaptive Monte-Carlo integration algorithms]. We obtained the best results with the SUAVE-algorithm that uses importance sampling for estimating the values of the integrals.

Fig. 7.4 provides a plot of the polyspectra in units of the noise of their respective estimators. Clearly, the measurements are dominated by cosmic variance and show the according Poissonian dependence with multipole ℓ, before the galaxy shape noise limits the measurement on small sacles and the curves level off or, in the case of the higher polyspectra, begin to drop on multipoles $\ell \lesssim 300$.

minimum values for detection

An observation of the polyspectra $C_\kappa(\ell)$, B_κ and T_κ with Euclid would yield signal to noise ratios as depicted in Fig. 7.5. Whereas the convergence spectrum $C_\kappa(\ell)$ can be detected with high significance in integrating over the multipole range up to $\ell = 10^3$, the bispectrum would require f_{NL} to be of the order 10^2 and the two trispectrum non-Gaussianities g_{NL} and τ_{NL}-values of the order 10^6 for yielding a detection, which of course is weaker compared to CMB bounds or bounds on the parameters from large-scale structure observation. The reason lies in the non-Gaussianity supression due to the central-limit theorem in the line of sight-integration [Jeong et al., 2011]. This could in principle be compensated by resorting to tomographic weak lensing (see Sect. 7.9).

7.6 DEGENERACIES IN THE TRISPECTRUM

independency between g_{NL} and τ_{NL}

The independency of estimates of g_{NL} and τ_{NL} from the weak lensing

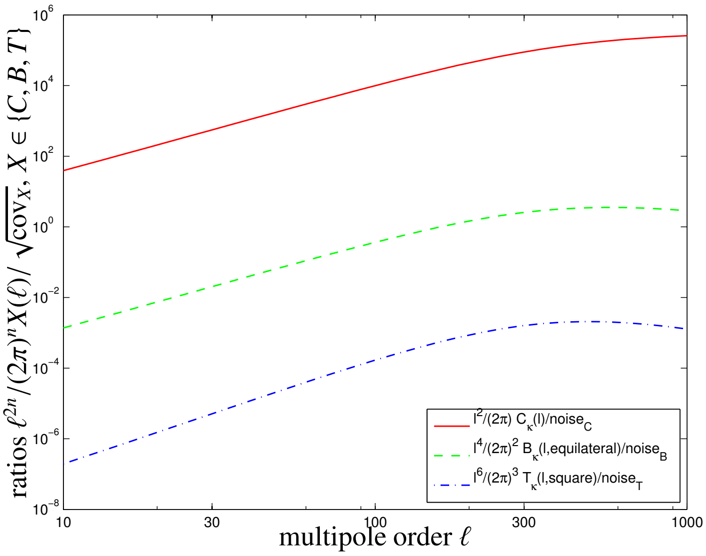

Figure 7.4: Noise-weighted weak lensing polyspectra: $C_\kappa(\ell)/\sqrt{\mathrm{cov}_C}$ (red solid line), $B_\kappa(\ell)/\sqrt{\mathrm{cov}_B}$ for the equilateral configuration (green dashed line) and $T_\kappa(\ell)/\sqrt{\mathrm{cov}_T}$ (blue dash-dotted line) for the square configuration. The non-Gaussianity parameters are $f_{NL} = 1$ and $g_{NL} = 1$

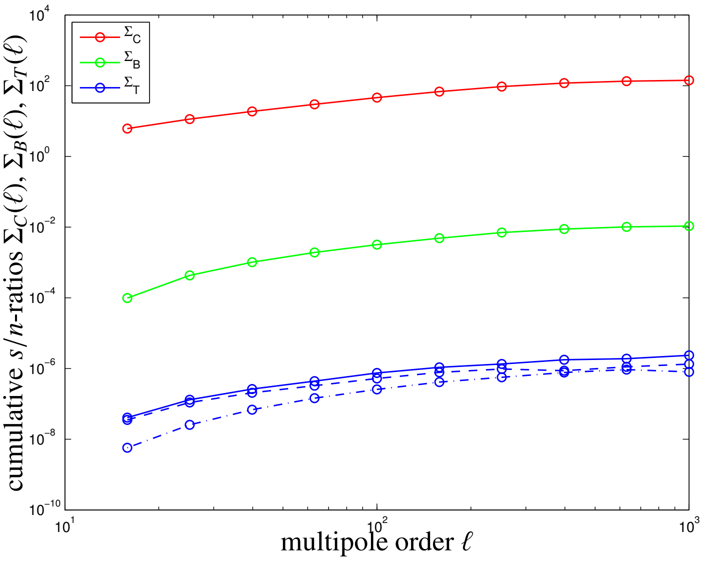

Figure 7.5: Cumulative signal to noise-ratios Σ_C for the weak lensing spectrum (red solid line), Σ_B for the weak lensing bispectrum (green solid line) and Σ_T for the weak lensing trispectrum, for $(\tau_{NL}, g_{NL}) = (1, 1)$ (blue solid line), $(\tau_{NL}, g_{NL}) = (1, 0)$ (blue dashed line) and $(\tau_{NL}, g_{NL}) = (0, 1)$ (blue dash-dotted line).

trispectrum are depicted in Fig. 7.6 where we plot the likelihood contours in the g_{NL}-τ_{NL}-plane. The likelihood $\mathcal{L}(f_{NL}, g_{NL}, \tau_{NL})$ is taken to be Gaussian,

$$\mathcal{L}(f_{NL}, g_{NL}, \tau_{NL}) = \sqrt{\frac{\det(F)}{(2\pi)^3}} \exp\left[-\frac{1}{2}\begin{pmatrix} f_{NL} \\ g_{NL} \\ \tau_{NL}\end{pmatrix}^T F \begin{pmatrix} f_{NL} \\ g_{NL} \\ \tau_{NL}\end{pmatrix}\right] \quad (7.30)$$

which can be expected due to the linearity of the polyspectra with the non-Gaussianity parameters. The Fisher-matrix F has been estimated for a purely Gaussian reference model and with a Gaussian covariance, and its entries can be computed in analogy to the signal to noise ratios. The diagonal of the Fisher matrix is composed from the values Σ_B and Σ_T with the non-Gaussianity parameters set to unity, and the only off-diagonal elements are the two entries $F_{g_{NL}\tau_{NL}}$,

$$\begin{aligned} F_{g_{NL}\tau_{NL}} &= \int\frac{d^2\ell_1}{(2\pi)^2}\int\frac{d^2\ell_2}{(2\pi)^2}\int\frac{d^2\ell_3}{(2\pi)^2}\int\frac{d^2\ell_4}{(2\pi)^2}\frac{1}{\mathrm{cov}_T(\ell_1,\ell_2,\ell_3,\ell_4)} \\ &\cdot \quad T_\kappa(g_{NL}=1,\tau_{NL}=0)T_\kappa(g_{NL}=0,\tau_{NL}=1), \end{aligned} \quad (7.31)$$

which again is solved by Monte-Carlo integration in polar coordinates. The statistical errors on f_{NL} on one side and g_{NL} and τ_{NL} on the other are independent. Clearly, there is a degeneracy that g_{NL} can be increased at the expense of τ_{NL} and vice versa. In the remainder of the paper, we carry out a marginalization of the Fisher-matrix such that the uncertainty in g_{NL} is contained in τ_{NL}. The overall precision that can be reached with lensing is about an order of magnitude worse compared to the CMB [Smidt et al., 2010], with a very similar orientation of the degeneracy.

marginalization

7.7 TESTING THE SUYAMA-YAMAGUCHI-INEQUALITY

Given the fact that there are a vast of different inflationary models generating similar local-type non-Gaussianity, it is indispensable to have a classification of these different models into some categories. This can be for instance achieved by using consistency relations among the non-Gaussianity parameters as the SY-relation. In the literature one distinguishes between three main categories of models, the single-source model, the multi-source model and constrained multi-source model. As the name already reveals the single-source model is a model of one field causing the non-linearities. The important representatives of this category include the pure curvaton and the pure modulated reheating scenarios. It is also possible that multiple sources are simultaneously responsible for the origin of density fluctuations. It could be for instance that both the inflaton and the curvaton fields are generating the non-linearities we observe today. In the case of multi-source models the relations between the non-linearity parameters are different from those for the single-source models. Finally, the

single-source models

multi-source models

constrained multi-source models

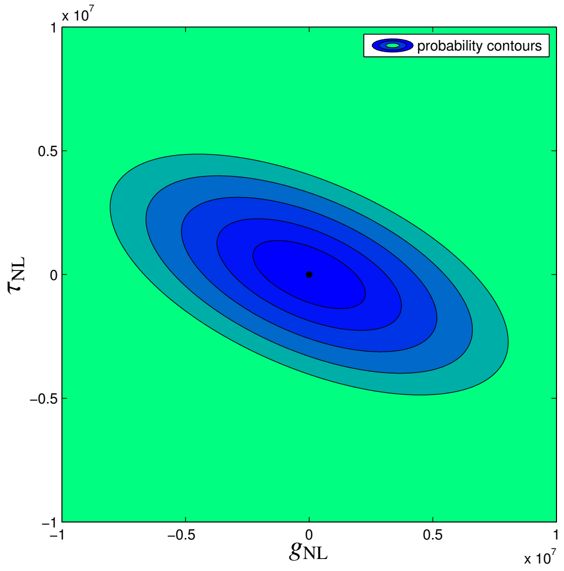

Figure 7.6: Degeneracies in the g_{NL}-τ_{NL}-plane for a measurement with Euclid: The $1\sigma \ldots 4\sigma$-contours of the joint likelihood are drawn, while all cosmological parameters are assumed to be known exactly.

constrained multi-source models are models in which the loop contributions in the expressions for the power spectrum and non-linearity parameters are not neglected. The classification into these three categories was based on the relation between f_{NL} and τ_{NL}. Nevertheless, this will not be enough to discriminate between the models of each category. For this purpose, we will need further relations between f_{NL} and g_{NL}. Hereby, the models are distinguished by rather if g_{NL} is proportional to f_{NL} ($f_{\mathrm{NL}} \sim g_{\mathrm{NL}}$) or enhanced or suppressed compared to f_{NL}. Summarizing, the f_{NL}-τ_{NL} and f_{NL}-g_{NL} relations will be powerful tools to discriminate models well. In this work we are focusing on the SY-relation between f_{NL} and τ_{NL}. The Bayesian evidence [for reviews, see Trotta, 2007, 2008] for the SY-relation $\tau_{\mathrm{NL}} \geqslant (6/5 f_{\mathrm{NL}})^2$ can be expressed as the fraction α of the likelihood $\mathcal{L}$ that provides support:

f_{NL}-τ_{NL} *and* f_{NL}-g_{NL} *relations*

$$\alpha = \int_{\tau_{\mathrm{NL}} \geqslant (6/5 f_{\mathrm{NL}})^2} \mathrm{d}\tau'_{\mathrm{NL}} \int \mathrm{d}f'_{\mathrm{NL}}\, \mathcal{L}\left(f_{\mathrm{NL}} - f'_{\mathrm{NL}}, \tau_{\mathrm{NL}} - \tau'_{\mathrm{NL}}\right). \qquad (7.32)$$

Hence α answers the question as to how likely one would believe in the SY-inequality with inferred f'_{NL} and τ'_{NL}-values if the true values are given by f_{NL} and τ_{NL}. Technically, α corresponds to the integral over the likelihood in the f_{NL}-τ_{NL}-plane over the allowed region. If $\alpha = 1$, we would fully believe in the SY-inequality, if $\alpha = 0$ we would think that the SY-relation would be violated. Correspondingly, $1-\alpha$ would provide a quantification of the violation of the SY-relation,

$$1-\alpha = \int\limits_{\tau_{NL}<(6/5f_{NL})^2} d\tau'_{NL} \int df'_{NL}\, \mathcal{L}\left(f_{NL}-f'_{NL}, \tau_{NL}-\tau'_{NL}\right). \quad (7.33)$$

We can formulate the integration over the allowed region as well as an integration over the full f_{NL}-τ_{NL}-range of the likelihood multiplied with a suitable function Π,

$$\alpha = \int d\tau'_{NL} \int df'_{NL}\, \mathcal{L}(f_{NL}-f'_{NL}, \tau_{NL}-\tau'_{NL}) \times \Pi(f_{NL}, \tau_{NL}) \quad (7.34)$$

degree of belief

with $\Pi = \theta(\tau_{NL}-(6/5f_{NL})^2)$. This function would play the role of a theoretical prior in the f_{NL}-τ_{NL}-plane. In this interpretation, α corresponds to the Bayesian evidence, that means the degree of belief that the SY-inequality is correct.

We can test the SY-inequality $\tau_{NL} \geqslant (6/5f_{NL})^2$ up to the errors on f_{NL} and τ_{NL} provided by the lensing measurement: Fig. 7.7 shows the test statistic $\alpha(f_{NL}, g_{NL}, \tau_{NL})$ in the f_{NL}-τ_{NL}-plane, where the likelihood has been marginalized over the parameter g_{NL}. The blue regime $f_{NL} \gtrsim 10^2$ is the parameter space which would not fulfill the SY-inequality, whereas the green area $\tau_{NL} \gtrsim 10^5$ is the parameter space that where the SY-relation would be fulfilled. Values of $f_{NL} \lesssim 10^2$ and $\tau_{NL} \lesssim 10^5$ are inconclusive and even though non-Gaussianity parameters may be inferred that would be in violation of the SY-relation, the wide likelihood would not allow to derive a statement. Another nice feature is the fact that for large f_{NL} and τ_{NL} the relation can be probed to larger precision and the contours are more closely spaced.

7.8 ANALYTICAL DISTRIBUTIONS

exactly fulfilled relation

In this section we would like to derive the analytical expression for the probability density that the SY-relation is exactly fulfilled, $\tau_{NL} = (6/5f_{NL})^2$, i.e. for the case $(6/5f_{NL})^2/\tau_{NL} \equiv 1$. For this purpose we explore the properties of the distribution

$$p(Q)dQ \quad \text{with} \quad Q = \frac{(6/5f_{NL})^2}{\tau_{NL}} \quad (7.35)$$

where the parameters f_{NL} and τ_{NL} are both Gaussian distributed with means $\bar{f}_{NL}$, $\bar{\tau}_{NL}$ and widths $\sigma_{f_{NL}}$ and $\sigma_{\tau_{NL}}$.

We will split the derivation into two parts. First of all we will derive the distribution for the product f^2_{NL}. For this purpose we use the transformation of the probability density:

$$p_y(y)dy = p_x(x)dx \quad (7.36)$$

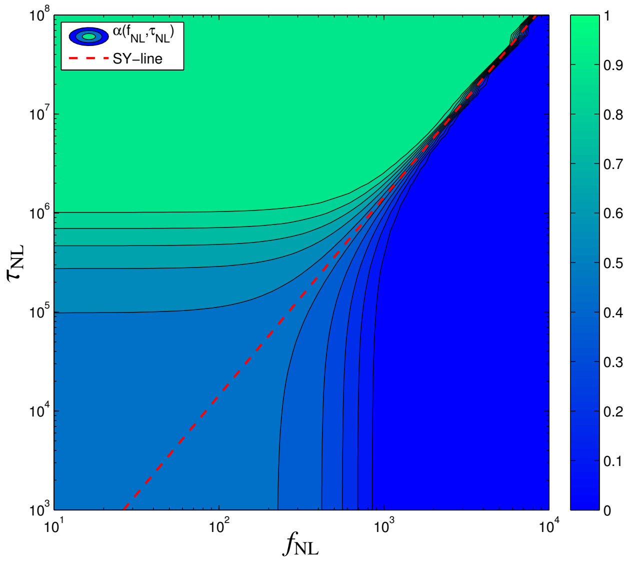

Figure 7.7: Bayesian evidence $\alpha(f_{NL}, \tau_{NL})$ in the f_{NL}-τ_{NL}-plane. Blue regions correspond to low, green regions to high degrees of belief. The SY-relation $\tau_{NL} = (6/5f_{NL})^2$ is indicated by the red dashed line.

with the Jacobian $\frac{dx}{dy} = \frac{1}{2\sqrt{y}}$ and where $x = f_{NL}$ and $y = x^2$. Thus we can write the above equality as

$$p_y(y) = \frac{p_x(\sqrt{y})}{2\sqrt{y}} \tag{7.37}$$

where the probability distribution $p_x(x)$ is given by

$$p_x(\sqrt{y}) = \frac{1}{\sqrt{2\pi\sigma^2_{f_{NL}}}} \exp\left(-\frac{(\sqrt{y} - \bar{f}_{NL})^2}{2\sigma^2_{f_{NL}}}\right) \tag{7.38}$$

Naively written in this way, we would lose half of the distribution and do not obtain the right normalization. Therefore we have to distinguish between the different signs of y. After taking care of that the distribution of a square of a Gaussian distributed variate f_{NL} with mean $\bar{f}_{NL}$ and variance $\sigma_{f_{NL}}$ is given by

$$\begin{aligned} p_y(y) &= \frac{1}{\sqrt{2\pi\sigma^2_{f_{NL}}}} \frac{1}{2\sqrt{y}} \\ &\cdot \begin{cases} \exp\left(-\frac{(\sqrt{y}-\bar{f}_{NL})^2}{2\sigma^2_{f_{NL}}}\right), & \sqrt{y} \text{ positive branch} \\ \exp\left(-\frac{(-\sqrt{-y}-\bar{f}_{NL})^2}{2\sigma^2_{f_{NL}}}\right), & \sqrt{y} \text{ negative branch} \end{cases} \end{aligned} \tag{7.39}$$

with $y = f_{\mathrm{NL}}^2$. In the special case of normally distributed variates, the above expression would reduce to

$$p_y(y) = \frac{K_0\left(\frac{|y|}{\sigma_{f_{\mathrm{NL}}}\sigma_{\tau_{\mathrm{NL}}}}\right)}{\pi\sigma_{f_{\mathrm{NL}}}\sigma_{\tau_{\mathrm{NL}}}} \tag{7.40}$$

where $K_n(y)$ is a modified Bessel function of the second kind [Abramowitz and Stegun, 1972].

The next step is now to implement the distribution eqn. (7.39) into a ratio distribution since we are interested in the distribution of

$$\left(\frac{6f_{\mathrm{NL}}}{5}\right)^2 \frac{1}{\tau_{\mathrm{NL}}}$$

incorporating the additional factor 4. The ratio distribution can be written down using the Mellin transformation [Arfken and Weber, 2005]:

$$p(Q) = \int |\alpha| d\alpha\, p_y(\alpha Q, \bar{f}_{\mathrm{NL}}) p_z(\alpha, \bar{\tau}_{\mathrm{NL}}), \tag{7.41}$$

with a Gaussian distribution for $z = \tau_{\mathrm{NL}}$,

$$p_z(z) = \frac{1}{\sqrt{2\pi\sigma_z^2}} \exp\left(-\frac{(z-\bar{z})^2}{2\sigma_z^2}\right) \tag{7.42}$$

In the special case of Gaussian distributed variates with zero mean the distribution would be simply given by the Cauchy distribution [Marsaglia, 1965, 2006], but in the general case eqn. (7.39) needs to be evaluated analytically.

In Fig. 7.8 we are illustrating the ratio distribution as a function of f_{NL} and τ_{NL} for $Q = 1$, i.e for the case where the SY-relation becomes an equality. The values for f_{NL} run from 1 to 10^3 and τ_{NL} runs from 1 to 10^6. The variances $\sigma_{f_{\mathrm{NL}}}$ and $\sigma_{\tau_{\mathrm{NL}}}$ are taken from the output of the Fisher matrix and correspond to $\sigma_{f_{\mathrm{NL}}} = 93$ and $\sigma_{\tau_{\mathrm{NL}}} = 7.5 \times 10^5$. We would like to point out the nice outcome, that the distribution has a clearly visible bumped line along the the SY-equality. Similarly, Fig. 7.9 shows a number of example distributions $p(Q)dQ$ for a choice of non-Gaussianity parameters f_{NL} and τ_{NL}. We let Q run from 1 to 5 and fix the values for f_{NL} and τ_{NL} pairwise to $(f_{\mathrm{NL}}, \tau_{\mathrm{NL}}) = (1, 1), (5, 5), (10, 10), (20, 20), \ldots, (100, 100)$ respectively.

7.9 SUMMARY

Topic of this paper is an investigation of inflationary bi- and trispectra by weak lensing, and testing of the SY-inequality relating the relative strengths of the inflationary bi- and trispectrum amplitudes using weak lensing as a mapping of the large-scale structure. Specifically, we consider the case of the projected Euclid weak lensing survey and choose a basic wCDM-cosmology as the background model.

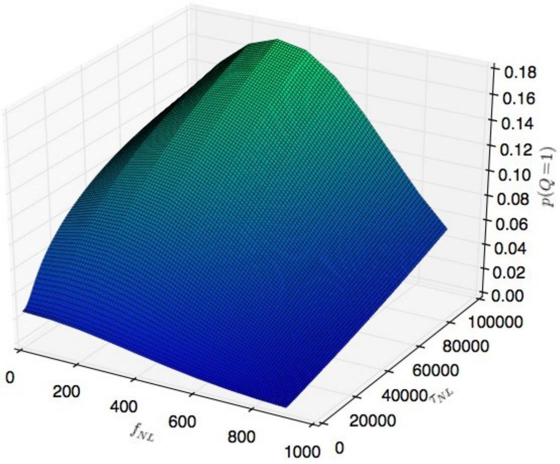

Figure 7.8: The probability distribution $p(Q)dQ$ of $Q = (6/5f_{\mathrm{NL}})^2/\tau_{\mathrm{NL}}$ as a function of the non-Gaussianity parameters f_{NL} and τ_{NL}.

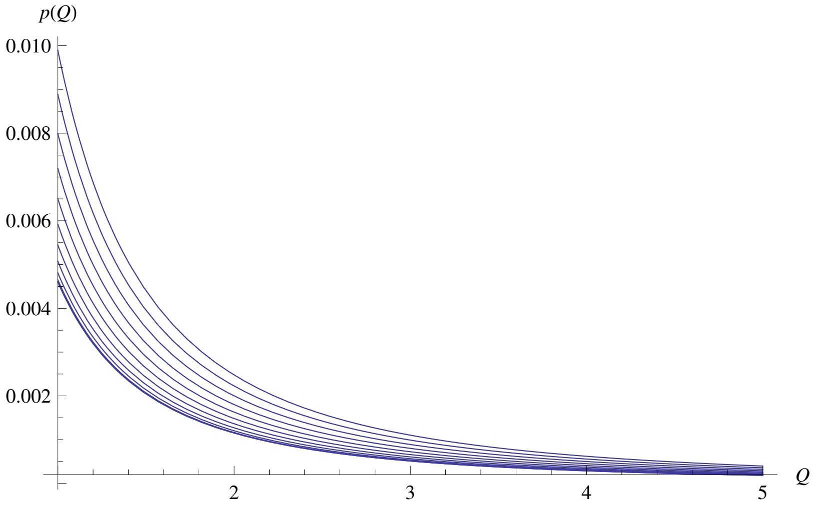

Figure 7.9: The probability distribution $p(Q)$ as a function of Q for fixed non-Gaussianity parameter f_{NL} and τ_{NL}. The curves in descending order represent $(f_{\mathrm{NL}}, \tau_{\mathrm{NL}}) = (1,1),(5,5),(10,10),(20,20),\ldots,(100,100)$.

1. We compute weak lensing potential and weak lensing convergence spectra C_κ, bispectra B_κ and trispectra T_κ by Limber-projection from the CDM-polyspectra P_Φ, B_Φ and T_Φ of the Newtonian gravitational potential Φ. The non-Gaussianity model for the higher-order spectra are local non-Gaussianities parametrised with f_{NL}, g_{NL} and τ_{NL}. The weak lensing polyspectra reflect in their magnitude the perturbative ansatz by which they are generated and collect most of their amplitude at distances of ~ 1 Gpc/h, where the higher order polyspectra show a tendency to be generated at slightly smaller distances. Ratios of polyspectra where the transfer function has been divided out, nicly illustrate the reduction to products of spectra by application of the Wick theorem, as a pure power-law behaviour is recovered by this construction.

2. The signal to noise ratios Σ_C, Σ_B and Σ_T at which the polyspectra can be estimated with Euclid's weak lensing data are forecasted using a very efficient Monte-Carlo integration scheme for carrying out the configuration space summation. These integrations are carried out in flat polar coordinates with a Gaussian expression for the signal covariance. Whereas the first simplification should influence the result only weakly as most of the signal originates from sufficiently large multipoles, the second simplification has been shown to be violated in the investigation of dominating structure formation non-Gaussianities, but might be applicable in the case of weak inflationary non-Gaussianities and on low multipoles.

3. With a very similar integration scheme we compute a Fisher-matrix for the set of non-Gaussianity parameters f_{NL}, g_{NL} and τ_{NL} such that a Gaussian likelihood $\mathcal{L}$ can be written down. Marginalization over g_{NL} yields the final likelihood $\mathcal{L}(f_{NL}, \tau_{NL})$ which is the basis of the statistical investigations concerning the SY-inequality. The diagonal elements of the Fisher matrix are simply inverse squared signal to noise ratios due to the proportionality $B_\kappa \propto f_{NL}$ and $T_\kappa \propto \tau_{NL}$. For Gaussian covariances, the parameters f_{NL} and τ_{NL} are statistically independent.

4. We quantify the degree of belief in the SY-relation with a set of infered values for f_{NL} and τ_{NL} and with statistical errors $\sigma_{f_{NL}}$ and $\sigma_{\tau_{NL}}$ by computing the Bayesian evidence that the SY-relation $\tau_{NL} \geqslant (6/5 f_{NL})^2$ is fulfilled. Euclid data would provide evidence in favour of the relation for $\tau_{NL} \gtrsim 10^5$ and against the relation if $g_{NL} \gtrsim 10^2$. For $f_{NL} < 10^2$ and $\tau_{NL} \lesssim 10^5$ the Bayesian evidence is inconclusive and quite generally, large non-Gaussianities allow for a better probing of the relation.

5. We provide a computation of the probability that the quantity $Q \equiv (6/5f_{NL})^2/\tau_{NL}$ is one, i.e. for an exact SY-relation. The distribution can be derived by generating a χ^2-distribution for f_{NL}^2 and then by Mellin-transform for the ratio f_{NL}^2/τ_{NL}. We observe, that the analytical probability distribution has a clearly visible bumped line along the SY-equality.

In summary, we would like to point out that constraining non-Gaussianities in weak lensing data is possible but the sensitivity is weaker compared to other probes. Nevertheless, for the small bispectrum parameter confirmed by PLANCK, τ_{NL} values of the order of 10^5 would be needed to claim a satisfied SY-relation, and values smaller than that would not imply a violation, given the large experimental uncertainties.

Despite the fact that we will not be able to see a violation of the inequality, if τ_{NL} is large enough to be observed, then this together with the tight observational constraints on f_{NL} will imply that the single-source relation is broken and instead $\tau_{NL} \gg f_{NL}^2$. Even though this might be allowed by inflation, such a result would come as a surprise and be of great interest, since typically even multi-source scenarios predict a result which is close to the single-source equality, and a strong breaking is hard to realise for known models, e.g. Peterson and Tegmark [2011]; Elliston et al. [2012]; Leung et al. [2013], although examples can be constructed at the expense of fine tuning [Ichikawa et al., 2008; Byrnes et al., 2009].

what about tomography?

As an outlook we provide a very coarse projection what levels of f_{NL} and τ_{NL} can be probed by tomographic surveys with $N = 2, 3, 4$ redshift bins which are chosen to contain equal fractions of the galaxy distribution [Hu, 1999; Takada and Jain, 2004]. Fig. 7.10 shows the signal to noise ratio Σ_B and Σ_T for measuring local weak lensing bi- and trispectra, respectively, and at the same time those numbers correspond to the inverse statistical errors $\sigma_{f_{NL}}$ and $\sigma_{\tau_{NL}}$ because of the proportionality $B_\kappa \propto f_{NL}$ and $T_\kappa \propto \tau_{NL}$. If the measurement is limited by statistics the constraints on the non-Gaussianity parameters could be improved substantially, up to an statistical uncertainty of $\sigma_{f_{NL}}$ of the order 10 and $\sigma_{\tau_{NL}}$ of the order 10^4 with a correspondingly tighter probing of the SY-relation, but of course many systematical effects become important, related to the measurement itself [Semboloni et al., 2011; Heymans et al., 2013], to structure formation non-Gaussianities at low redshifts [which can in principle be controlled with good priors on cosmological parameters, Schäfer et al., 2012], or to the numerics of the polyspectrum estimation [Smith et al., 2011b].

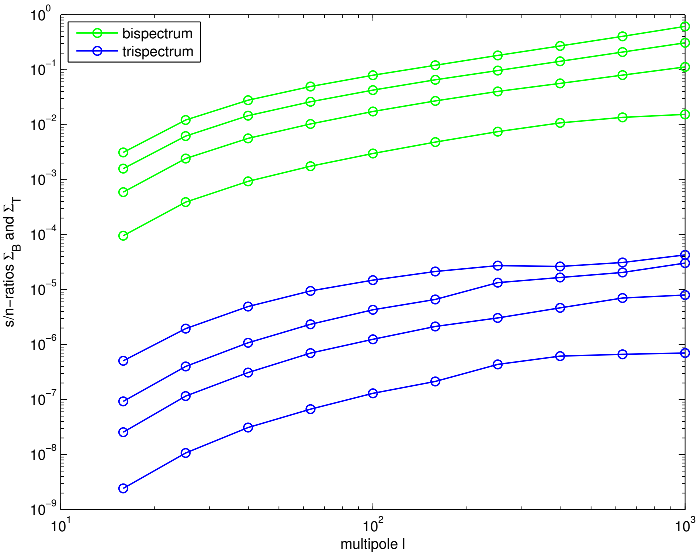

Figure 7.10: Cumulative signal to noise ratios Σ_B (green liness) and Σ_T (blue lines) for measuring the bi- and trispectrum in a tomographic weak lensing survey, with $N = 1, 2, 3, 4$ (bottom to top) redshift bins.

Part IV

SUMMARY AND CONCLUSIONS

SUMMARY AND CONCLUSIONS

The relativistic effect of gravitational lensing has become, over the years, one of the most promising cosmological tools. The well understood relation between light deflection and the mass that acts on it as a lens, permits to use lensing to probe the distribution of matter in our Universe, especially if we consider this phenomenon's most common regime, referred to as weak lensing.

This work intended to propose weak gravitational lensing as a means both to detect baryon acoustic oscillations and to measure the amount of primordial non-Gaussianities, possibly testing the relation that exists between some of the quantities by which they are parametrized.

BAO: Motivation

Baryon acoustic oscillations are particularly interesting from a cosmological point of view. They originated back in the time when baryonic matter and radiation were coupled, and can now be observed as a characteristic clustering length in the matter distribution. They are extremely good candidates to the role of statistical standard rulers, and can therefore contribute to the study of the properties and the evolution of dark energy. A lensing approach to BAO detection would benefit, for instance, from weak lensing's sensitivity to both dark matter and baryons, and could probe smaller redshifts than CMB.

primordial n-G: Motivation

Primordial non-Gaussianities, on the other hand, can help to discriminate among competing models of inflation. In effect, some of these models predict different amount, or different shapes of non-Gaussianity in the primordial distribution of density fluctuations. Some of them even predict a violation of the fundamental relation that exists between two non-Gaussianity parameters: the Suyama-Yamaguchi inequality. Detecting such violation could lead to prefer these models, and the mechanisms they propose as responsible for inflation. The main advantage of adopting weak lensing to measure primordial non-Gaussianities, would be providing an independent new method, subject to different systematics and, most of all, probing smaller scales than CMB. Such a characteristics would be valuable in case of a scale-dependent non-Gaussianity.

BAO WITH 3DWL We addressed the first of these problems by carrying out a statistical investigation to determine whether future surveys could detect BAO with a 3d weak lensing method, with a special attention to Euclid, DES or the hypothetical deep-reaching DEEP.

assumptions

To simplify the analysis, we assumed a fixed wCDM cosmology, and that noise sources like the shape-noise or the photometric-redshift error could be described by independent, Gaussian statistics.

technique

The model was parametrized by the amplitudes of the CDM power spectrum $P(k)$ at the positions of the less damped baryonic oscillations, as they are predicted by the cosmology we assumed. By varying $P(k)$ in a way that preserved its wiggle-shape in those wave number intervals, and by using a Fisher matrix approach, we calculated the best errors σ_α to expect for the amplitudes of $P(k)$ at such positions.

results

We tested the sensitivity of such statistical precisions, and estimated the best errors to expect for surveys like Euclid, DES, and DEEP. Moreover, we inferred the maximum number of wiggles that can be simultaneously constrained with reasonably small errors. It was found that

1. Among all the survey characteristics, σ_α seemed to be particularly sensitive to volume and density of the galaxy sample. This held, at least, for relatively small values of the redshift error, i. e. $\sigma_z < 0.1 - 0.2$.
2. Euclid, immediately followed by DES, gave the best performance. We estimated that Euclid could allow for the simultaneous detection of the first four baryonic wiggles with sensible precision, whereas DES is not expected to go beyond the third harmonic.

PRIMORDIAL NON-GAUSSIANITIES WITH WL Our second investigation focused on the study of a weak lensing approach to primordial non-Gaussianities.

"A weak lensing view on primordial non-Gaussianities"

We initially started by estimating the strength of the signal for local, equilateral and orthogonal forms of primordial non-Gaussianities in the weak lensing bispectrum. We did so by means of a Monte Carlo integration of the signal-to-noise ratio computations. Such study proved weak lensing to have a weaker constraining power than CMB, concluding that $f_{NL} = 200, 575, 1628$ (for local, orthogonal and equilateral shape, respectively) is necessary for weak lensing to be able to claim a detection. We also found that a wrong model choice in the fitting of the data bispectrum could lead to misestimates on f_{NL} of the order of ± 3. In addition, the propagation on f_{NL} estimate of a partially wrong subtraction of the structure formation signal, is found to be dependent on the prior considered. A prior consisting in Euclid weak lensing and BAO data, and PLANCK's results on the temperature and polarization maps, would yield uncertainties of $\sim 29, 98, 149$ for local, orthogonal, and equilateral non-Gaussianities.

Finally, we analyzed weak lensing sensitivity as a test for the relation that exists between f_{NL} and τ_{NL}, i. e. the Suyama-Yamaguchi inequality.

assumptions

In the study, a wCDM cosmology was assumed; also, flat polar coordinates and a Gaussian expression for the signal covariance were used in the integrations of the signal-to-noise ratios. We considered a local form of non-Gaussianity, parametrized by f_{NL}, g_{NL} and τ_{NL}, and the case of the projected Euclid weak lensing survey.

technique

Our analysis was carried out by computing inflationary bi- and trispectra by weak lensing and the correspondent signal-to-noise ratio via a very efficient Monte Carlo integration. The Fisher matrix of the f_{NL}, g_{NL} and τ_{NL} parameters was also evaluated with a similar numerical method, and from this, we derived the likelihood of the parameters f_{NL} and τ_{NL}.

results

Thanks to the likelihood $\mathcal{L}(f_{NL}, \tau_{NL})$, we could estimate the degree of belief of the Suyama-Yamaguchi inequality, stating $\tau_{NL} \geqslant (6/5 f_{NL})^2$. We could conclude that data coming from a survey like Euclid would provide a reliable statement on the inequality only for $\tau_{NL} \gtrsim 10^5$, that would give evidence for its validity, and $f_{NL} \gtrsim 10^2$, that would instead indicate a violation of the relation.

In summary, one can conclude that measurements of baryon acoustic oscillations with 3d weak lensing are possible. Future surveys like Euclid or DES should allow to detect higher amplitude oscillations like the first four or three. A 3d weak lensing approach would avoid issues related to galaxy biasing and redshift-space distortions, and therefore be particularly valuable.

Further steps can be made to advance this work, like estimating the precision gain on inferences about dark energy density and equation of state, when low-redshift BAO data from lensing is added to intermediate and high redshift probes (from galaxy distribution and CMB, respectively). An investigation of the impact of systematical errors on the estimation process from 3dWL data and biases in the estimation of BAO-wiggle amplitudes, could also be useful.

On the other side, we acknowledge the fact that weak lensing sensitivity to primordial non-Gaussianities is not competitive with probes like the CMB, and large degrees of non-Gaussianity would be necessary, in order to be able to observe them with such a method. Large primordial non-Gaussianities would be also needed for a better probing of the Suyama-Yamaguchi relation. Nonetheless, weak lensing could probe smaller scales than CMB, possibly allowing for the detection of a scale-dependence of the non-linearity parameters. Finally, if τ_{NL} is large enough to be observed, then the current constraints on f_{NL} would imply $\tau_{NL} \gg f_{NL}^2$, hence ruling out single field inflationary models, as well as many multi-field scenarios, all predicting the Suyama-Yamaguchi relation to be close to an equality.

Among the future developments to this work, I would definitely suggest a thorough study of the improvement on τ_{NL} and f_{NL} constraints, coming from a tomographic analysis, that already seems particularly promising.

APPENDIX

A

NUMERICAL METHOD FOR THE CALCULATION OF THE 3D WEAK LENSING COVARIANCE

In this appendix, I will illustrate the numerical method we used for the calculation of the covariance matrix of the 3d weak lensing convergence.

We have seen that the covariance $C_{\kappa,\ell}(k,k')$ is the sum of a noise part (Equation 4.25) and a signal part (Equation 4.22). Then $C_{\kappa,\ell}(k,k')$ can be either calculated directly from the previous equations, that are numerically quite demanding, or via a more efficient and more stable method, derived by Ayaita et al. [2012] and adopted in this work.

During this derivation, I will use the standard matrix notation, relating to the one used in Chapter 4 in the following way

$$A_{kk'} = A(k,k')\sqrt{k^2\Delta k}\,\sqrt{k'^2\Delta k'}, \tag{A.1}$$

where, for a multiplication between matrix, the coefficients reproduce the summation convention[1].

Since the trace operation is independent of the basis, and the Fisher matrix is given by a trace, we can choose a transformation that simplifies the numerical computation. Let this transformation be denoted by T^ℓ:

$$\tilde{C}_\ell = (T^\ell)^{-1} C_\ell T^\ell, \tag{A.2}$$

A natural choice for such a basis change would be an orthogonal T^ℓ, i. e. $(T^\ell)^{-1} = (T^\ell)^T$, chosen in such a way that the transformed matrix

---

[1] $\sum_k k^2\Delta k \sim \int dk k^2$

$\tilde{M}^\ell$ is diagonal. This occurs by means of the orthogonality relations if we define

$$T^\ell_{k\rho} = \sqrt{\frac{2}{\pi}}\sqrt{\rho^2\Delta\rho}\sqrt{k^2\Delta k}\, j_\ell(k\rho), \tag{A.3}$$

where the pre-factors are given by the normalization of the eigenvectors.

In this way $\tilde{M}^\ell$ becomes, as desired

$$\tilde{M}^\ell_{\rho\rho'} = T^\ell_{\rho k}\, M^\ell_{kk'}\, T^\ell_{k'\rho'} = \bar{n}(\rho)\delta_{\rho\rho'}, \tag{A.4}$$

whereas for the signal part, since we have $S^\ell \propto B^\ell_{kk'}\, P(k')\, (B^\ell_{kk'})^T$, the transformation implies an action of T^ℓ on the B^ℓ matrix of the type

$$\tilde{B}^\ell_{\rho k'} = T^\ell_{k\rho} B^\ell_{kk'}. \tag{A.5}$$

It can be shown that, by making use of the orthogonality relation, the final expression for B^ℓ is

$$\begin{aligned} \tilde{B}^\ell_{\rho k'} &= 2\sqrt{\frac{2}{\pi}}\,\sqrt{\rho^2\Delta\rho}\int_0^\infty d\chi\, p(\rho|\chi)n(\chi)\,\cdot \\ &\cdot \int_0^\chi d\chi'\, j_\ell(k'\chi')\,\frac{\chi-\chi'}{\chi\chi'}\frac{D_+}{a}\sqrt{k'^2\Delta k}. \end{aligned} \tag{A.6}$$

Once we have Equation A.6 we can use it for the calculation of the signal part, while the noise part is already given by Equation A.4. By the sum of these two contributions, the covariance matrix for a given ℓ can be computed and then used in the evaluation of the Fisher matrix.

BIBLIOGRAPHY

Abramowitz, M. and Stegun, I. A. (1972). *Handbook of Mathematical Functions*. Handbook of Mathematical Functions, New York: Dover, 1972.

Acquaviva, V., Baccigalupi, C., and Perrotta, F. (2004). Weak lensing in generalized gravity theories. *Phys. Rev. D*, 70(2):023515.

Adler, R. J. (1981). *The Geometry of Random Fields*.

Albrecht, A., Bernstein, G., Cahn, R., Freedman, W. L., Hewitt, J., Hu, W., Huth, J., Kamionkowski, M., Kolb, E. W., Knox, L., Mather, J. C., Staggs, S., and Suntzeff, N. B. (2006). Report of the Dark Energy Task Force. *ArXiv Astrophysics e-prints*.

Alcock, C. and Paczynski, B. (1979). An evolution free test for non-zero cosmological constant. *Nature*, 281:358.

Alishahiha, M., Silverstein, E., and Tong, D. (2004). DBI in the sky: Non-Gaussianity from inflation with a speed limit. *Phys. Rev. D*, 70(12):123505.

Allahverdi, R., Brandenberger, R., Cyr-Racine, F.-Y., and Mazumdar, A. (2010). Reheating in Inflationary Cosmology: Theory and Applications. *Annual Review of Nuclear and Particle Science*, 60:27–51.

Allen, S. W., Schmidt, R. W., and Fabian, A. C. (2002). Cosmological constraints from the X-ray gas mass fraction in relaxed lensing clusters observed with Chandra. *MNRAS*, 334:L11–L15.

Amara, A. and Réfrégier, A. (2007). Optimal surveys for weak-lensing tomography. *MNRAS*, 381:1018–1026.

Angulo, R. E., Baugh, C. M., Frenk, C. S., and Lacey, C. G. (2008). The detectability of baryonic acoustic oscillations in future galaxy surveys. *MNRAS*, 383:755–776.

Anselmi, S. and Pietroni, M. (2012). Nonlinear Power Spectrum from Resummed Perturbation Theory: a Leap Beyond the BAO Scale. *ArXiv e-prints 1205.2235*.

Arfken, G. B. and Weber, H. J. (2005). Mathematical methods for physicists 6th ed. *Materials and Manufacturing Processes*.

Arkani-Hamed, N., Creminelli, P., Mukohyama, S., and Zaldarriaga, M. (2004). Ghost inflation. *JCAP*, 4:1.

Ayaita, Y., Schäfer, B. M., and Weber, M. (2012). Investigating clustering dark energy with 3D weak cosmic shear. *MNRAS*, 422:3056–3066.

Babich, D. (2005). Optimal estimation of non-Gaussianity. *Phys. Rev. D*, 72(4):043003.

Ballinger, W. E., Heavens, A. F., and Taylor, A. N. (1995). The real-space power spectrum of IRAS galaxies on large scales and the redshift distortion. *MNRAS*, 276:L59–L63.

Bardeen, J. M., Bond, J. R., Kaiser, N., and Szalay, A. S. (1986). The statistics of peaks of Gaussian random fields. *ApJ*, 304:15–61.

Barnaby, N. (2010). Non-Gaussianity from Particle Production during Inflation. *Advances in Astronomy*, 2010.

Bartelmann, M. (2010a). Gravitational Lensing. *ArXiv e-prints*.

Bartelmann, M. (2010b). The dark Universe. *Reviews of Modern Physics*, 82:331–382.

Bartelmann, M. (2010c). TOPICAL REVIEW Gravitational lensing. *Classical and Quantum Gravity*, 27(23):233001.

Bartelmann, M. (2012). *Development of Cosmology: From a Static Universe to Accelerated Expansion*, page 49.

Bartelmann, M. and Schneider, P. (2001). Weak gravitational lensing. *Physics Reports*, 340:291–472.

Bartolo, N., Fasiello, M., Matarrese, S., and Riotto, A. (2010). Tilt and running of cosmological observables in generalized single-field inflation. *JCAP*, 12:26.

Bartolo, N., Komatsu, E., Matarrese, S., and Riotto, A. (2004). Non-Gaussianity from inflation: theory and observations. *Physics Reports*, 402:103–266.

Bassett, B. and Hlozek, R. (2010). *Baryon acoustic oscillations*, page 246.

Bassett, B. A., Tsujikawa, S., and Wands, D. (2006). Inflation dynamics and reheating. *Reviews of Modern Physics*, 78:537–589.

Becker, A., Huterer, D., and Kadota, K. (2011). Scale-Dependent Non-Gaussianity as a Generalization of the Local Model. *JCAP*, 1101:006. * Temporary entry *.

Beltrán Almeida, J. P., Rodríguez, Y., and Valenzuela-Toledo, C. A. (2013). The Suyama-Yamaguchi Consistency Relation in the Presence of Vector Fields. *Modern Physics Letters A*, 28:50012.

Benitez, N., Gaztanaga, E., Miquel, R., Castander, F., Moles, M., Crocce, M., Fernandez-Soto, A., Fosalba, P., Ballesteros, F., Campa, J., Cardiel-Sas, L., Castilla, J., Cristobal-Hornillos, D., Delfino, M., Fernandez, E., Fernandez-Sopuerta, C., Garcia-Bellido, J., Lobo, J., Martinez, V., Ortiz, A., Pacheco, A., Paredes, S., Pons-Borderia, M., Sanchez, E., Sanchez, S., Varela, J., and de Vicente, J. (2008). Measuring baryon acoustic oscillations along the line of sight with photometric redshifs: the pau survey.

Bennett, C. L., Kogut, A., Hinshaw, G., Banday, A. J., Wright, E. L., Gorski, K. M., Wilkinson, D. T., Weiss, R., and et, a. (1994). Cosmic temperature fluctuations from two years of COBE differential microwave radiometers observations. *ApJ*, 436:423–442.

Bernardeau, F., Colombi, S., Gaztañaga, E., and Scoccimarro, R. (2002). Large-scale structure of the Universe and cosmological perturbation theory. *Physics Reports*, 367:1–248.

Beutler, F., Blake, C., Colless, M., Jones, D. H., Staveley-Smith, L., Campbell, L., Parker, Q., Saunders, W., and Watson, F. (2011). The 6dF Galaxy Survey: baryon acoustic oscillations and the local Hubble constant. *MNRAS*, 416:3017–3032.

Blake, C. and Glazebrook, K. (2003). Probing Dark Energy Using Baryonic Oscillations in the Galaxy Power Spectrum as a Cosmological Ruler. *ApJ*, 594:665–673.

Blake, C., Parkinson, D., Bassett, B., Glazebrook, K., Kunz, M., and Nichol, R. C. (2006). Universal fitting formulae for baryon oscillation surveys. *MNRAS*, 365:255–264.

Bond, J. R., Frolov, A. V., Huang, Z., and Kofman, L. (2009). Non-Gaussian Curvature Spikes from Chaotic Billiards in Inflation Preheating. *Physical Review Letters*, 103(7):071301.

Buchalter, A., Helfand, D. J., Becker, R. H., and White, R. L. (1998). Constraining Omega 0 with the Angular Size–Redshift Relation of Double-lobed Quasars in the FIRST Survey. *ApJ*, 494:503.

Buchert, T. (1994). Lagrangian Theory of Gravitational Instability of Friedman-Lemaitre Cosmologies - a Generic Third-Order Model for Nonlinear Clustering. *MNRAS*, 267:811.

Busca, N. G., Delubac, T., Rich, J., Bailey, S., Font-Ribera, A., Kirkby, D., Goff, J.-M. L., Pieri, M. M., Slosar, A., Aubourg, É., Bautista, J. E., Bizyaev, D., Blomqvist, M., Bolton, A. S., Bovy, J., Brewington, H., Borde, A., Brinkmann, J., Carithers, B., Croft, R. A. C., Dawson, K. S., Ebelke, G., Eisenstein, D. J., Hamilton, J.-C., Ho, S., Hogg, D. W., Honscheid, K., Lee, K.-G., Lundgren, B., Malanushenko, E., Malanushenko, V., Margala, D., Maraston, C., Mehta, K., Miralda-Escudé, J., Myers, A. D., Nichol, R. C., Noterdaeme, P., Olmstead, M. D., Oravetz, D., Palanque-Delabrouille, N., Pan, K., Pâris, I., Percival, W. J., Petitjean, P., Roe, N. A., and et al. (16 additional authors not shown) (2012). Baryon acoustic oscillations in the ly-alpha forest of boss quasars.

Busca, N. G., Delubac, T., Rich, J., Bailey, S., Font-Ribera, A., Kirkby, D., Le Goff, J.-M., Pieri, M. M., and et, a. (2012). Baryon Acoustic Oscillations in the Ly-alpha forest of BOSS quasars. *ArXiv e-prints 1211.2616*.

Byrnes, C. T., Choi, K.-Y., and Hall, L. M. (2009). Large non-Gaussianity from two-component hybrid inflation. *JCAP*, 0902:017.

Byrnes, C. T., Enqvist, K., and Takahashi, T. (2010a). Scale-dependence of non-Gaussianity in the curvaton model. *JCAP*, 9:26.

Byrnes, C. T., Gerstenlauer, M., Nurmi, S., Tasinato, G., and Wands, D. (2010b). Scale-dependent non-Gaussianity probes inflationary physics. *JCAP*, 10:4–+.

Byrnes, C. T., Sasaki, M., and Wands, D. (2006). The primordial trispectrum from inflation. *Phys.Rev.*, D74:123519.

Byun, J. and Bean, R. (2013). Non-Gaussian Shape Recognition. *ArXiv e-prints 1303.3050*.

Cabré, A. and Gaztañaga, E. (2011). Have baryonic acoustic oscillations in the galaxy distribution really been measured? *MNRAS*, 412:L98–L102.

Cai, Y.-C., Angulo, R. E., Baugh, C. M., Cole, S., Frenk, C. S., and Jenkins, A. (2009). Mock galaxy redshift catalogues from simulations: implications for Pan-STARRS1. *MNRAS*, 395:1185–1203.

Carroll, S. M., Press, W. H., and Turner, E. L. (1992). The cosmological constant. *ARA&A*, 30:499–542.

Casaponsa, B., Barreiro, R. B., Curto, A., Martínez-González, E., and Vielva, P. (2011). Wilkinson Microwave Anisotropy Probe 7-yr constraints on f_{NL} with a fast wavelet estimator. *MNRAS*, 411:2019–2025.

Castro, P. G., Heavens, A. F., and Kitching, T. D. (2005). Weak lensing analysis in three dimensions. *Phys. Rev. D*, 72(2):023516.

Chen, X. (2005). Running non-Gaussianities in Dirac-Born-Infeld inflation. *Phys. Rev. D*, 72(12):123518.

Chen, X. (2010). Primordial Non-Gaussianities from Inflation Models. *Advances in Astronomy*, 2010.

Chen, X., Easther, R., and Lim, E. A. (2007). Large non-Gaussianities in single-field inflation. *JCAP*, 6:23.

Chen, X., Easther, R., and Lim, E. A. (2008). Generation and characterization of large non-Gaussianities in single field inflation. *JCAP*, 4:10.

Cheung, C., Fitzpatrick, A. L., Kaplan, J., Senatore, L., and Creminelli, P. (2008). The effective field theory of inflation. *Journal of High Energy Physics*, 3:14–014.

Coles, P. (1993). Galaxy formation with a local bias. *MNRAS*, 262:1065–1075.

Coles, P. and Lucchin, F. (2002). *Cosmology: The Origin and Evolution of Cosmic Structure, Second Edition*.

Cooray, A. and Hu, W. (2001). Power Spectrum Covariance of Weak Gravitational Lensing. *ApJ*, 554:56–66.

Cooray, A., Hu, W., Huterer, D., and Joffre, M. (2001). Measuring Angular Diameter Distances through Halo Clustering. *ApJL*, 557:L7–L10.

Creminelli, P., Nicolis, A., Senatore, L., Tegmark, M., and Zaldarriaga, M. (2006). Limits on non-Gaussianities from WMAP data. *JCAP*, 5:4.

Creminelli, P. and Zaldarriaga, M. (2004). A single-field consistency relation for the three-point function. *JCAP*, 10:6.

Crocce, M. and Scoccimarro, R. (2006a). Memory of initial conditions in gravitational clustering. *Phys. Rev. D*, 73(6):063520.

Crocce, M. and Scoccimarro, R. (2006b). Renormalized cosmological perturbation theory. *Phys. Rev. D*, 73(6):063519.

Crocce, M. and Scoccimarro, R. (2008). Nonlinear evolution of baryon acoustic oscillations. *Phys. Rev. D*, 77(2):023533.

Del Popolo, A. (2013). Non-Baryonic Dark Matter in Cosmology. *ArXiv e-prints*.

Desjacques, V., Crocce, M., Scoccimarro, R., and Sheth, R. K. (2010). Modeling scale-dependent bias on the baryonic acoustic scale with the statistics of peaks of Gaussian random fields. *Phys. Rev. D*, 82(10):103529.

Desjacques, V. and Seljak, U. (2010a). Primordial non-Gaussianity from the large-scale structure. *Classical and Quantum Gravity*, 27(12):124011–+.

Desjacques, V. and Seljak, U. (2010b). Primordial Non-Gaussianity in the Large-Scale Structure of the Universe. *Advances in Astronomy*, 2010.

Dodelson, S. and Zhang, P. (2005). Weak lensing bispectrum. *Phys. Rev. D*, 72(8):083001.

Dolney, D., Jain, B., and Takada, M. (2006). Baryon oscillations and dark-energy constraints from imaging surveys. *MNRAS*, 366:884–898.

Doroshkevich, A. G., Zeldovich, Y. B., and Syunyaev, R. A. (1978). Fluctuations of the microwave background radiation in the adiabatic and entropic theories of galaxy formation. *Soviet Astronomy*, 22:523.

Einasto, J. (2009). Dark Matter. *ArXiv e-prints*.

Einasto, J. (2011). Dark Matter. *Baltic Astronomy*, 20:231–240.

Eisenstein, D. (2003). Large-Scale Structure and Future Surveys. *ArXiv Astrophysics e-prints*.

Eisenstein, D. J. and Hu, W. (1998). Baryonic Features in the Matter Transfer Function. *ApJ*, 496:605.

Eisenstein, D. J. and Hu, W. (1999). Power Spectra for Cold Dark Matter and Its Variants. *ApJ*, 511:5–15.

Eisenstein, D. J., Seo, H.-J., Sirko, E., and Spergel, D. N. (2007a). Improving Cosmological Distance Measurements by Reconstruction of the Baryon Acoustic Peak. *ApJ*, 664:675–679.

Eisenstein, D. J., Seo, H.-J., and White, M. (2007b). On the robustness of the acoustic scale in the low-redshift clustering of matter. *Astrophys.J.*, 664:660–674.

Eisenstein, D. J. and White, M. (2004). Theoretical uncertainty in baryon oscillations. *Phys.Rev.D*, 70:103523.

Eisenstein, D. J., Zehavi, I., Hogg, D. W., Scoccimarro, R., Blanton, M. R., Nichol, R. C., Scranton, R., Seo, H.-J., and et, a. (2005). Detection of the Baryon Acoustic Peak in the Large-Scale Correlation Function of SDSS Luminous Red Galaxies. *ApJ*, 633:560–574.

Elliston, J., Alabidi, L., Huston, I., Mulryne, D., and Tavakol, R. (2012). Large trispectrum in two-field slow-roll inflation. *JCAP*, 1209:001.

Enqvist, K. and Sloth, M. S. (2002). Adiabatic CMB perturbations in pre-Big-Bang string cosmology. *Nuclear Physics B*, 626:395–409.

Fedeli, C., Carbone, C., Moscardini, L., and Cimatti, A. (2011a). The clustering of galaxies and galaxy clusters: constraints on primordial non-Gaussianity from future wide-field surveys. *MNRAS*, 414:1545–1559.

Fedeli, C., Pace, F., Moscardini, L., Grossi, M., and Dolag, K. (2011b). The effect of primordial non-Gaussianity on the skeleton of cosmic shear maps. *MNRAS*, 416:3098–3107.

Fergusson, J. and Shellard, E. (2009). The shape of primordial non-Gaussianity and the CMB bispectrum. *Phys.Rev.*, D80:043510.

Fergusson, J. R., Liguori, M., and Shellard, E. P. S. (2010). General CMB and primordial bispectrum estimation: Mode expansion, map making, and measures of F_{NL}. *Phys. Rev. D*, 82(2):023502–+.

Fergusson, J. R. and Shellard, E. P. S. (2007). Primordial non-Gaussianity and the CMB bispectrum. *Phys. Rev. D*, 76(8):083523–+.

Frenk, C. S. and White, S. D. M. (2012). Dark matter and cosmic structure. *Annalen der Physik*, 524:507–534.

Fry, J. N. (1996). The Evolution of Bias. *ApJL*, 461:L65.

Gangui, A., Lucchin, F., Matarrese, S., and Mollerach, S. (1994). The three-point correlation function of the cosmic microwave background in inflationary models. *ApJ*, 430:447–457.

Gaztañaga, E., Cabré, A., Castander, F., Crocce, M., and Fosalba, P. (2009a). Clustering of luminous red galaxies - III. Baryon acoustic peak in the three-point correlation. *MNRAS*, 399:801–811.

Gaztañaga, E., Cabré, A., and Hui, L. (2009b). Clustering of luminous red galaxies - IV. Baryon acoustic peak in the line-of-sight direction and a direct measurement of H(z). *MNRAS*, 399:1663–1680.

Grassi, A., Heisenberg, L., Byrnes, C. T., and Schäfer, B. M. (2013). A test of the Suyama-Yamaguchi inequality from weak lensing. *in preparation*.

Grassi, A. and Schäfer, B. M. (2013). Detecting baryon acoustic oscillations by 3d weak lensing. *ArXiv e-prints*.

Gurvits, L. I. (1994). Apparent milliarcsecond sizes of active galactic nuclei and the geometry of the universe. *ApJ*, 425:442–449.

Guth, A. H. (1981). Inflationary universe: A possible solution to the horizon and flatness problems. *Phys. Rev. D*, 23:347–356.

Hahn, T. (2005). Cuba, a library for multidimensional numerical integration. *Computer Physics Communications*, 168(2):78 – 95.

Hamana, T., Colombi, S. T., Thion, A., Devriendt, J. E. G. T., Mellier, Y., and Bernardeau, F. (2002). Source-lens clustering effects on the skewness of the lensing convergence. *MNRAS*, 330:365–377.

Hamilton, A. J. S. (2009). Power Spectrum Estimation. I. Basics. In Martínez, V. J., Saar, E., Martínez-González, E., and Pons-Bordería, M.-J., editors, *Data Analysis in Cosmology*, volume 665 of *Lecture Notes in Physics, Berlin Springer Verlag*, pages 415–431.

Heavens, A. (2003). 3D weak lensing. *MNRAS*, 343:1327–1334.

Heavens, A. F., Kitching, T. D., and Taylor, A. N. (2006). Measuring dark energy properties with 3D cosmic shear. *MNRAS*, 373:105–120.

Heavens, A. F. and Taylor, A. N. (1995). A spherical harmonic analysis of redshift space. *MNRAS*, 275:483–497.

Heymans, C., Grocutt, E., Heavens, A., Kilbinger, M., Kitching, T. D., Simpson, F., Benjamin, J., Erben, T., and et al. (2013). CFHTLenS tomographic weak lensing cosmological parameter constraints: Mitigating the impact of intrinsic galaxy alignments. *ArXiv e-prints 1303.1808*.

Hinshaw, G., Nolta, M. R., Bennett, C. L., Bean, R., Doré, O., Greason, M. R., Halpern, M., Hill, R. S., and et, a. (2007). Three-Year Wilkinson Microwave Anisotropy Probe (WMAP) Observations: Temperature Analysis. *ApJS*, 170:288–334.

Hinshaw, G., Spergel, D. N., Verde, L., Hill, R. S., Meyer, S. S., Barnes, C., Bennett, C. L., Halpern, M., and et, a. (2003). First-Year Wilkinson Microwave Anisotropy Probe (WMAP) Observations: The Angular Power Spectrum. *ApJS*, 148:135–159.

Hoekstra, H. and Jain, B. (2008). Weak Gravitational Lensing and Its Cosmological Applications. *Annual Review of Nuclear and Particle Science*, 58:99–123.

Hu, W. (1999). Power Spectrum Tomography with Weak Lensing. *ApJL*, 522:L21–L24.

Hu, W. (2000). Weak lensing of the CMB: A harmonic approach. *Phys. Rev. D*, 62(4):043007.

Hu, W. (2001). Angular trispectrum of the cosmic microwave background. *Phys. Rev. D*, 64(8):083005.

Hu, W. and Sugiyama, N. (1996). Small-Scale Cosmological Perturbations: an Analytic Approach. *ApJ*, 471:542.

Hu, W. and White, M. (2001). Power Spectra Estimation for Weak Lensing. *ApJ*, 554:67–73.

Huff, E., Schulz, A. E., White, M., Schlegel, D. J., and Warren, M. S. (2007). Simulations of baryon oscillations. *Astroparticle Physics*, 26:351–366.

Ichikawa, K., Suyama, T., Takahashi, T., and Yamaguchi, M. (2008). Primordial Curvature Fluctuation and Its Non-Gaussianity in Models with Modulated Reheating. *Phys.Rev.*, D78:063545.

Jackson, J. C. and Dodgson, M. (1997). Deceleration without dark matter. *MNRAS*, 285:806–810.

Jeong, D. and Komatsu, E. (2006). Perturbation Theory Reloaded: Analytical Calculation of Nonlinearity in Baryonic Oscillations in the Real-Space Matter Power Spectrum. *ApJ*, 651:619–626.

Jeong, D. and Komatsu, E. (2009). Perturbation Theory Reloaded. II. Nonlinear Bias, Baryon Acoustic Oscillations, and Millennium Simulation in Real Space. *ApJ*, 691:569–595.

Jeong, D., Schmidt, F., and Sefusatti, E. (2011). Primordial non-Gaussianity and the statistics of weak lensing and other projected density fields. *Phys. Rev. D*, 83(12):123005.

Joachimi, B., Shi, X., and Schneider, P. (2009). Bispectrum covariance in the flat-sky limit. *A&A*, 508:1193–1204.

Jürgens, G. and Bartelmann, M. (2012). Perturbation Theory Trispectrum in the Time Renormalisation Approach. *ArXiv e-prints 1204.6524*.

Kamionkowski, M., Smith, T. L., and Heavens, A. (2011). CMB bispectrum, trispectrum, non-Gaussianity, and the Cramer-Rao bound. *Phys. Rev. D*, 83(2):023007.

Kayo, I., Takada, M., and Jain, B. (2013). Information content of weak lensing power spectrum and bispectrum: including the non-Gaussian error covariance matrix. *MNRAS*, 429:344–371.

Kazin, E. A., Blanton, M. R., Scoccimarro, R., McBride, C. K., and Berlind, A. A. (2010a). Regarding the Line-of-sight Baryonic Acoustic Feature in the Sloan Digital Sky Survey and Baryon Oscillation Spectroscopic Survey Luminous Red Galaxy Samples. *ApJ*, 719:1032–1044.

Kazin, E. A., Blanton, M. R., Scoccimarro, R., McBride, C. K., Berlind, A. A., Bahcall, N. A., Brinkmann, J., Czarapata, P., and et, a. (2010b). The Baryonic Acoustic Feature and Large-Scale Clustering in the Sloan Digital Sky Survey Luminous Red Galaxy Sample. *ApJ*, 710:1444–1461.

Kellermann, K. I. (1993). The cosmological deceleration parameter estimated from the angular-size/redshift relation for compact radio sources. *Nature*, 361:134–136.

Kitching, T. D., Heavens, A. F., Taylor, A. N., Brown, M. L., Meisenheimer, K., Wolf, C., Gray, M. E., and Bacon, D. J. (2007). Cosmological constraints from COMBO-17 using 3D weak lensing. *MNRAS*, 376:771–778.

Kitching, T. D., Heavens, A. F., Verde, L., Serra, P., and Melchiorri, A. (2008a). Finding evidence for massive neutrinos using 3D weak lensing. *Phys. Rev. D*, 77(10):103008.

Kitching, T. D., Taylor, A. N., and Heavens, A. F. (2008b). Systematic effects on dark energy from 3D weak shear. *MNRAS*, 389:173–190.

Komatsu, E. (2003). Wilkinson Microwave Anisotropy Probe constraints on non-Gaussianity. *New Astronomy*, 47:797–803.

Komatsu, E. (2010). Hunting for Primordial Non-Gaussianity in the Cosmic Microwave Background. *Class.Quant.Grav.*, 27:124010.

Komatsu, E., Afshordi, N., Bartolo, N., Baumann, D., Bond, J., et al. (2009). Non-Gaussianity as a Probe of the Physics of the Primordial Universe and the Astrophysics of the Low Redshift Universe. *arXiv 0902.4759*.

Komatsu, E., Smith, K. M., Dunkley, J., Bennett, C. L., Gold, B., Hinshaw, G., Jarosik, N., Larson, D., Nolta, M. R., Page, L., Spergel, D. N., Halpern, M., Hill, R. S., Kogut, A., Limon, M., Meyer, S. S., Odegard, N., Tucker, G. S., Weiland, J. L., Wollack, E., and Wright, E. L. (2011). Seven-year Wilkinson Microwave Anisotropy Probe (WMAP) Observations: Cosmological Interpretation. *ApJS*, 192:18.

Komatsu, E. and Spergel, D. N. (2001). Acoustic signatures in the primary microwave background bispectrum. *Phys. Rev. D*, 63(6):063002.

Krause, E. and Hirata, C. M. (2010). Weak lensing power spectra for precision cosmology. Multiple-deflection, reduced shear, and lensing bias corrections. *A&A*, 523:A28.

Labatie, A., Starck, J. L., and Lachièze-Rey, M. (2012). Detecting Baryon Acoustic Oscillations. *ApJ*, 746:172.

Lanusse, F., Rassat, A., and Starck, J.-L. (2012). Spherical 3D isotropic wavelets. *A&A*, 540:A92.

Larson, D., Dunkley, J., Hinshaw, G., Komatsu, E., Nolta, M. R., Bennett, C. L., Gold, B., Halpern, M., and et, a. (2011). Seven-year Wilkinson Microwave Anisotropy Probe (WMAP) Observations: Power Spectra and WMAP-derived Parameters. *ApJS*, 192:16.

Lehners, J.-L. (2010). Ekpyrotic Nongaussianity: A Review. *Advances in Astronomy*, 2010.

Leistedt, B., Rassat, A., Réfrégier, A., and Starck, J.-L. (2012). 3DEX: a code for fast spherical Fourier-Bessel decomposition of 3D surveys. *A&A*, 540:A60.

Leonard, A., Dupé, F.-X., and Starck, J.-L. (2012). A compressed sensing approach to 3D weak lensing. *A&A*, 539:A85.

Lesgourgues, J. (2013). TASI Lectures on Cosmological Perturbations. *ArXiv e-prints 1302.4640*.

Leung, G., Tarrant, E. R. M., Byrnes, C. T., and Copeland, E. J. (2013). Influence of Reheating on the Trispectrum and its Scale Dependence.

Lewis, A. (2011). The real shape of non-Gaussianities. *JCAP*, 10:26.

Li, M., Wang, T., and Wang, Y. (2008). General single field inflation with large positive non-Gaussianity. *JCAP*, 3:28.

Liddle, A. R. and Lyth, D. H. (2000). *Cosmological Inflation and Large-Scale Structure*.

Limber, D. N. (1953). The Analysis of Counts of the Extragalactic Nebulae in Terms of a Fluctuating Density Field. *ApJ*, 117:134.

Limber, D. N. (1954). The Analysis of Counts of the Extragalactic Nebulae in Terms of a Fluctuating Density Field. II. *ApJ*, 119:655–+.

Lin, C. and Wang, Y. (2010). Quadra-spectrum and quint-spectrum from inflation and curvaton models.

Linder, E. V. and Jenkins, A. (2003). Cosmic structure growth and dark energy. *MNRAS*, 346:573–583.

Lo Verde, M., Miller, A., Shandera, S., and Verde, L. (2008). Effects of scale-dependent non-Gaussianity on cosmological structures. *JCAP*, 4:14–+.

LoVerde, M. and Smith, K. M. (2011). The non-Gaussian halo mass function with f_{NL}, g_{NL} and τ_{NL}. *JCAP*, 8:3.

Lyth, D. H. and Rodríguez, Y. (2005). Inflationary Prediction for Primordial Non-Gaussianity. *Physical Review Letters*, 95(12):121302.

Lyth, D. H., Ungarelli, C., and Wands, D. (2003). Primordial density perturbation in the curvaton scenario. *Phys. Rev. D*, 67(2):023503.

Lyth, D. H. and Wands, D. (2002). Generating the curvature perturbation without an inflaton. *Physics Letters B*, 524:5–14.

Ma, C.-P. and Bertschinger, E. (1995). Cosmological perturbation theory in the synchronous and conformal newtonian gauges. *Astrophys.J.*, 455:7–25.

Mantz, A., Allen, S. W., Ebeling, H., and Rapetti, D. (2008). New constraints on dark energy from the observed growth of the most X-ray luminous galaxy clusters. *MNRAS*, 387:1179–1192.

Marsaglia, G. (1965). Ratios of normal variables and ratios of sums of uniform variables. *Journal of the American Statistical Association*, 60(309):193–204.

Marsaglia, G. (2006). Ratios of normal variables. *Journal of Statistical Software*, 16(4):1–10.

Martin, J. (2012). Everything you always wanted to know about the cosmological constant problem (but were afraid to ask). *Comptes Rendus Physique*, 13:566–665.

Martin, J., Ringeval, C., and Vennin, V. (2013). Encyclopaedia Inflationaris. *ArXiv e-prints 1303.3787*.

Massey, R., Rhodes, J., Leauthaud, A., Capak, P., Ellis, R., Koekemoer, A., Réfrégier, A., Scoville, N., and et, a. (2007). COSMOS: Three-dimensional Weak Lensing and the Growth of Structure. *ApJS*, 172:239–253.

Matarrese, S. and Pietroni, M. (2008). Baryonic Acoustic Oscillations via the Renormalization Group. *Modern Physics Letters A*, 23:25–32.

Mehta, K. T., Cuesta, A. J., Xu, X., Eisenstein, D. J., and Padmanabhan, N. (2012). A 2% Distance to z = 0.35 by Reconstructing Baryon Acoustic Oscillations - III : Cosmological Measurements and Interpretation. *ArXiv e-prints 1202.0092*.

Mehta, K. T., Seo, H.-J., Eckel, J., Eisenstein, D. J., Metchnik, M., Pinto, P., and Xu, X. (2011). Galaxy Bias and Its Effects on the Baryon Acoustic Oscillation Measurements. *ApJ*, 734:94.

Meiksin, A., White, M., and Peacock, J. A. (1999). Baryonic signatures in large-scale structure. *MNRAS*, 304:851–864.

Mollerach, S. (1990). Isocurvature baryon perturbations and inflation. *Phys. Rev. D*, 42:313–325.

Montanari, F. and Durrer, R. (2011). Analytic approach to baryon acoustic oscillations. *Phys. Rev. D*, 84(2):023522.

Mukhanov, V. (2005). *Physical Foundations of Cosmology*.

Munshi, D., Heavens, A., and Coles, P. (2011). Higher-order convergence statistics for three-dimensional weak gravitational lensing. *MNRAS*, 411:2161–2185.

Munshi, D., Valageas, P., van Waerbeke, L., and Heavens, A. (2008). Cosmology with weak lensing surveys. *Physics Reports*, 462(3):67 – 121.

Munshi, D., van Waerbeke, L., Smidt, J., and Coles, P. (2012). From weak lensing to non-Gaussianity via Minkowski functionals. *MNRAS*, 419:536–555.

Nishimichi, T., Ohmuro, H., Nakamichi, M., Taruya, A., Yahata, K., Shirata, A., Saito, S., Nomura, H., Yamamoto, K., and Suto, Y. (2007). Characteristic Scales of Baryon Acoustic Oscillations from Perturbation Theory: Nonlinearity and Redshift-Space Distortion Effects. *PASJ*, 59:1049–.

Nishimichi, T., Shirata, A., Taruya, A., Yahata, K., Saito, S., Suto, Y., Takahashi, R., Yoshida, N., Matsubara, T., Sugiyama, N., Kayo, I., Jing, Y., and Yoshikawa, K. (2009). Modeling Nonlinear Evolution of Baryon Acoustic Oscillations: Convergence Regime of N-body Simulations and Analytic Models. *PASJ*, 61:321–.

Noh, Y., White, M., and Padmanabhan, N. (2009). Reconstructing baryon oscillations. *Phys. Rev. D*, 80(12):123501.

Nolta, M. R., Dunkley, J., Hill, R. S., Hinshaw, G., Komatsu, E., Larson, D., Page, L., Spergel, D. N., and et, a. (2009). Five-Year Wilkinson Microwave Anisotropy Probe Observations: Angular Power Spectra. *ApJS*, 180:296–305.

Pace, F., Moscardini, L., Bartelmann, M., Branchini, E., Dolag, K., Grossi, M., and Matarrese, S. (2011). A numerical study of the effects of primordial non-Gaussianities on weak lensing statistics. *MNRAS*, 411:595–606.

Padmanabhan, N., Schlegel, D. J., Seljak, U., Makarov, A., Bahcall, N. A., Blanton, M. R., Brinkmann, J., Eisenstein, D. J., and et, a. (2007). The clustering of luminous red galaxies in the Sloan Digital Sky Survey imaging data. *MNRAS*, 378:852–872.

Padmanabhan, N., Xu, X., Eisenstein, D. J., Scalzo, R., Cuesta, A. J., Mehta, K. T., and Kazin, E. (2012). A 2% Distance to z=0.35 by Reconstructing Baryon Acoustic Oscillations - I : Methods and Application to the Sloan Digital Sky Survey. *ArXiv e-prints 1202.0090*.

Padmanabhan, T. (1993). *Structure Formation in the Universe*.

Padmanabhan, T. (2003). Cosmological constant-the weight of the vacuum. *Physics Reports*, 380:235–320.

Parejko, J. K., Sunayama, T., Padmanabhan, N., Wake, D. A., Berlind, A. A., Bizyaev, D., Blanton, M., Bolton, A. S., and et, a. (2012). The clustering of galaxies in the SDSS-III Baryon Oscillation Spectroscopic Survey: the low redshift sample. *ArXiv e-prints 1211.3976*.

Parkinson, D., Riemer-Sørensen, S., Blake, C., Poole, G. B., Davis, T. M., Brough, S., Colless, M., Contreras, C., and et al. (2012). The wigglez dark energy survey: Final data release and cosmological results. *Phys. Rev. D*, 86:103518.

Peebles, P. J. E. (1968). Recombination of the Primeval Plasma. *ApJ*, 153:1.

Peebles, P. J. E. and Yu, J. T. (1970). Primeval Adiabatic Perturbation in an Expanding Universe. *ApJ*, 162:815.

Penzias, A. A. and Wilson, R. W. (1965). A Measurement of Excess Antenna Temperature at 4080 Mc/s. *ApJ*, 142:419–421.

Percival, W. J., Burkey, D., Heavens, A., Taylor, A., Cole, S., Peacock, J. A., Baugh, C. M., Bland-Hawthorn, J., and et, a. (2004). The 2dF Galaxy Redshift Survey: spherical harmonics analysis of fluctuations in the final catalogue. *MNRAS*, 353:1201–1218.

Percival, W. J., Cole, S., Eisenstein, D. J., Nichol, R. C., Peacock, J. A., Pope, A. C., and Szalay, A. S. (2007a). Measuring the Baryon Acoustic Oscillation scale using the Sloan Digital Sky Survey and 2dF Galaxy Redshift Survey. *MNRAS*, 381:1053–1066.

Percival, W. J., Nichol, R. C., Eisenstein, D. J., Weinberg, D. H., Fukugita, M., Pope, A. C., Schneider, D. P., Szalay, A. S., and et, a. (2007b). Measuring the Matter Density Using Baryon Oscillations in the SDSS. *ApJ*, 657:51–55.

Percival, W. J., Reid, B. A., Eisenstein, D. J., Bahcall, N. A., Budavari, T., Frieman, J. A., Fukugita, M., Gunn, J. E., and et, a. (2010). Baryon acoustic oscillations in the Sloan Digital Sky Survey Data Release 7 galaxy sample. *MNRAS*, 401:2148–2168.

Perlmutter, S., Aldering, G., Goldhaber, G., Knop, R. A., Nugent, P., Castro, P. G., Deustua, S., Fabbro, S., Goobar, A., Groom, D. E., Hook, I. M., Kim, A. G., Kim, M. Y., Lee, J. C., Nunes, N. J., Pain, R., Pennypacker, C. R., Quimby, R., Lidman, C., Ellis, R. S., Irwin, M., McMahon, R. G., Ruiz-Lapuente, P., Walton, N., Schaefer, B., Boyle, B. J., Filippenko, A. V., Matheson, T., Fruchter, A. S., Panagia, N., Newberg, H. J. M., Couch, W. J., and Supernova Cosmology Project (1999). Measurements of Omega and Lambda from 42 High-Redshift Supernovae. *ApJ*, 517:565–586.

Peter, A. H. G. (2012). Dark Matter: A Brief Review. *ArXiv e-prints*.

Peterson, C. M. and Tegmark, M. (2011). Non-Gaussianity in Two-Field Inflation. *Phys.Rev.*, D84:023520.

Pettinari, G. W., Fidler, C., Crittenden, R., Koyama, K., and Wands, D. (2013). The intrinsic bispectrum of the cosmic microwave background. *JCAP*, 4:3.

Pietroni, M. (2008). Flowing with time: a new approach to non-linear cosmological perturbations. *JCAP*, 10:36.

Planck Collaboration, Ade, P. A. R., Aghanim, N., Armitage-Caplan, C., Arnaud, M., Ashdown, M., Atrio-Barandela, F., Aumont, J., Baccigalupi, C., Banday, A. J., and et al. (2013a). Planck 2013 results. XVI. Cosmological parameters. *ArXiv e-prints 1303.5076*.

Planck Collaboration, Ade, P. A. R., Aghanim, N., Armitage-Caplan, C., Arnaud, M., Ashdown, M., Atrio-Barandela, F., Aumont, J., Baccigalupi, C., Banday, A. J., and et al. (2013b). Planck 2013 Results. XXIV. Constraints on primordial non-Gaussianity. *ArXiv e-prints*.

Pratten, G. and Munshi, D. (2013). BAOs and Non-linearities: 3D Spherical Analysis. *ArXiv e-prints*.

Preskill, J. P. (1979). Cosmological production of superheavy magnetic monopoles. *Physical Review Letters*, 43:1365–1368.

Press, W. H. and Schechter, P. (1974). Formation of Galaxies and Clusters of Galaxies by Self-Similar Gravitational Condensation. *ApJ*, 187:425–438.

Rassat, A. and Refregier, A. (2012). 3D spherical analysis of baryon acoustic oscillations. *A&A*, 540:A115.

Refregier, A. (2003). Weak Gravitational Lensing by Large-Scale Structure. *ARA&A*, 41:645–668.

Refregier, A. (2009). The Dark UNiverse Explorer (DUNE): proposal to ESA's cosmic vision. *Experimental Astronomy*, 23:17–37.

Riess, A. G., Filippenko, A. V., Challis, P., Clocchiatti, A., Diercks, A., Garnavich, P. M., Gilliland, R. L., Hogan, C. J., Jha, S., Kirshner, R. P., Leibundgut, B., Phillips, M. M., Reiss, D., Schmidt, B. P., Schommer, R. A., Smith, R. C., Spyromilio, J., Stubbs, C., Suntzeff, N. B., and Tonry, J. (1998). Observational Evidence from Supernovae for an Accelerating Universe and a Cosmological Constant. *AJ*, 116:1009–1038.

Riotto, A. and Sloth, M. S. (2011). Strongly scale-dependent non-Gaussianity. *Phys. Rev. D*, 83(4):041301.

Rodríguez, Y., Beltrán Almeida, J. P., and Valenzuela-Toledo, C. A. (2013). The different varieties of the Suyama-Yamaguchi consistency relation and its violation as a signal of statistical inhomogeneity. *JCAP*, 4:39.

Sahni, V. (2002). The cosmological constant problem and quintessence. *Classical and Quantum Gravity*, 19:3435–3448.

Sasaki, M. and Stewart, E. D. (1996). A General Analytic Formula for the Spectral Index of the Density Perturbations Produced during Inflation. *Progress of Theoretical Physics*, 95:71–78.

Sato, M. and Nishimichi, T. (2013). Impact of the non-Gaussian covariance of the weak lensing power spectrum and bispectrum on cosmological parameter estimation. *ArXiv e-prints 1301.3588*.

Schäfer, B. M. (2009). Galactic Angular Momenta and Angular Momentum Correlations in the Cosmological Large-Scale Structure. *International Journal of Modern Physics D*, 18:173–222.

Schäfer, B. M., Grassi, A., Gerstenlauer, M., and Byrnes, C. T. (2012). A weak lensing view on primordial non-Gaussianities. *MNRAS*, 421:797–807.

Schäfer, B. M., Pfrommer, C., and Zaroubi, S. (2005). Redshift estimation of clusters by wavelet decomposition of their Sunyaev-Zel'dovich morphology. *MNRAS*, 362:1418–1434.

Schneider, P., van Waerbeke, L., Jain, B., and Kruse, G. (1998). A new measure for cosmic shear. *MNRAS*, 296:873–892.

Schneider, P., van Waerbeke, L., and Mellier, Y. (2002). B-modes in cosmic shear from source redshift clustering. *A&A*, 389:729–741.

Seery, D. and Lidsey, J. E. (2005). Primordial non-Gaussianities in single-field inflation. *JCAP*, 6:3.

Seery, D., Lidsey, J. E., and Sloth, M. S. (2007). The inflationary trispectrum. *JCAP*, 1:27.

Sefusatti, E. and Komatsu, E. (2007). Bispectrum of galaxies from high-redshift galaxy surveys: Primordial non-Gaussianity and nonlinear galaxy bias. *Phys. Rev. D*, 76(8):083004.

Sefusatti, E., Liguori, M., Yadav, A. P., Jackson, M. G., and Pajer, E. (2009). Constraining Running Non-Gaussianity. *JCAP*, 0912:022.

Seitz, S. and Schneider, P. (1994). Some remarks on multiple deflection gravitational lensing. *A&A*, 287:349–360.

Seitz, S., Schneider, P., and Ehlers, J. (1994). Light propagation in arbitrary spacetimes and the gravitational lens approximation. *Classical and Quantum Gravity*, 11:2345–2373.

Seljak, U. and Zaldarriaga, M. (1996). A Line-of-Sight Integration Approach to Cosmic Microwave Background Anisotropies. *ApJ*, 469:437.

Semboloni, E., Heymans, C., van Waerbeke, L., and Schneider, P. (2008). Sources of contamination to weak lensing three-point statistics: constraints from N-body simulations. *MNRAS*, 388:991–1000.

Semboloni, E., Hoekstra, H., Schaye, J., van Daalen, M. P., and McCarthy, I. G. (2011). Quantifying the effect of baryon physics on weak lensing tomography. *MNRAS*, 417:2020–2035.

Seo, H.-J. and Eisenstein, D. J. (2003). Probing Dark Energy with Baryonic Acoustic Oscillations from Future Large Galaxy Redshift Surveys. *ApJ*, 598:720–740.

Seo, H.-J., Siegel, E. R., Eisenstein, D. J., and White, M. (2008). Nonlinear Structure Formation and the Acoustic Scale. *ApJ*, 686:13–24.

Shapiro, C. and Cooray, A. (2006). The Born and lens lens corrections to weak gravitational lensing angular power spectra. *Journal of Cosmology and Astro-Particle Physics*, 3:7–+.

Silk, J. (1968). Cosmic Black-Body Radiation and Galaxy Formation. *ApJ*, 151:459.

Silk, J. (2013). Observational Status of Dark Matter. In Calcagni, G., Papantonopoulos, L., Siopsis, G., and Tsamis, N., editors, *Lecture Notes in Physics, Berlin Springer Verlag*, volume 863 of *Lecture Notes in Physics, Berlin Springer Verlag*, page 271.

Silverstein, E. and Tong, D. (2004). Scalar speed limits and cosmology: Acceleration from D-cceleration. *Phys. Rev. D*, 70(10):103505.

Simpson, F., Peacock, J. A., and Simon, P. (2009). Locating the baryon acoustic peak. *Phys. Rev. D*, 79(6):063508.

Slosar, A., Iršič, V., Kirkby, D., Bailey, S., Busca, N. G., Delubac, T., Rich, J., Aubourg, É., Bautista, J. E., Bhardwaj, V., Blomqvist, M., Bolton, A. S., Bovy, J., Brownstein, J., Carithers, B., Croft, R. A. C., Dawson, K. S., Font-Ribera, A., Goff, J.-M. L., Ho, S., Honscheid, K., Lee, K.-G., Margala, D., McDonald, P., Medolin, B., Miralda-Escudé, J., Myers, A. D., Nichol, R. C., Noterdaeme, P., Palanque-Delabrouille, N., Pâris, I., Petitjean, P., Pieri, M. M., Piškur, Y., Roe, N. A., Ross, N. P., Rossi, G., Schlegel, D. J., Schneider, D. P., Sheldon, E. S., Seljak, U., Viel, M., Weinberg, D. H., and Yèche, C. (2013). Measurement of baryon acoustic oscillations in the lyman-alpha forest fluctuations in boss data release 9.

Smidt, J., Amblard, A., Byrnes, C. T., Cooray, A., Heavens, A., and Munshi, D. (2010). CMB contraints on primordial non-Gaussianity from the bispectrum (f_{NL}) and trispectrum (g_{NL} and τ_{NL}) and a new consistency test of single-field inflation. *Phys. Rev. D*, 81(12):123007.

Smith, K. M., Loverde, M., and Zaldarriaga, M. (2011a). Universal Bound on N-Point Correlations from Inflation. *Physical Review Letters*, 107(19):191301.

Smith, R. E., Scoccimarro, R., and Sheth, R. K. (2007). Scale dependence of halo and galaxy bias: Effects in real space. *Phys. Rev. D*, 75(6):063512.

Smith, T. L., Kamionkowski, M., and Wandelt, B. D. (2011b). The Probability Distribution for Non-Gaussianity Estimators. *ArXiv e-prints 1104.0930*.

Spergel, D. N., Bean, R., Doré, O., Nolta, M. R., Bennett, C. L., Dunkley, J., Hinshaw, G., Jarosik, N., Komatsu, E., Page, L., Peiris, H. V., Verde, L., Halpern, M., Hill, R. S., Kogut, A., Limon, M., Meyer, S. S., Odegard, N., Tucker, G. S., Weiland, J. L., Wollack, E., and Wright, E. L. (2007). Three-Year Wilkinson Microwave Anisotropy Probe (WMAP) Observations: Implications for Cosmology. *ApJS*, 170:377–408.

Springel, V., White, S. D. M., Jenkins, A., Frenk, C. S., Yoshida, N., Gao, L., Navarro, J., Thacker, R., and et, a. (2005). Simulations of the formation, evolution and clustering of galaxies and quasars. *Nature*, 435:629–636.

Starobinskiĭ, A. A. (1985). Multicomponent de Sitter (inflationary) stages and the generation of perturbations. *Soviet Journal of Experimental and Theoretical Physics Letters*, 42:152.

Sugiyama, N. (1995). Cosmic Background Anisotropies in Cold Dark Matter Cosmology. *ApJS*, 100:281.

Sugiyama, N. S. (2012). Consistency relation for multifield inflation scenario with all loop contributions. *JCAP*, 5:32.

Sutherland, W. (2012). On measuring the absolute scale of baryon acoustic oscillations. *MNRAS*, 426:1280–1290.

Suyama, T., Takahashi, T., Yamaguchi, M., and Yokoyama, S. (2010). On classification of models of large local-type non-Gaussianity. *JCAP*, 12:30.

Suyama, T. and Yamaguchi, M. (2008). Non-Gaussianity in the modulated reheating scenario. *Phys. Rev. D*, 77(2):023505.

Takada, M. and Hu, W. (2013). Power Spectrum Super-Sample Covariance. *ArXiv e-prints*.

Takada, M. and Jain, B. (2003a). The three-point correlation function in cosmology. *MNRAS*, 340:580–608.

Takada, M. and Jain, B. (2003b). Three-point correlations in weak lensing surveys: model predictions and applications. *MNRAS*, 344:857–886.

Takada, M. and Jain, B. (2004). Cosmological parameters from lensing power spectrum and bispectrum tomography. *MNRAS*, 348:897–915.

Takada, M. and Jain, B. (2009). The impact of non-Gaussian errors on weak lensing surveys. *MNRAS*, 395:2065–2086.

Taruya, A., Nishimichi, T., Saito, S., and Hiramatsu, T. (2009). Nonlinear evolution of baryon acoustic oscillations from improved perturbation theory in real and redshift spaces. *Phys. Rev. D*, 80(12):123503.

Tegmark, M., Eisenstein, D. J., Strauss, M. A., Weinberg, D. H., Blanton, M. R., Frieman, J. A., Fukugita, M., Gunn, J. E., Hamilton, A. J. S., Knapp, G. R., Nichol, R. C., Ostriker, J. P., Padmanabhan, N., Percival, W. J., Schlegel, D. J., Schneider, D. P., Scoccimarro, R., Seljak, U., Seo, H.-J., Swanson, M., Szalay, A. S., Vogeley, M. S., Yoo, J., Zehavi, I., Abazajian, K., Anderson, S. F., Annis, J., Bahcall, N. A., Bassett, B., Berlind, A., Brinkmann, J., Budavari, T., Castander, F., Connolly, A., Csabai, I., Doi, M., Finkbeiner, D. P., Gillespie, B., Glazebrook, K., Hennessy, G. S., Hogg, D. W., Ivezić, Ž., Jain, B., Johnston, D., Kent, S., Lamb, D. Q., Lee, B. C., Lin, H., Loveday, J., Lupton, R. H., Munn, J. A., Pan, K., Park, C., Peoples, J., Pier, J. R., Pope, A., Richmond, M., Rockosi, C., Scranton, R., Sheth, R. K., Stebbins, A., Stoughton, C., Szapudi, I., Tucker, D. L., vanden Berk, D. E., Yanny, B., and York, D. G. (2006). Cosmological constraints from the SDSS luminous red galaxies. *Phys. Rev. D*, 74(12):123507.

Tegmark, M., Taylor, A. N., and Heavens, A. F. (1997). Karhunen-Loeve Eigenvalue Problems in Cosmology: How Should We Tackle Large Data Sets? *ApJ*, 480:22–+.

Trotta, R. (2007). Applications of Bayesian model selection to cosmological parameters. *MNRAS*, 378:72–82.

Trotta, R. (2008). Bayes in the sky: Bayesian inference and model selection in cosmology. *Contemporary Physics*, 49:71–104.

Turner, M. S. and White, M. (1997). CDM models with a smooth component. *Phys. Rev. D*, 56:4439–+.

Verde, L. (2010). Non-Gaussianity from Large-Scale Structure Surveys. *Advances in Astronomy*, 2010.

Verde, L., Wang, L., Heavens, A. F., and Kamionkowski, M. (2000). Large-scale structure, the cosmic microwave background and primordial non-Gaussianity. *MNRAS*, 313:141–147.

Wands, D. (2008). Multiple Field Inflation. In Lemoine, M., Martin, J., and Peter, P., editors, *Inflationary Cosmology*, volume 738 of *Lecture Notes in Physics, Berlin Springer Verlag*, page 275.

Wang, L. and Steinhardt, P. J. (1998). Cluster Abundance Constraints for Cosmological Models with a Time-varying, Spatially Inhomogeneous Energy Component with Negative Pressure. *ApJ*, 508:483–490.

Wang, Y. (2013). Inflation, Cosmic Perturbations and Non-Gaussianities. *ArXiv e-prints 1303.1523*.

Weinberg, D. H. (1995). Recovering Initial Conditions from Present-Day Structure. In *American Astronomical Society Meeting Abstracts #186*, volume 27 of *Bulletin of the American Astronomical Society*, page 853.

White, M. (2005). The theory of baryon oscillations. In *Probing the Dark Universe with Subaru and Gemini*.

White, M. and Hu, W. (2000). A New Algorithm for Computing Statistics of Weak Lensing by Large-Scale Structure. *ApJ*, 537:1–11.

Wright, E. L., Bennett, C. L., Gorski, K., Hinshaw, G., and Smoot, G. F. (1996). Angular Power Spectrum of the Cosmic Microwave Background Anisotropy seen by the COBE DMR. *ApJL*, 464:L21.

Zaldarriaga, M. (2000). Lensing of the CMB: Non-Gaussian aspects. *Phys. Rev. D*, 62(6):063510.

Zaldarriaga, M. (2004). Non-Gaussianities in models with a varying inflaton decay rate. *Phys. Rev. D*, 69(4):043508.

Zeldovich, Y. B., Kurt, V. G., and Syunyaev, R. A. (1969). Recombination of Hydrogen in the Hot Model of the Universe. *Soviet Journal of Experimental and Theoretical Physics*, 28:146.

Zhan, H., Wang, L., Pinto, P., and Tyson, J. A. (2008). Measuring baryon acoustic oscillations with millions of supernovae.

Zhao, G.-B., Saito, S., Percival, W. J., Ross, A. J., Montesano, F., Viel, M., Schneider, D. P., Ernst, D. J., and et, a. (2012). The clustering of galaxies in the SDSS-III Baryon Oscillation Spectroscopic Survey: weighing the neutrino mass using the galaxy power spectrum of the CMASS sample. *ArXiv e-prints 1211.3741*.

ACKNOWLEDGEMENTS

It is finally time for expressing my gratitude to everyone contributed to this journey, in one way or another.
I would like to start from Prof. **Joachim Wambsganß** and Prof. **Eva Grebel**: thank you for the kind hospitality at the Astronomisches Rechen-Institut throughout these years.
I deeply thank the **H**eidelberg **G**raduate **S**chool for **F**undamental **P**hysics, for the funding that made life in Heidelberg even possible.
I also thank all the administrative staff of **HGSFP**, **ARI**, and **ITA** for their helpfulness and kindness.

On a more personal note: I would not be here if it was not for you, **Björn**. I will never be grateful enough for you giving me this wonderful opportunity. Thank you for letting me be your student. Your enthusiasm, your unconditioned love for science, and your passion for teaching have been, and continue to be, simply inspiring. I could not ask for more, and I am grateful for everything you taught me.
I thank **Matthias**, for all his suggestions, for letting me tutor his course in Cosmology, and most of all for being a daily source of learning. It has been an honor working so close to you.
I deeply thank Prof. **Luca Amendola**, for kindly accepting to be my second corrector, and Prof. **Karlheinz Meier** and Prof. **Eva Grebel** for giving me the honor of joining my examination committee.
A warm thank you goes to **Maik Weber** and **Youness Ayaita**, for their precious contribution to the work on baryon acoustic oscillations, and to **Lavinia Heisenberg** and **Christian Byrnes** for the work on primordial non-Gaussianities.

I am grateful to all the colleagues at the Astronomisches Rechen Institut and Institut für Theoretische Astrophysik that in some way contributed to this work and made pleasant my everyday life. In particular, my warmest thank you goes to **Jan**, **Christian**, **Alex**, **Matteo**, **Mauricio**, **Luigi**, **Felix**, **Matthias**, **Gero**, for the nice and funny atmosphere during all the ITA and ARI breaks.
I also thank **Aram**, for our first two years here in Heidelberg, for all our stimulating discussions about philosophy, all the pasta al pesto and the laughs together. And for reminding me that most of the times nothing lasts forever, not even friendships.
Thank you **Denjia**, thank you **Massimo**, thank you sweet **Gisella**, and **Mario**, and **Sara**: I wish we had had more time to spend together, but who knows what future will bring us.

One special thanks goes to **Frederik**, for the warmest of welcoming in a strange land, for all the dinners together, the board games and the refreshing chats. Dear Fritsch, I missed your smiling face at our door, in these months.
Thanks to the lovely **Anna** and **Emanuela**: it has been a pleasure enjoying so many coffees with you, mie Contessine, and I am sure still many have to come, wherever we will end up.
Thanks to **Bobi** and **Laura**, because laughing with you during the last months in that blue-white-virtual world of ours kept me away from insanity. Your beloved Omega-wolf.
I thank **Alessandro**, for the words and the thoughts and the images we still have for each other after all these years, after all this road in between us. After all.
And how could I forget the core of the Centrale-guys.
Thank you **Adi**! The only thought of you makes me typing exclamation marks, you see? You just bring joy everywhere you go.
Thanks **Juri**, for your awesomeness, of course, and because your place felt like home the very first time I entered that door. спасибо, my friend.
Thank you **Ana**, for your support in this crazy period, for your colors and details, for that peculiar, red-lipped grace of yours. And thank you, **Emanuel**, for all the nice friday nights together, and for what probably were the best lasagne I have ever had (do not tell my grandma, though).
I would also like to thank the most adorable **Agnese**, for her soft and shy touch, and because she smells like mum (and she knows why).
Thank you, **Eleonora**. What would I have done without the daily dose of furry cuteness your links provided me? I am looking forward to dozens of projects together, now, my sweet yet tough sewing-mate. And **Jean Claude**, I cannot wait to beat you at Bang!
I deeply thank **Angelos**, for his gentle voice when needed, for the squeezes when last expected.
Francesca and **Fabio**. More than ten years passed, and different cities and countries and lives. Still, I feel your shoulders next to mine, and every time it is like we are still there, together under some porch.

A warm thank you to my whole dysfunctional, crazy and most beautiful family. Thank you to **Silvia**, **Marco**, i **nonni**, **Laura**, the sweet **Susino**, and the empress **Marguttena**. Thanks to every one of you for always waiting for me, wherever I went. Thank you **Emma**, little sister of mine.
Thank you, **mamma**, for all your support along these years. Thank you for letting me be the person I wanted to be, for letting me fly away, and still holding me tight, always. Thank you, **Gem**, for being the best twin I could ask for, and for that shy way of yours of not understanding how much you make me proud. And lastly, but perhaps more importantly: thank you, **babbo**. I would not be here, had you

not imparted me your deep love for physics. I owe all this to your passion, your intelligence, your patient way to teach me. Thank you.

A very, very special thank-you note goes to **Federica**, of course. What can I say, Fede. You have been sister in the frustration and the joy, in the accomplishments and the disappointments, and *every-single-thing* this adventure brought to us. You simply filled these 1295 days with your curly being, making me laugh as loud as I never had in my entire life. If there is one thing I know, now, in this chaotic and scary turning point of mine, is that we will find a way to keep laughing together.

My last loving words are for you, **Emanuele**: playmate, friend, love, husband. All I recall, is the two of us flying as fast as we can, no matter the distance, no matter the weariness.
Thank you for waiting for me. Thank you for all our sleepy yet cheerful breakfasts, every single day, 600 km apart.
You see? It wasn't that far away, after all.
I'm coming home, now.

[Under my breath.
I thank **Ciube**, for 13 wagging years together. May you sleep tight, my beloved friend.]

COLOPHON

This document was typeset using the typographical look-and-feel `classicthesis` developed by André Miede. The style was inspired by Robert Bringhurst's seminal book on typography *"The Elements of Typographic Style"*. `classicthesis` is available for both LaTeX and LyX:

`http://code.google.com/p/classicthesis/`